

Parton Shower for Massive Fermions

Partonschauer für massive Fermionen

Diplomarbeit
von

Martin Stoll

An der Fakultät für Physik
Institut für Theoretische Physik

Referent: Prof. Dr. D. Zeppenfeld
Korreferent: Prof. Dr. G. Quast

Februar 2012

Ich versichere, dass ich diese Arbeit selbstständig verfasst und ausschließlich die angegebenen Hilfsmittel verwendet habe.

Martin Stoll
Karlsruhe, den 03. Februar 2012

Als Diplomarbeit anerkannt.

Prof. Dr. D. Zeppenfeld
Karlsruhe, den 03. Februar 2012

Deutsche Zusammenfassung

Monte-Carlo-Ereignisgeneratoren sind aus der Analyse moderner Teilchenbeschleuniger-Experimente nicht mehr wegzudenken. Die probabilistische Natur der Quantenmechanik impliziert hier die Simulation von einzelnen, zufällig verteilten Ereignissen, die dann entsprechend der Theorie gewichtet werden. Ein Ereignis wird dabei typischerweise in mehreren Schritten simuliert, die als unabhängig angenommen werden.

Die Streuamplituden und Wirkungsquerschnitte auf Elementarteilchenebene können i.a. störungstheoretisch berechnet werden. In einem Großteil der Prozesse treten hier im Endzustand Quarks und Gluonen, sogenannte Partonen, auf. Sie unterliegen der starken Wechselwirkung, welche durch die Quantenchromodynamik beschrieben wird, und sind die fundamentalen Bausteine der Atomkerne. Partonen werden allerdings nie als freie Teilchen beobachtet, da sie einer zentralen Eigenschaft der QCD, dem Confinement oder Quark-Einschluss, unterliegen. In der Folge bilden mehrere Partonen immer gebundene Zustände, die Hadronen, welche dann im Experiment nachgewiesen werden können. Diese Eigenschaft lässt sich dadurch veranschaulichen, dass Quarks und Gluonen sogenannte Farbladung tragen; gebundene Zustände müssen allerdings immer farblos sein. Am anderen Ende der Energieskala sind energiereiche Partonen asymptotisch frei und eine störungstheoretische Beschreibung ist möglich.

Ereignisgeneratoren bewerkstelligen den Übergang vom harten Prozess zum hadronischen Endzustand in zwei Schritten. Zuerst wird die Energie der einzelnen Partonen im Partonschauer im Rahmen der Störungstheorie durch sukzessive Abstrahlprozesse reduziert. Damit wird ein Vielteilchen-Zustand angenähert, der mit einer Berechnung von Streuamplituden nicht zu bewerkstelligen wäre. Die Partonschauernäherung basiert hierbei auf der Abstrahlung von kollinearen und weichen Partonen, welche die größten Beiträge zum Wirkungsquerschnitt liefern. Zum Ende des Schauers verbleiben Partonen mit geringer Energie und die Störungstheorie verliert ihre Gültigkeit. Im Anschluss werden daher Hadronisierungs-Modelle verwendet, um den partonischen Zustand entsprechend des Confinements in Hadronen überzuführen. Hierbei kommen phänomenologische Modelle zum Einsatz, die zuerst farbverbundene (Anti-)Quarks zu größeren Gebilden zusammenfügen, welche dann in leichtere Hadronen zerfallen.

Ziel dieser Arbeit war die Implementierung eines dipol-artigen Partonschauers in den Ereignisgenerator `Herwig++` unter Berücksichtigung endlicher Partonmassen. In diesem Dipolschauer-Ansatz wird zusätzlich zur herkömmlichen Abstrahlung ein sogenanntes Zuschauer-Parton berücksichtigt, welches einen Rückstoß erfährt. Dadurch wird in jedem Schritt Energie-Impuls-Erhaltung ermöglicht; außerdem erfüllen die Partonen während

des gesamten Prozesses ihre jeweilige Massenschalen-Bedingung. Diese Beschreibung verspricht, physikalisch sinnvoller zu sein als die Standardimplementierung und macht eine nachträgliche Korrektur der einzelnen Impulse, wie sie ansonsten nötig wäre, überflüssig.

Ein wichtiger Punkt bei der numerischen Berechnung von störungstheoretischen Korrekturen zu Wirkungsquerschnitten ist das Auftreten von Divergenzen in Zwischenschritten. Im `Herwig++ Matchbox`-Modul ist hier ein Subtraktions-Ansatz gewählt, in welchem Zusatzterme eingeführt werden, die die Singularitäten jeweils einmal subtrahieren und an anderer Stelle addieren, und somit eine numerische Berechnung möglich machen. Diese Hilfsterte sollten ebenfalls für den Fall endlicher Partonmassen implementiert werden. Eine weitere Aufgabe bestand darin, Partonschauer und harten Prozess konsistent zusammenzuführen, was als `Matching` bezeichnet wird.

Mit all diesen Modifikationen bestand die Erwartung, besonders Prozesse, an denen schwere Quarks beteiligt sind, nun besser beschreiben zu können.

Zum Zwecke des verbesserten Partonschauers wurden die nötigen Splitting-Kernel, welche das Spektrum der Abstrahlung beschreiben, implementiert. Parametrisierungen der Impulse sowie die relevanten Phasenraum-Faktorisierungen wurden für alle Dipolkombinationen und beliebige Massen hergeleitet und ebenfalls für den Fall auslaufender Partonen implementiert. Das Abstrahlungsspektrum der vollständigen Implementierung konnte mit einer unabhängigen Rechnung verglichen und verifiziert werden, wobei besonderes Augenmerk auf den Einfluss großer Quarkmassen gelegt wurde.

Zur Beschreibung von Elektron-Positron-Annihilation in nächstführender Ordnung wurde die entsprechende Korrektur zum Matrixelement implementiert. Gemeinsam mit neuen Catani-Seymour-Dipolen, Einschuboperatoren und kinematischen Abbildungen sind somit alle Bestandteile des Subtraktionsschemas sowie des `Matchings` verfügbar. Die korrekte Funktionsweise der Subtraktionsterme konnte numerisch bestätigt werden. Desweiteren fügen sich die Erweiterungen konsistent in den bisherigen Algorithmus, in welchem eine masselose Näherung verwendet wird, ein. Übereinstimmung sowohl auf Parton- als auch Observablen-Niveau wurde gefunden. Mit diesen Erweiterungen besteht nun die Möglichkeit für den Nutzer, zwischen der masselosen und der weiterentwickelten Implementierung auszuwählen.

Im nächsten Schritt wurde dieses Setup genutzt, um die Freiheitsgrade der Simulation an Daten aus dem LEP-Experiment neu anzupassen. Im Fokus stehen hier v.a. Hadronisierungsparameter sowie die untere Energieschranke des Partonschauers, der sogenannte infrarote Cutoff. Generell konnte die gute Übereinstimmung aus der masselosen Implementierung noch leicht übertroffen werden. Ein Schwachpunkt bleibt allerdings trotz der verbesserten Schauersimulation die Beschreibung der B -Hadron-Fragmentierung, wo die Neuerungen zunächst nicht die gewünschte Wirkung erzielen konnten. Diese Observable beschreibt das Energiespektrum derjenigen Hadronen, die schwere b -Quarks enthalten und ist damit besonders sensibel auf die Neuerungen im massiven Partonschauer. Auf der Suche nach Hinweisen auf die Ursache dieser Unzulänglichkeit, wobei jedoch das nicht-perturbative Hadronisierungsmodell unangetastet bleiben sollte, wurde daher der (experimentell unzugängliche) Zustand nach dem Schauer und direkt vor der Hadronisierung untersucht. Das Spektrum der Primär-Cluster hängt dabei zum einen von der Art des Schauers (dipol-artig oder herkömmlich) ab, zum anderen auch sehr stark vom infraroten Cutoff. Obwohl die Erwartung besteht, dass der Dipolschauer generell eine bessere Beschreibung liefern sollte, so ist ein Vergleich mit dem erfolgreichen Standardschauer durchaus sinnvoll, und deutet in Richtung eines sehr niedrigen Cutoffs für die Evolution von sowohl schweren als auch leichten Quarks. Desweiteren wurde festgestellt, dass Quark-Antiquark-Bildung im Schauer überschätzt wird. Ein zugeschnittenes weiteres Tuning konnte diese Ergebnisse bestätigen und die Beschreibung der B -Hadron-Fragmentierung

wurde signifikant verbessert. In anderen Worten wird durch den niedrigen Cutoff in der Simulation mehr Verantwortung vom Hadronisierungsmodell an den perturbativen Partonschauer übertragen.

Es erscheint jedoch wichtig, weitere Studien zum Übergang vom Partonschauer in den nicht-perturbativen Bereich durchzuführen. Besonderes Augenmerk wäre hier auf die Unterschiede im partonischen Endzustand von dipol-artigen und herkömmlichen Partonschauern zu legen. Gerade unter dem Gesichtspunkt, dass die gängigen Hadronisierungsmodelle im Zusammenspiel mit monopol-artigen Partonschauern entwickelt wurden, scheint eine genauere Analyse vielversprechend. Weiterhin wurde die Frage aufgeworfen, wie der im Dipolschauer auftretende Überschuss an Splittings von $g \mapsto q\bar{q}$ begrenzt werden kann. Hier wäre eine interessante Fragestellung, welche Rolle der infrarote Schauercutoff sowie die Abschirmskala der Splittingkernels genau spielen, sowie in welchem Rahmen Modifikationen an den Splittingkernels möglich sind.

Zusammenfassend lässt sich feststellen, dass die konsistente Implementierung eines dipol-artigen Schauers für massive Partonen im Endzustand eine gute Beschreibung der LEP-Daten liefern kann. Desweiteren wurden die relevanten Größen und Abbildungen, welche im Splittingprozess benötigt werden, auch für den Fall von Hadron-Beschleunigern bestimmt, wodurch einer Implementierung nichts mehr im Wege steht. Dies ist gerade im Hinblick auf den LHC interessant, da hier zum einen ein- und auslaufende Partonen Dipole bilden können, die dann Schauerevolution durchlaufen, und zum anderen wesentlich höhere Energien erreicht werden, wodurch der Einfluss schwerer Quarks besonders zum Tragen kommt.

1. Introduction	1
2. Quantum Chromodynamics	3
2.1. Quantum Field Theory	3
2.2. The QCD Lagrangian	4
2.3. Phenomenological Properties of QCD	5
3. Parton Showers and Higher Orders in Perturbation Theory	7
3.1. Higher-Order Corrections	7
3.2. The General Method of Catani and Seymour	9
3.3. The Parton Shower Approximation	11
3.4. A Formalism using Catani-Seymour Kernels	13
3.5. Matching	14
3.5.1. Motivation	14
3.5.2. NLO Matching	15
4. The Herwig++ Event Generator and Analysis Tools	19
4.1. Hard Process	19
4.2. Parton Shower	19
4.3. Hadronization	20
4.4. The Rivet Analysis Toolkit	22
4.4.1. Overview	22
4.4.2. New Analysis	22
4.5. The Professor Tuning System	22
5. Massive Parton Shower with Local Recoils	25
5.1. Final-State Radiation and Final-State Spectator	25
5.1.1. Kinematics	25
5.1.2. A new Evolution Parameter	27
5.1.3. Phase Space and Splitting Probability	28
5.2. Final-State Radiation and Initial-State Spectator	30
5.2.1. Kinematics	30
5.2.2. Phase Space and Splitting Probability	31
5.3. Initial-State Radiation and Final-State Spectator	33
5.3.1. Kinematics I	33
5.3.2. Kinematics II	34

5.3.3. Phase Space and Splitting Probability	35
5.4. Initial-State Radiation and Initial-State Spectator	36
6. The Herwig++ Add-On Modules and Our Implementation	37
6.1. The <code>exsample</code> Library	37
6.2. The <code>DipoleShower</code> Module	37
6.2.1. Initialization	38
6.2.2. Evolution	38
6.2.3. Finalization of the Shower	39
6.3. The <code>Matchbox</code> Module	39
6.3.1. Automatic Generation of Subtraction Terms	39
6.3.2. Matching with Matrix Element Corrections	41
6.4. Our Implementation	41
7. Analysis I: Code Validation	43
7.1. Shower Radiation	43
7.2. Matrix Element Subtraction	46
7.3. Observables in the Massless Limit	46
7.4. Conclusions	46
8. Analysis II: Simulation Results	49
8.1. Tuning	49
8.1.1. Setup	49
8.1.2. Results and Discussion	50
8.2. B -Hadron Fragmentation	54
8.3. Conclusions	57
9. Conclusions and Outlook	59
A. Implementation	61
A.1. Modified and New Classes	61
A.2. Simulations using Our Implementation	61
B. Splitting Kernels and Insertion Operators	65
B.1. Parton-Shower Splitting Kernels	65
B.2. Splitting Functions in the Subtraction Scheme	66
B.3. Insertion Operator	66
Bibliography	69
Danksagung	73

CHAPTER 1

Introduction

In the history of particle physics, many insights into the properties of elementary particles and forces have been gained. With experiments successively reaching higher energy regimes, new particles were detected which are now consistently incorporated into the Standard Model of Particle Physics [1, 2, 3]. Besides known shortcomings which led to many competing theories commonly denoted BSM theories (beyond the Standard Model), it has been well confirmed by the large majority of experiments. Quantum Chromodynamics (QCD) as part of the Standard Model describes the interactions of quarks and gluons, the fundamental building blocks of atomic nuclei. These particles, collectively called partons, show the peculiar characteristic of never appearing on their own - they always combine to larger entities called hadrons, an effect which is known as confinement. If they are produced in collider experiments, this leads to final states not consisting of elementary particles but of a complicated accumulation of a large number of hadrons which occur in particle jets. Owing to this complexity, plain calculations by hand alone are no longer suitable and a simulation of parton evolution and hadronization becomes necessary. For this reason, Monte Carlo event generators [4, 5, 6] play a crucial role in modern particle physics. Based on sophisticated algorithms that emulate single collider events by making use of random numbers, they allow for detailed simulations that can be compared to experimental data.

In this work, we focus on the QCD simulation of hard scattering processes and subsequent parton showers. Our aim is to give an improved description of the partonic final state by extending the existing implementation in the event generator `Herwig++` [4, 7]. Specifically, our implementation takes finite quark masses fully into account, i.e. it provides a more accurate description of heavy particles. The main obstacle here is that for each non-zero mass, an additional energy scale is introduced that leads to modifications in the pole structure of matrix elements and to a more complicated parametrization of the available phase space. We study leptonic collisions in particular, since they produce very clear hadronic signals with well-defined initial conditions. Thus, our implementation of a new parton shower can easily be compared to data from the LEP experiment.

The outline of this work is as follows.

In Chapter 2, the basic properties of QCD are sketched. Some specific aspects of perturbative corrections are given in Chapter 3. In particular, matrix element corrections and

the parton shower approximation are at the core of this work. Chapter 4 outlines the functionality of `Herwig++` and the analysis tools used to obtain results from our implementation.

The properties of massive dipole-type parton showers, which we derived in the course of this work, are described in Chapter 5. Chapter 6 depicts the implementation into the existing framework.

The validity of our implementation was investigated at parton level, which is described in Chapter 7. In Chapter 8, simulation results are systematically compared to experimental data in order to adjust the free parameters of the model. This particularly involves the degrees of freedom in the hadronization model and limiting conditions of the parton shower evolution.

Conclusions are drawn in Chapter 9, and a critical analysis of the advantages of the algorithm is made. An outlook suggests possible future studies on the topic.

Quantum Chromodynamics

The Standard Model of Particle Physics (SM) is a quantum field theory describing all known fundamental particles and forces (except for gravity) in Nature. Its success stems from the ability to describe the majority of experiments performed at particle colliders so far with very high accuracy. The entire SM particle content has been experimentally confirmed, except for the postulated Higgs boson whose properties are expected to be severely restricted in the near future by the LHC. Since Quantum Chromodynamics (QCD), the theory of quarks and gluons, will play a prominent role throughout this thesis, its basic properties are outlined in this chapter. The SM as a whole is a combination of electroweak theory and QCD, described as the quantum field theory of the underlying gauge group $SU(3) \times SU(2) \times U(1)$.

2.1. Quantum Field Theory

The basic entity from which quantum field theories are constructed is a Lagrangian density. For non-interacting fermionic fields ψ of spin 1/2 and spinless bosonic fields ϕ , respectively, the Lagrangian reads

$$\mathcal{L}_{\text{fermion}}^{\text{free}} = \bar{\psi}(i\not{\partial} - m)\psi, \quad (2.1)$$

$$\mathcal{L}_{\text{boson}}^{\text{free}} = \frac{1}{2}(\partial_{\mu}\phi)^2 - \frac{1}{2}m^2\phi^2. \quad (2.2)$$

Quantization is carried out by interpreting the fields as operators, on which (anti-)commutation properties are imposed¹,

$$\begin{aligned} \{\psi_a(\vec{x}), \psi_b^{\dagger}(\vec{y})\} &\equiv \psi_a(\vec{x})\psi_b^{\dagger}(\vec{y}) + \psi_b^{\dagger}(\vec{y})\psi_a(\vec{x}) = \delta^{(3)}(\vec{x} - \vec{y})\delta_{ab}, \\ [\phi(\vec{x}), \pi(\vec{y})] &\equiv \phi(\vec{x})\pi(\vec{y}) - \pi(\vec{y})\phi(\vec{x}) = i\delta^{(3)}(\vec{x} - \vec{y}), \end{aligned} \quad (2.3)$$

where ψ_i denotes a component of the spinor ψ and π is the conjugate momentum density to the field ϕ .

Many interesting properties arise by virtue of Emmy Noether's theorem, which states that to every continuous symmetry under which the action $\int d^4x \mathcal{L}$ remains invariant,

¹We denote 3-vectors by \vec{x} and 4-vectors by x , where the components are given by x^{μ} , i.e. $x \cdot y \equiv g_{\mu\nu}x^{\mu}y^{\nu} \equiv x^{\mu}y_{\mu} \equiv x^0y^0 - \vec{x} \cdot \vec{y}$.

a corresponding conserved quantity exists. In this sense, invariance under the spatial transformations of the Poincaré group leads to conservation of energy, momentum and angular momentum. Clearly, this is the case for the free Lagrangians in Eqs. (2.1) and (2.2).

Interacting field theories are obtained by imposing intrinsic symmetries on the fields. In the simplest case, demanding invariance under local $U(1)$ transformations of the field spinors (i.e. multiplying each spinor by $\exp[-i\alpha(x)]$) leads to Quantum Electrodynamics, the theory of electrons, positrons and photons. Electroweak theory includes the weak force of radioactive decays and is based on a local $SU(2) \times U(1)$ symmetry. The introduction of the Higgs field breaks the symmetry again, thus introducing mass terms for the fermions and weak gauge bosons. The last ingredient of the Standard Model, Quantum Chromodynamics, is the theory of quarks and gluons which interact via the strong force. We outline the construction of QCD from a local $SU(3)$ symmetry in more detail in the following section, since it plays an important role throughout this thesis.

2.2. The QCD Lagrangian

Quantum Chromodynamics is a non-abelian gauge theory based on an $SU(3)_C$ gauge group (where C stands for “colour”). Starting from a fermionic Lagrangian for different quark flavours f

$$\mathcal{L} = \sum_{f=u,d,s,\dots} \bar{\Psi}_f (i\gamma_\mu \partial^\mu - m_f) \Psi_f, \quad (2.4)$$

the symmetry is locally imposed together with a connection (expressed through gauge fields A), which is required for consistency. This procedure results in a Lagrangian where partial derivatives are replaced by covariant derivatives and is known as minimal coupling,

$$\partial \mapsto D \equiv \partial \mathbb{1}^{\text{colour}} - ig_s A^a t^a. \quad (2.5)$$

g_s denotes the strong coupling constant. The gauge fields² $\{A^a\}$ represent gluon fields that transform according to the adjoint representation. Hence, they can be decomposed into a basis formed by the eight generators t^a of the symmetry group $SU(3)_C$. In the fundamental representation, the generators are given by the Gell-Mann matrices: $t^a \equiv \frac{\lambda^a}{2}$.

The fermions (quarks) transform according to the standard representation, i.e. they are colour triplets $\Psi_f \equiv \Psi_f^c$ ($c = \text{red, blue, green}$). In order to simplify the notation, colour indices are suppressed from now on whenever unambiguous. After an infinitesimal local $SU(3)_C$ transformation, which is expressed through parameters $\alpha^a \equiv \alpha^a(x)$, the respective fields are given by

$$\Psi(x) \mapsto (1 + i\alpha^a t^a) \Psi(x), \quad (2.6)$$

$$D^\mu \Psi(x) \mapsto (1 + i\alpha^a t^a) D^\mu \Psi(x), \quad (2.7)$$

$$A^a \mapsto A^a + \frac{1}{g_s} \partial \alpha^a + f^{abc} A^b \alpha^c, \quad (2.8)$$

where f^{abc} are the structure constants of the $SU(3)_C$ Lie algebra which obey

$$[t^a, t^b] = if^{abc} t^c. \quad (2.9)$$

Here lies the crucial difference between QCD and abelian gauge theories such as QED, where the structure constants vanish. This property is related to gluon self-coupling and ultimately leads to asymptotic freedom, see Section 2.3.

²In our notation, the set of all components A^a is denoted $\{A^a\}$.

A gauge-invariant field-strength tensor can be defined via the covariant derivative

$$[D_\mu, D_\nu] = -ig_s F_{\mu\nu}^a t^a \quad (2.10)$$

which, expressed in terms of the gauge fields, is given by

$$F_{\mu\nu}^a = \partial_\mu A_\nu^a - \partial_\nu A_\mu^a + g_s f^{abc} A_\mu^b A_\nu^c. \quad (2.11)$$

The whole QCD Lagrangian then reads (colour indices suppressed)

$$\mathcal{L} = -\frac{1}{4}(F_{\mu\nu}^a)^2 + \sum_{f=u,d,s,\dots} \bar{\Psi}_f (\not{\partial} - m_f) \Psi_f. \quad (2.12)$$

Note that in QCD as a separate theory, the gauge-invariant Lagrangian can contain fermionic mass terms as written above since they do not break SU(3) gauge theory. On the other hand, the underlying SU(2) \times U(1) symmetry of electroweak theory is explicitly broken by similar terms. This is one of the reasons for the introduction of an additional Higgs field in the Standard Model, where QCD and electroweak theory are merged. As we are not concerned with electroweak interactions in this work, we do not go into any detail here. However, a comprehensive discussion of QCD and the Standard Model can be found in many textbooks, see e.g. Ref. [8].

Quantization of the gluon fields can be carried out by adding a gauge-fixing term to the Lagrangian in order to eliminate a large class of physically equivalent gauges. Unphysical gluon polarizations can be compensated by the introduction of additional (and equally unphysical) Faddeev-Popov ghost fields. Alternatively, the gauge fields can be treated in the axial gauge where $n \cdot A^a = 0$ for fixed gauge vector n .

2.3. Phenomenological Properties of QCD

When considering higher-order corrections to QCD processes, ultraviolet divergences occur and are handled by distinguishing between the bare parameters of the Lagrangian and physical quantities. In this procedure, which is called renormalization, the divergence-free and physically meaningful renormalized coupling constant $\alpha_S(\mu^2)$ is defined, where $\alpha_S \equiv g_s^2/4\pi$. Corrections from higher orders in perturbation theory are incorporated in α_S , which also exhibits a dependence on the renormalization scale μ , i.e. the scale of momentum transfer at which renormalization is performed. Requiring any result to be independent of the arbitrary choice of μ leads to a differential equation for the renormalized coupling $\alpha_S(\mu^2)$, which is governed by the so-called β function,

$$\frac{\partial}{\partial(\ln \mu^2)} \alpha_S(\mu^2) = \beta(\alpha_S(\mu^2)). \quad (2.13)$$

$\beta(\alpha_S)$ is derived from higher-order calculations and reads (to one-loop order accuracy)

$$\beta(g) = -\frac{g^3}{(4\pi)^2} \left[\frac{11}{3} C_2(G) - \frac{4}{3} n_f C(r) \right]. \quad (2.14)$$

The SU(N) Casimir operators are given by $C(r) = \frac{1}{2}$ and $C_2(G) = N$ respectively. For the SU(3) symmetry group and $n_f = 6$ observed quark flavours, the β function is of negative sign. The resulting running coupling constant $\alpha_S(Q^2)$ thus becomes effectively smaller at higher scales (which corresponds to smaller distances) and the solution of Eq. (2.13) is given by

$$\alpha_S(Q^2) = \frac{\alpha_S(\mu^2)}{1 + \frac{\alpha_S(\mu^2)}{12\pi} (33 - 2n_f) \log(Q^2/\mu^2)}, \quad (2.15)$$

where Q^2 denotes the scale of the momentum transfer of the process under consideration. Two important effects arise from this property. First, perturbative QCD calculations are valid only for energy scales $\gtrsim \Lambda_{QCD} = \mathcal{O}(100 \text{ MeV})$, since in this regime the coupling constant α_S can be considered small. This implies that in the high-energy regime, quarks and gluons appear to be almost free particles, an effect which is known as asymptotic freedom [9, 10]. Second, for large distances (or, correspondingly, low energy scales) perturbation theory breaks down. Experimentally, only $SU(3)_C$ singlet states (hadrons) are observed in this regime. This property, which cannot be described within the perturbative framework of QCD, is called confinement.

Asymptotic freedom is a distinct property of non-abelian gauge theories with an appropriately small number of flavours [11, Chapter 14.6], and can be traced back to three- and four-gluon vertices, whose analogues are absent in abelian theories.

Parton Showers and Higher Orders in Perturbation Theory

Performing QCD calculations beyond the leading order is absolutely crucial in order to obtain reliable results, as will be motivated in this chapter. We thus give a brief description of the structure of these higher-order corrections with a focus on their largest contributions. By virtue of the Kinoshita-Lee-Nauenberg (KLN) theorem [12], computational results for sufficiently inclusive and infrared-safe observables are always finite. In intermediate steps, however, infrared divergences occur which can be traced back to soft and collinear partons. These terms have to be cancelled analytically, but this procedure prevents from a straightforward numerical implementation. A calculational formalism that explicitly overcomes these obstacles is introduced in Section 3.2.

The focus of this work lies on the implementation of an improved (dipole-type) parton shower that explicitly takes all finite parton masses into account. Therefore, Section 3.3 gives a description of the basic properties of parton showers. In Section 3.4, we recapitulate the shower formalism proposed in Ref. [13] and implemented in the `Herwig++` `DipoleShower` module for massless partons, which is the basis for our new implementation. Section 3.5 outlines the merging of NLO calculations and parton showers, called matching. A consistent matching algorithm is implemented in the `Herwig++` `Matchbox` module for massless partons, which also was extended in the course of this work.

3.1. Higher-Order Corrections

In perturbative QCD, the strong coupling constant is still of $\mathcal{O}(0.1)$ at scales typically encountered at collider experiments. Due to this fact, higher-order corrections to matrix elements can in general not be considered to turn out small. These corrections include loop diagrams as well as additional real emissions on top of the leading-order (LO) process. A conventional estimate of higher orders in perturbation theory is by means of scale variations. The energy scale at which $\alpha_S(Q^2)$ is evaluated in the calculation is varied by a factor of 2 and 1/2, and the difference between the respective results serves as a prediction of the absolute value of higher-order corrections. Indeed, thus estimated theoretical uncertainties typically become smaller as higher orders in α_S are determined.

An inclusive observable $\langle O \rangle$ at next-to-leading order (NLO) accuracy receives contributions from the LO or Born part of the cross section (σ^B), from real emission (σ^R) and from

virtual corrections (σ^V)

$$\begin{aligned} \langle O \rangle^{NLO} &= \int_m d\sigma^B(\{p_i\}) O_m(\{p_i\}) \\ &+ \int_{m+1} d\sigma^R(\{p_i\}) O_{m+1}(\{p_i\}) + \int_m d\sigma^V(\{p_i\}) O_m(\{p_i\}). \end{aligned} \quad (3.1)$$

\int_n denotes the integration over the n -parton final state phase space.

An important issue in higher-order calculations is the handling of divergences which occur at intermediate steps during calculations. Ultraviolet (UV) divergences stem from integrating over (unbounded) loop momenta and are absorbed into physically meaningful renormalized field operators, coupling constants and masses. The second class of divergences – infrared (IR) divergences – is connected to either the emission of a soft gluon or two massless partons becoming collinear. Massive partons do not exhibit collinear divergences, however, the respective contributions are still very large in the related phase-space regions. In either case the two partons undergo hadronization and cannot be resolved as separate jets by any experiment. Most commonly, the divergences are regularized by analytic continuation of the integrals to $d = 4 - 2\epsilon$ space-time dimensions, as this is the only known gauge- and Lorentz-invariant procedure. In this prescription, the IR divergences of the virtual contribution are manifest in poles in ϵ whereas those of the real emission contribution emerge implicitly after integration over the respective phase-space regions. At NLO, poles of the form $1/\epsilon$ stem from (massless) collinear partons or soft gluon emission. Poles of the form $1/\epsilon^2$ arise in massless configurations and are related to soft-and-collinear divergences. For sufficiently inclusive and IR safe quantities, these divergences always cancel between the real emission and virtual contribution of a fixed-order matrix element, as expressed by the KLN theorem.

Subtleties arise whenever initial-state partons or identified final-state partons are involved. Both types of processes are referred to as processes with identified partons. Initial-state partons occur in hadronic collider experiments where they are extracted from a hadron with momentum distribution according to the parton distribution function (PDF). To leading order in QCD, the parton momenta are collinear to the momentum of the proton, and if the hard parton-level process involves scattering into a final state X , the cross section at hadron level is given by the convolution

$$\sigma(p + p \mapsto X + Y) = \int_0^1 dx_1 \int_0^1 dx_2 \sum_{a,b} f_a(x_1; \mu_F) f_b(x_2; \mu_F) \hat{\sigma}(a(x_1 P_1) + b(x_2 P_2) \mapsto X), \quad (3.2)$$

where f_i denotes the respective PDF, Y is any hadronic final state and we considered proton-proton collisions with momenta $P_{1,2}$. The partons carry longitudinal momentum fractions x_i , additionally all possible flavours a, b for the process under consideration have to be taken into account. The PDFs depend on the factorization scale μ_F which corresponds to the resolution at which the hadron is being probed.

In the partonic cross section, the phase space exhibits further constraints since the direction of the identified parton momenta has to be kept fixed. Thus, integrating the real emission contribution over the collinear region does generate additional poles in ϵ which are not compensated by the divergences stemming from the virtual contribution any more. However, this problem can be solved by realizing that parton and hadron momenta are connected via a momentum fraction x . The additional divergences are inseparably connected with the non-perturbative PDFs (or, for the case of identified partons in the final state, fragmentation functions) and can be absorbed into renormalized distributions. As a formal result, in calculations at parton level an additional divergent term has to be added

in order to render the cross section finite, called collinear counter term,

$$\int_0^1 dz \int_m d\sigma^B(\{p_i^C(z)\}) O_m(\{p_i^C(z)\}) \Gamma(z). \quad (3.3)$$

It is defined via a process-independent factor $\Gamma(z)$ that is divergent as $\epsilon \mapsto 0$, and the phase-space point $\{p_i^C(z)\}$ denotes that one parton entering the Born cross section is carrying a momentum fraction z with respect to the momentum of the respective parton in the real emission contribution.

While arbitrary processes turn out to produce a finite prediction due to the cancellation of all divergences, a straightforward numerical integration is prohibited: IR divergences first have to be extracted and cancelled analytically before evaluating the respective integrals in $d = 4$ dimensions. Once this is done, Monte Carlo event generators such as **Herwig++** can be used to simulate events and make predictions for an observable O .

3.2. The General Method of Catani and Seymour

In order to numerically evaluate the separately divergent integrals of NLO calculations, several subtraction schemes have been developed. Commonly used schemes are FKS [14] and antenna subtraction [15, 16], however, we base our implementation on a general and very flexible formalism put forward by Catani and Seymour in 1997 [17] and extended to incorporate the influence of finite parton masses five years later [18]. In this formalism, an auxiliary cross section $d\sigma^A$ is introduced which is to have the same point-wise singular behaviour as $d\sigma^R$ in d space-time dimensions. The quantity $d\sigma^R - d\sigma^A$ can then be safely integrated in $d = 4$ dimensions. As an additional property, outside the singular regions $d\sigma^A$ is constructed in a way which allows for an analytical integration over the one-parton subspace related to parton emission. The KLN theorem then states that the poles in ϵ emerging from this integration cancel all poles from the remaining terms. Thus, the modified virtual contribution $d\sigma^V + \int_1 d\sigma^A$ can also be safely integrated in four space-time dimensions as long as no initial-state partons or identified partons in the final state are involved. If, however, identified partons do occur, an additional counter term is to be added as outlined in the previous section. More precisely, in the general case an inclusive and IR-safe observable $\langle O \rangle$ is calculated as

$$\begin{aligned} \langle O \rangle^{\text{NLO}} &= \int_m d\sigma^B(\{p_i\}) O_m(\{p_i\}) \\ &+ \int_{m+1} [d\sigma^R(\{p_i\}) O_{m+1}(\{p_i\}) - d\sigma^A(\{p_i\}) O_m(\{p_i\})] \\ &+ \int_m \left[d\sigma^V(\{p_i\}) + \int_1 d\sigma^A(\{p_i\}) \right] O_m(\{p_i\}) \\ &+ \int_0^1 dz \int_m d\sigma^B(\{p_i^C(z)\}) O_m(\{p_i^C(z)\}) \Gamma(z). \end{aligned} \quad (3.4)$$

The first two terms on the right-hand side are finite and integrable in four space-time dimensions. The divergences in the virtual contribution and collinear counter term cancel analytically against the auxiliary term integrated over the one-parton subspace.

In QCD, the differential real emission cross section features properties called factorization, see e.g. Ref. [19]. More specifically, in the phase-space regions of

- a soft gluon,
- two partons in the quasi-collinear limit¹,

the differential real emission cross section can be expressed as the convolution of the squared Born matrix element with process-independent factors. Specifically, these factors only depend on the external legs of the Born element and generally exhibit colour correlations with the latter in the soft region and spin correlations in the (quasi-)collinear region. Note that the factorization properties hold in the very phase-space regions where the poles in the integrals occur, i.e. the auxiliary cross section $d\sigma^A$ is required to resemble the real emission contribution $d\sigma^R$ only in the limits where the factorization properties hold. Therefore, $d\sigma^A$ can be similarly decomposed into $d\sigma^B$ and process-independent factors. Symbolically, we express $d\sigma^A$ as a sum over dipole factors dV_{dipole} convoluted with the Born cross section (indicated by the symbol \otimes),

$$d\sigma^A = \sum_{\text{dipoles}} d\sigma^B \otimes dV_{\text{dipole}}. \quad (3.5)$$

Each dipole factor describes radiation off an external parton (the “emitter”), with another external parton acting as a “spectator”. A detailed discussion of the splitting kinematics is presented in Chapter 5, where the dipole picture is used to put forward a parton shower. A visualization of the dipoles is depicted in Fig. 3.1.

Since the dipole factors are process-independent, the integral over the one-parton subspace can be carried out analytically and yields a universal factor which in the simple case of no identified parton reads

$$\mathbf{I} \equiv \sum_{\text{dipoles}} \int_1 dV_{\text{dipole}}. \quad (3.6)$$

This contribution is called insertion operator since in the calculation, it is convoluted with (“inserted into”) the Born matrix element. In the general case, additional divergences emerge in this integral which are analytically cancelled against the collinear counter term. The resulting operator \mathbf{I} again removes all divergences from the virtual contribution. Additionally, a finite remainder is left from the collinear counter term which carries the dependence on the momentum fraction z . It is split into two new insertion operators \mathbf{P} and \mathbf{K} featuring a different dependence on z and the rescaled momenta $\{p_i^C(z)\}$, respectively. Most notably, only \mathbf{P} depends on the factorization scale.

¹The collinear divergence, which is obtained by letting the transverse momentum between two massless partons vanish ($p_{\perp} \mapsto 0$), is screened by finite parton masses. Therefore, the quasi-collinear limit is defined by the property that parton masses and transverse momentum vanish uniformly, $p_{\perp} \mapsto \lambda p_{\perp}$, $m_i \mapsto \lambda m_i$ where $\lambda \mapsto 0$. With this definition, factorization properties hold for massive partons as well.

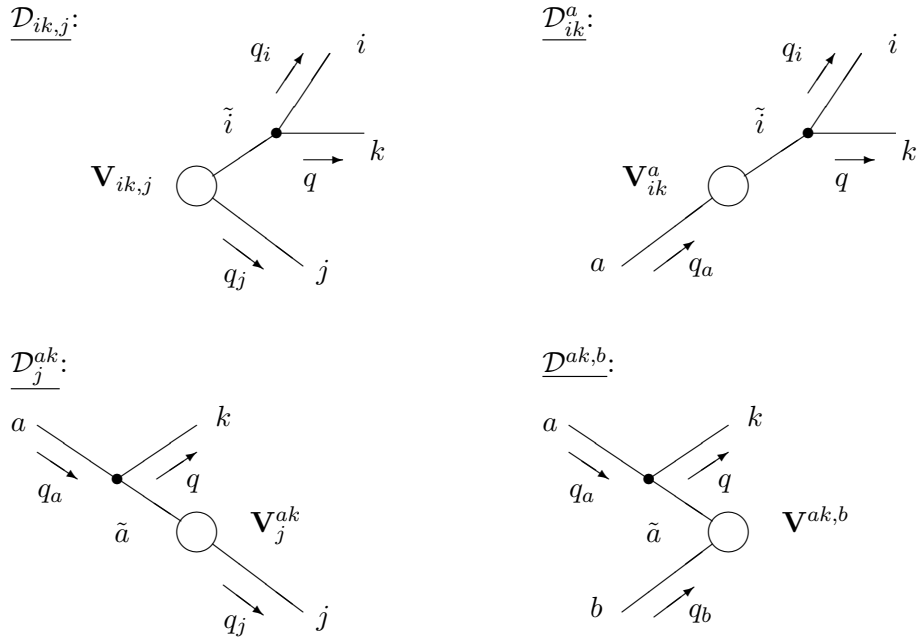


Figure 3.1.: Diagrammatic visualization for the different emitter-spectator cases. Final state partons are labelled i, j, k , initial state partons a, b . $\{q_n\}$ denote the momenta after splitting. The spectator absorbs a longitudinal recoil such that all partons remain on their respective mass shells. Starting from the upper left, the dipole configurations are named as follows: final-final, final-initial, initial-final, and initial-initial, according to whether the emitter and spectator belong to the initial or final state.

Incorporating all the notations outlined above, the cross section is rewritten,

$$\begin{aligned}
\langle O \rangle^{\text{NLO}} &= \int_m d\sigma^B(\{p_i\}) O_m(\{p_i\}) \\
&+ \int_{m+1} \left[(d\sigma^R(\{p_i\}))_{\epsilon=0} O_{m+1}(\{p_i\}) \right. \\
&\quad \left. - \left(\sum_{\text{dipoles}} d\sigma^B(\{p_i\}) \otimes dV_{\text{dipole}}(\{p_i\}) \right)_{\epsilon=0} O_m(\{p_i\}) \right] \\
&+ \int_m [d\sigma^V(\{p_i\}) + d\sigma^B(\{p_i\}) \otimes \mathbf{I}(\{p_i\})]_{\epsilon=0} O_m(\{p_i\}) \\
&+ \int_0^1 dz \int_m [d\sigma^B(\{p_i^C(z)\}) \otimes (\mathbf{P} + \mathbf{K})(z, \{p_i^C(z)\})]_{\epsilon=0} O_m(\{p_i^C(z)\}). \quad (3.7)
\end{aligned}$$

The insertion operators \mathbf{I} , \mathbf{P} and \mathbf{K} are universal and, after analytic cancellation of the divergences between \mathbf{I} and the virtual contribution, finite for $\epsilon \mapsto 0$. Therefore, all phase-space integrals can be evaluated numerically in four space-time dimensions.

The explicit form of all the process-independent factors in the dipole formalism is derived in Refs. [17, 18] and listed in Appendix B. In order to evaluate the terms where operators are inserted into the Born matrix element, colour and spin projections of the latter are required.

3.3. The Parton Shower Approximation

Fixed-order calculations in perturbative QCD typically give an accurate description of processes in the regime where the perturbation series expansion is convergent. However,

there are kinematic regions in phase space where higher-order corrections can overcome the smallness of the coupling α_S . These enhancements appear in configurations related to the emission of soft or collinear partons and occur as poles in $1/\epsilon^2$ or $1/\epsilon$ in the calculations. If a cutoff parameter ρ is applied (where the singularities correspond to $\rho \mapsto 0$), the result is enhanced by factors of the form

$$\alpha_S \ln^2(\rho) \quad \text{and} \quad \alpha_S \ln(\rho) \quad (3.8)$$

(in one-to-one correspondence with the poles in $1/\epsilon^2$ and $1/\epsilon$). These contributions occur to all orders in α_S ,

$$\alpha_S^n \ln^{2n}(\rho) \quad \text{and} \quad \alpha_S^n \ln^{2n-1}(\rho), \quad (3.9)$$

and are referred to as leading logarithmic (LL) contributions. Less singular contributions $\alpha_S^n \ln^{2n-2}(\rho)$, ... are referred to as next-to-leading logarithmic (NLL) contributions etc. The aim of the parton shower approximation is to effectively resum the leading terms to all orders, which is possible for a large class of observables.

The enhancements in the (quasi-)collinear limit are associated with parton branching. The factorization properties of the real emission cross section state that

$$d\sigma_{m+1} = d\sigma_m \frac{dQ}{Q} dz \frac{\alpha_S}{2\pi} P_{\text{split}}(Q, z), \quad (3.10)$$

where the factor

$$\frac{dQ}{Q} dz \frac{\alpha_S}{2\pi} P_{\text{split}}(Q, z) \equiv d\mathcal{P}(Q, z) \quad (3.11)$$

can be interpreted as the splitting rate [20], i.e. higher-orders corrections are obtained by considering emissions off external partons. Common choices for the scale Q are the virtuality t of the parton under consideration, the opening angle θ between the splitting products, or the transverse momentum p_\perp between the latter. In the dipole shower formalism treated in this thesis, p_\perp^2 is chosen as the typical scale of a splitting and will be used in the following. z denotes the second kinematic variable, e.g. a quantity proportional to the energy fraction of the first daughter parton to the mother parton. Any dependence on the azimuthal angle is already assumed to be integrated out. P_{split} denotes the splitting kernel, which is derived in the (quasi-)collinear limit and governs the spectrum of the emission.

Parton showers are built from multiple branching as a Markov process, whose main calculational tool is the Sudakov form factor

$$\Delta(Q^2, p_\perp^2) = \exp \left[- \int_{p_\perp^2}^{Q^2} \frac{d\bar{p}_\perp^2}{\bar{p}_\perp^2} \int_{z_-(\bar{p}_\perp^2)}^{z_+(\bar{p}_\perp^2)} dz \frac{\alpha_s}{2\pi} P_{\text{split}}(\bar{p}_\perp^2, z) \right], \quad (3.12)$$

giving the probability of evolution from a hard scale Q^2 to a scale p_\perp^2 without resolved splitting. The Sudakov anomalous dimension is obtained by integrating the splitting kernels, $\Gamma(\bar{p}_\perp^2) \equiv \int dz P_{\text{split}}(\bar{p}_\perp^2, z)$. p_\perp can be chosen as the evolution variable of the parton shower, together with a second suitable kinematic variable. When considering non-collinear enhancements due to soft gluon emission as well, we are led to the choice of the opening angle [20] or transverse momentum [13] as evolution variable. In the first case, an angular-ordered parton shower emerges where soft gluon emission is confined to a cone around the emitter parton. The correct LL and NLL contributions are then recovered if strong ordering of successive splittings is imposed [13], $\theta^{n+1} \ll \theta^n$ or $p_\perp^{n+1} \ll p_\perp^n$, respectively, and the shower is called coherent.

In fact, the Sudakov form factor sums enhanced virtual as well as real contributions to all orders, since the virtual corrections contribute to the no-splitting probability. By unitarity, i.e. branching and no-branching probabilities sum to one, the cancellation of the

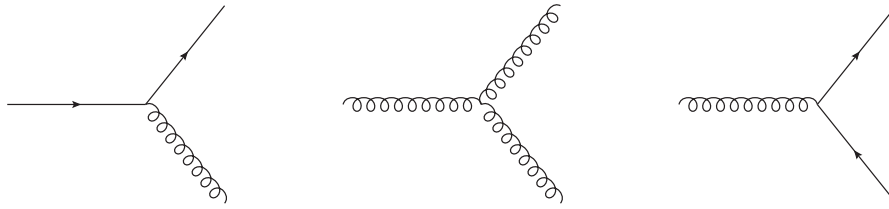


Figure 3.2.: Relevant splitting processes in a QCD parton shower.

divergences in the splitting functions and the corresponding virtual corrections is handled implicitly.

In QCD, possible splittings include gluon emission and the splitting of a gluon into a quark-antiquark pair, see Fig. 3.2. Thus, in the Sudakov form factor all possible splittings from all legs contribute. The form factor itself, often referred to as a jet function, plays a central role in any parton shower since it is used to determine the scale of the next splitting.

3.4. A Formalism using Catani-Seymour Kernels

A parton shower formalism based on Catani-Seymour dipole kernels was proposed in Refs. [21, 22] and implemented into *Herwig++* for the case of massless partons, following a new approach put forward in Refs. [13, 23, 24]. These kernels have originally been derived in the context of the subtraction formalism for NLO calculations, cf. Section 3.2. A substantial feature of the formalism is the implementation of exact 4-momentum conservation at each splitting by considering $2 \mapsto 3$ processes. The additional parton acts as a so-called spectator and is chosen to absorb the longitudinal recoil. On the contrary, in previous implementations of a conventional $1 \mapsto 2$ parton shower, this is not possible and all parton momenta have to be put on mass shell after the evolution terminated. In the dipole picture, each two colour-connected partons form an emitter-spectator pair that may radiate. The definition of colour-connection is illustrated in Fig. 3.3. Both legs have to be considered for emission and the recoil absorbed by the partner parton is to be taken in the longitudinal direction of the splitting, i.e. only the direct splitting products experience a transverse momentum component. When these conditions are met, interference diagrams are collinearly subleading and the splitting kernels are left unchanged by the recoil. See again Fig. 3.1 for an illustration, which is now interpreted as showing emissions during the parton shower. The blob symbolizes the part of the process connecting the emitter-spectator pair.

Parton shower evolution is ordered in transverse momentum p_{\perp} , in the sense that the absolute value of p_{\perp} is successively reduced in each splitting process. By also applying suitably chosen phase-space boundaries, the correct expression for the Sudakov anomalous dimension is recovered. Effects which stem from the recoils only enter beyond NLL. Additionally, the hard scale of a single cascade is to be chosen to be the dipole's invariant mass in order to reproduce the correct LL contributions. Via strong evolution ordering in transverse momentum (as opposed to angular ordering for monopole-type showers [20]), the correct coherence properties related to multiple gluon emission are reproduced, as mentioned in the previous section.

Since finite parton masses do not call for any conceptual adjustment of this line of argument, the reader is referred to Ref. [13] for technicalities. We will, however, present the work flow of the implementation in more detail in Chapter 6, together with a discussion of the modifications which are necessary in the case of finite parton masses.

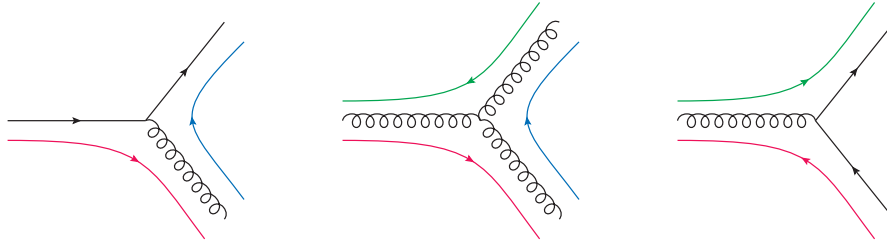


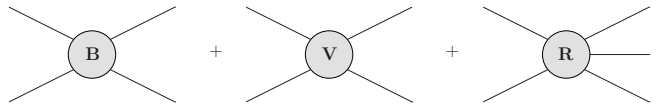
Figure 3.3.: In the large- N_c limit, where N_c is the number of colours in QCD, each outgoing (anti-)quark can be assigned an (anti-)colour, and each gluon carries both colour and anticolour. As a result of colour charge conservation, unambiguous and continuous colour lines can be reconstructed. The colour flow of primary partons is determined by the matrix element.

3.5. Matching

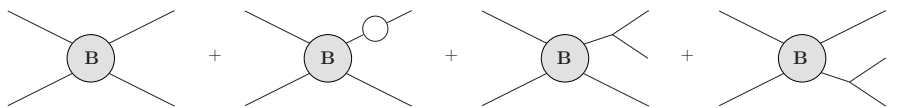
In this section, we describe in very simple terms the procedure of matching parton showers and higher-order matrix element calculations. Parton showers give an approximation of the leading terms of a process to all orders, whereas fixed-order matrix elements are exact to some specified order k in the coupling constant α_S . When both are combined, an effect known as double counting occurs which leads to wrong results. By use of a matched calculation together with subsequent showering, however, the correct result is recovered.

3.5.1. Motivation

Let us first have a look at the difference between a fixed-order calculation and the parton shower prediction at NLO. The NLO calculation can be decomposed into the born part (B) and two perturbative corrections of $\mathcal{O}(\alpha_S)$, namely the virtual contribution (V) and the real emission contribution (R)



(For illustration purposes, an $l\bar{l} \mapsto q\bar{q}$ process is depicted.) On the other hand, each emission in the parton shower formally increases the order k in α_S to $k + 1$, thus serving as an approximation to the complete fixed-order calculation. Starting off the Born matrix element, emissions are possible from both final-state legs, and the shower prediction can symbolically be written



The second term symbolizes that virtual corrections are incorporated in the Sudakov form factor and cancel the IR divergences from the real emission contribution. We see that if we naïvely let the parton shower act on the matrix elements at NLO, the shower emission off the Born part contributes additional terms formally of $\mathcal{O}(\alpha_S)$. Thus, the NLO contribution is doubly counted which leads to a wrong result. Note that when the shower starts off the real emission contribution, the first emission will formally be of higher order α_S^2 .

In the following we give a schematic derivation of matched NLO calculations, where the doubly-counted contributions are being removed.

3.5.2. NLO Matching

In a simplified model, we consider an LO process with m partons in the final state and we symbolize all kinematic degrees of freedom in the phase space by the variable x . The additional degrees of freedom describing the real emission contribution are denoted y , where the notation $y \mapsto 0$ indicates the limit of unresolved parton emission. An observable O is labelled $O(x)$ if referring to the m -parton configuration, and $O(x, y)$ if referring to the real emission $m + 1$ -parton configuration. We require that O is infrared safe, i.e.

$$O(x, y) \mapsto O(x) \quad , \quad \text{if } y \mapsto 0. \quad (3.13)$$

For the sake of clarifying the simplified notation, we quickly recapitulate the matrix element evaluation in the Catani-Seymour subtraction scheme, cf. Section 3.2. At NLO accuracy, the prediction for O is given by the Born and real emission contribution with respective squared amplitudes $B(x)$ and $\alpha_S R(x, y)/y$, and the virtual interference term $\alpha_S V(x)$,

$$\begin{aligned} \langle O \rangle_{NLO} &= \int_m dx B(x) O(x) \\ &+ \alpha_s \int_m dx V(x) O(x) \\ &+ \alpha_s \int_{m+1} dx dy \frac{R(x, y)}{y} O(x, y). \end{aligned} \quad (3.14)$$

In order to easily keep track of the order in α_S of each term, the coupling constant is extracted from the respective integrals. The virtual and real emission contributions are separately IR divergent, which is indicated by the notation $R(x, y)/y$ for the real emission contribution. The divergence exhibited by the virtual contribution is implicitly given in terms of a pole in $\epsilon = (d-4)/2$, $V(x) = -B(x)/\epsilon + \bar{V}(x)$. Using the subtraction formalism, an auxiliary cross section $\alpha_S A(x, y)/y$ which resembles the divergences in the real emission part is introduced, i.e. $A(x, y) \mapsto B(x)$ as $y \mapsto 0$. Hence, the NLO prediction is modified in the following way,

$$\begin{aligned} \langle O \rangle_{NLO} &= \int_m dx B(x) O(x) \\ &+ \alpha_s \int_m dx \left[V(x) + \int_1 dy \frac{A(x, y)}{y^{1-\epsilon}} \right] O(x) \\ &+ \alpha_s \int_{m+1} dx dy \frac{R(x, y) O(x, y) - A(x, y) O(x)}{y}. \end{aligned} \quad (3.15)$$

The notation $A(x, y)/y^{1-\epsilon}$ indicates that the collinear divergences are expressed as poles in ϵ and analytically cancel against those from the virtual contribution. As a result, all integrals are finite and numerically integrable in $d = 4$ dimensions.

In comparison, a parton shower starting off the Born matrix element gives the following prediction,

$$\langle O \rangle_{PS} = \int_{m+1} dx dy B(x) \left[\delta(y) \Delta(x) + \theta(y - \mu) \alpha_s \frac{P(x, y)}{y} \Delta(x) \right] O(x, y), \quad (3.16)$$

where the first term in square brackets denotes unresolved branching. μ is an infrared shower cutoff, $P(x, y)$ the splitting kernels associated with the final state partons, and

$\Delta(x)$ the Sudakov form factor which we recall from Section 3.3 in a compactified notation,

$$\begin{aligned}\Delta(x) &= e^{-\alpha_s \int_\mu^1 dy' \frac{P(x,y')}{y'}} \\ &= 1 - \alpha_s \int_\mu^1 dy' \frac{P(x,y')}{y'} + \mathcal{O}(\alpha_s^2).\end{aligned}\quad (3.17)$$

Thus, the parton shower prediction to $\mathcal{O}(\alpha_s)$ is given by

$$\langle O \rangle_{PS} = \int_m dx B(x) O(x) + \alpha_s \int_{m+1} dx dy \frac{P(x,y)}{y} [O(x,y) - O(x)] B(x) + \mathcal{O}(\alpha_s^2).\quad (3.18)$$

Again, we see that if the parton shower starts off the exact NLO calculation (3.15), additional terms formally of $\mathcal{O}(\alpha_s)$ are added, and the correct result is not obtained due to double counting. Specifically, combining Eq. (3.15) with the prediction (3.18) given by the subsequent parton shower yields

$$\begin{aligned}\langle O \rangle_{NLO+PS} &= \int_m dx B(x) O(x) \\ &+ \alpha_s \int_m dx \left[V(x) + \int_1 dy \frac{A(x,y)}{y^{1-\epsilon}} \right] O(x) \\ &+ \alpha_s \int_{m+1} dx dy \frac{R(x,y) O(x,y) - A(x,y) O(x)}{y} \\ &+ \alpha_s \int_{m+1} dx dy \frac{P(x,y)}{y} [O(x,y) - O(x)] B(x) \\ &+ \mathcal{O}(\alpha_s^2),\end{aligned}\quad (3.19)$$

where the additional term of $\mathcal{O}(\alpha_s)$ stems from parton shower emission off the Born part. Note that further terms of $\mathcal{O}(\alpha_s^2)$ are given by three distinct contributions, namely two or more successive splittings off the Born part, emission off the subtracted virtual contribution or emission off the subtracted real emission contribution.

The basic idea of matching parton showers with fixed-order matrix element calculations is to modify the matrix element in a way such that after parton shower evolution, the correct result at NLO accuracy (3.15) is recovered. Thus, the corrections of $\mathcal{O}(\alpha_s)$ that are added on top of a fixed-order calculation during the parton shower, cf. Eq. (3.19), are removed from the cross section by hand. The matched matrix element which enters the simulation reads

$$\begin{aligned}\langle O \rangle_{matched}^{NLO} &= \int_m dx B(x) O(x) \\ &+ \alpha_s \int_m dx [\bar{V}(x) + A_{\text{finite}}(x)] O(x) \\ &+ \alpha_s \int_{m+1} dx dy \frac{P(x,y) B(x) - A(x,y)}{y} O(x) \\ &+ \alpha_s \int_{m+1} dx dy \frac{R(x,y) - P(x,y) B(x)}{y} O(x,y),\end{aligned}\quad (3.20)$$

where all divergences have been explicitly cancelled. Combining Eqs. (3.18) and (3.20), the fixed-order calculation at NLO accuracy is reproduced together with all parton shower corrections that enter beyond NLL. The implementation of an automated matching procedure forms the core of the `Herwig++ Matchbox` module, of which we give an overview in Chapter 6. Note that $A(x,y)$ and $P(x,y)$ feature the same dipole-type structure and

that there is some freedom of defining these terms away from the quasi-collinear limit, such that the matched matrix element (3.20) can be significantly simplified. Common matching schemes are MC@NLO [25] and POWHEG [26], which are both implemented in Herwig++.

In the POWHEG scheme, matrix element corrections are applied to the parton shower, i.e. the splitting kernels are expressed by

$$\frac{P^{\text{POWHEG}}(x, y)}{y} = \frac{R(x, y)}{y} \Big/ B(x). \quad (3.21)$$

Thus, the last term on the right-hand side of Eq. (3.20) vanishes. In turn, the splitting kernels of the first parton shower emission are determined by the full radiative corrections.

Conversely, in the MC@NLO scheme, the third term on the right-hand-side of Eq. (3.20) vanishes by choosing the auxiliary cross section of the subtraction scheme according to the splitting kernels of the parton shower,

$$\frac{A^{\text{MC@NLO}}(x, y)}{y} = \frac{P(x, y)}{y} \cdot B(x). \quad (3.22)$$

With the implementation of a dipole-type parton shower, this matching prescription is compatible with the Catani-Seymour subtraction formalism since the same dipoles are used. A subtlety of MC@NLO matching is that it has to be assured that the first emission is also the hardest emission in terms of transverse momentum p_{\perp} . This constraint is naturally respected by the dipole shower as its evolution variable is given by p_{\perp} .

For the sake of completeness we also note that other matching schemes are possible, particularly mixed schemes which allow to interpolate smoothly between the two methods outlined above.

The Herwig++ Event Generator and Analysis Tools

Herwig++ [4] is a multi-purpose Monte Carlo event generator designed for the simulation of lepton-lepton, lepton-hadron and hadron-hadron scattering. It provides a full simulation of high energy collisions including the hard process, parton shower, hadronization and particle decays, as well as multiple scatterings (for the latter see e.g. Ref. [27]). We give an overview of those features which are most important for electron-positron annihilation, since this lies in the focus of this work.

4.1. Hard Process

The hard process handles the high p_{\perp} interaction of incoming particles extracted from the beams at an energy scale where perturbation theory is valid. Matrix elements are typically implemented at LO, though NLO corrections are available for some processes. Leading higher-order QCD corrections are resummed by the parton shower, giving rise to additional parton radiation. Outgoing momenta are sampled according to the hard cross section. In hadronic processes, a parton is first extracted from the hadron with a weight given by parton distribution functions (PDF). Colour flows are assigned to all external partons, which serves as an important initial condition for the parton shower as well as for multiple scattering. In Herwig++ all matrix elements which will be taken into account during the simulation are specified by the user.

A large variety of hard processes that are not implemented in Herwig++ can be included via the Les Houches Accord interface [28, 29] and extensions to allow calculations at NLO accuracy have been proposed as well. This standard file format allows the exchange of data between matrix element generators such as VBFNLO [30] or MadEvent/MadGraph [31] and multi-purpose event generators (besides Herwig++, common event generators are Pythia [5] and SHERPA [6]).

In this work, we did not use this interface but directly implemented the massive extension of $e^+e^- \mapsto q\bar{q}$ at NLO.

4.2. Parton Shower

The parton shower performs the perturbative transition from the hard process down to a scale at the onset of non-perturbative effects, where hadronization models take over.

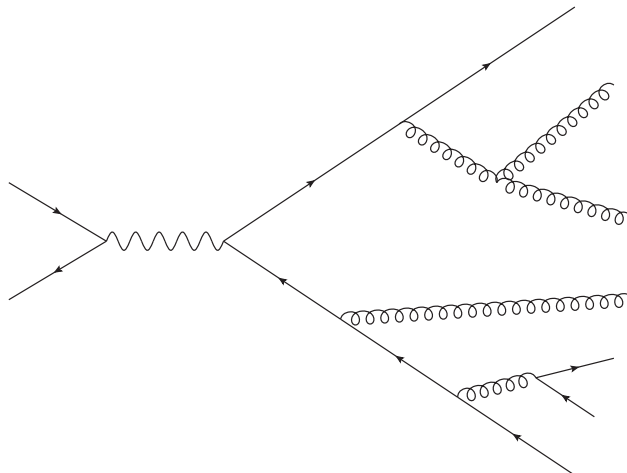


Figure 4.1.: Sketch of a sample parton shower in leptonic collisions.

Through successive parton emissions, higher orders in perturbation theory are effectively resummed. In this way, any outgoing parton from the hard process initiates a branching cascade (“final state radiation”). At each step, the Sudakov form factor $\Delta((p_{\perp}^{(i)})^2, (p_{\perp}^{(i+1)})^2)$ is used to determine the scale of the next splitting. The evolution terminates when no splitting above the infrared cutoff μ_{IR} can be selected. Fig. 4.1 depicts a sample final-state parton shower.

In hadronic collisions, initial state partons undergo parton showering as well, starting at the hard process and evolving backwards in time from higher to lower scales. Again, the shower terminates when the evolution variable p_{\perp}^2 falls below μ_{IR} . The parton is then extracted from the hadron if the shower evolution stopped at a valence (anti-)quark. If this is not the case, additional splittings are imposed in order to force the evolution to terminate with a valence (anti-)quark [32]. All partons emitted during initial state radiation may themselves initiate further final state radiation.

The infrared cutoff μ_{IR} is a free parameter of the parton shower and is constrained by the requirement that perturbative QCD is still possible at this energy scale. Its value is determined by tuning the simulation results to experimental data, cf. Section 4.5 and Chapter 8. Typically, separate values for initial-state and final-state branching are implemented.

An implementation of a dipole shower in the massless approximation is already available in the *Herwig++* `DipoleShower` module, and a detailed description of the massive dipole shower which we implemented in the course of this work is given in Chapter 5. Note that the standard implementation in *Herwig++* is given by a monopole-type shower ($1 \mapsto 2$ splittings) [33] which also takes finite parton masses into account. Both previous implementations can serve as a reference for comparisons with our simulation results.

4.3. Hadronization

After the shower evolution has terminated, the parton-level final state is converted into hadrons that can be experimentally observed. Hence, hadronization is very sensitive to the details of the partonic final state and it is absolutely crucial to adjust the hadronization parameters once a new shower has been implemented. We will give a brief overview, focusing on those quantities which are sensitive to our parton shower. *Herwig++* uses a cluster hadronization model as originally proposed in Ref. [34].

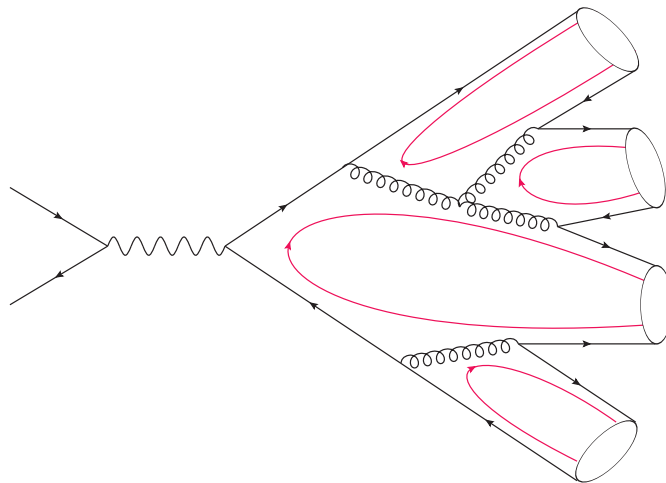


Figure 4.2.: Parton shower and clustering in a typical LEP event. Gluons are non-perturbatively split into quark-antiquark pairs, then clusters are formed from each colour-singlet quark-antiquark pair. Colour flow is unambiguously determined by the flavour structure of the parton shower and represented by red lines.

Before hadronization, all partons are put on their respective constituent mass shells. Gluons are then non-perturbatively split into quark-antiquark pairs. From this state, colour-singlet clusters are formed with the momentum given by the sum of the momenta of the constituent (colour-connected) partons, see Fig. 4.2. These clusters can be interpreted as highly excited hadron resonances. Before decaying into the observed hadrons, heavy clusters (of mass M) are split if the following condition holds,

$$M^{\text{Cl}_{\text{pow}}} \geq \text{Cl}_{\text{max}}^{\text{Cl}_{\text{pow}}} + (m_1 + m_2)^{\text{Cl}_{\text{pow}}}. \quad (4.1)$$

$m_{1,2}$ are the masses of the constituent partons of the cluster and Cl_{max} , Cl_{pow} are parameters of the hadronization model that are not known from first principles. In practice, separate values of both Cl_{max} and Cl_{pow} are used for clusters containing light (u, d, s), charm or bottom quarks respectively. Thereby, the description of bottom and charm hadrons is further improved, which is important for identified particle spectra. If a cluster $q_i \bar{q}_j$ is selected to be split, a $q\bar{q}$ pair (quark mass m_q) is popped from the vacuum and the new clusters read $q_i \bar{q}$ and $q\bar{q}_j$ respectively. The masses are given by

$$\begin{aligned} M_1 &= m_1 + (M - m_1 - m_q) \mathcal{R}_1^{1/P_{\text{split}}}, \\ M_2 &= m_2 + (M - m_2 - m_q) \mathcal{R}_2^{1/P_{\text{split}}}, \end{aligned} \quad (4.2)$$

where $M_{1,2}$ denote the masses of the splitting products, $\mathcal{R}_{1,2}$ are random numbers and P_{split} is an adjustable parameter that takes separate values for clusters containing light, charm or bottom quarks. Note that in hadron collisions, additional clusters are formed from the beam remnants and are treated separately. For a treatment of multiple interactions, see e.g. Ref. [27].

In the final step of the cluster hadronization model, each cluster is decayed into a pair of hadrons. For heavy clusters, both mesonic and baryonic decays are possible and the respective rates can be controlled in order to obtain agreement with experimental data. By default, partons that stem from the final state of the parton shower retain their directions (and so do their respective hadrons), whereas in general the decay products are distributed isotropically. All hadron momenta are smeared through an angle θ_{smear} according to a

Gaussian distribution,

$$\cos \theta_{\text{smear}} = 1 + \text{Cl}_{\text{smr}} \log \mathcal{R}. \quad (4.3)$$

Again, \mathcal{R} is a random number and the parameter Cl_{smr} can be separately set for clusters containing light, charm or bottom quarks.

4.4. The Rivet Analysis Toolkit

4.4.1. Overview

Besides its own analysis tools, *Herwig++* features an output via the HepMC event record interface. The Rivet generator validation system [35] is both a library of experimental analyses and provides tools for calculating physical observables at the simulation-level from the event record. Through this procedure, the analysis is completely separated from the MC generator behaviour. At the moment, more than 100 verified analyses from various collider experiments are included. Throughout this work we made use of Rivet to compare our simulation output to experimental results.

4.4.2. New Analysis

Rivet has been designed in a way to simplify the coding of new analyses by the user. As will be evident from Chapter 8, identified particle spectra are crucial for tuning the free parameters of the simulation to experimental data. For this reason, we implemented a new analysis that is not yet included in the set of standard analyses. Based on experimental results published by the SLD Collaboration [36], the new observables are the spectra of charged pions π^\pm , charged kaons K^\pm and (anti-)protons p^\pm in (*uds*), *c* and *b* quark events, respectively, and several ratios. These observables play an important role when we investigate the impact of our implementation, see Chapter 8.

4.5. The Professor Tuning System

The Professor tuning system [37] was designed for tuning model parameters of a Monte Carlo event generator to experimental data, where simulation results are by default obtained using the Rivet analysis toolkit outlined in the previous section. Best possible agreement is sought for by adjusting the free parameters of the simulation. For that purpose, a large number of generator runs with different sets of parameters is required, where each run corresponds to one point in the multi-dimensional parameter space under consideration. Typically, these parameter points are sampled randomly within a predefined hypercube characterizing the physical ranges of the parameters. In contrast to brute-force methods, Professor interpolates between the individual parameter points and is thus able to find a best fit which most likely does not coincide with one of the sampled points in parameter space.

For this purpose, a certain number of runs is accumulated into several run combinations. Each run combination is treated separately in order to obtain systematic control over the tuning results. The generator’s response to parameter changes as present in the various independent runs of a run combination is parametrized, using a cubic polynomial by default. This is done by the `prof-interpolate` routine bin-by-bin for every observable. Owing to this method, different weights can not only be assigned to certain observables, but also to particular regions within these distributions. The minimum number of runs necessary for the tune is given by the number of free parameters of the interpolation function. For example, the tuning of ten free parameters to experimental data by making use of a cubic polynomial requires a minimum of 286 independent runs to act as “anchor points” for the

fit. However, significant oversampling is recommended by the developers in order to obtain a more robust fit.

Before the actual tuning stage, sensitivity plots of all the observables to shifts in parameter space can be produced. Tuning is performed for all respective run combinations by making use of the `prof-tune` method. A goodness of fit function is defined in a manner where statistical errors at simulation level enter as well, such that having only a relatively small number of events for each run is sufficient. Finally, the tuning results for all distinct run combinations are combined and the results can be investigated in scatter plots.

We mentioned the fact that it is recommended to create several independent run combinations in order to obtain a robust tune. These sets of runs are not required to be disjoint, but should only have a reasonable overlap. In our case, we chose to oversample by a factor of three and performed tuning for 100 different run combinations. Our particular strategy of tuning a large set of parameters to data is described in Chapter 8, together with the results.

Massive Parton Shower with Local Recoils

Our aim was the implementation of a new dipole-type parton shower as described in Chapter 3 that takes full account of finite parton masses. The shower is constructed from the kinematic variables and splitting kernels introduced in Ref. [18], where the reader is referred to for details. However, we present all additional ingredients which we derived in the course of this work and which are necessary for an implementation in an event generator. The considerations in this chapter are a generalization of the dipole shower for massless partons, as developed in Ref. [13]. We will not recall the special case of vanishing parton masses, but do stress the fact that our parametrization reproduces the exact massless limit as laid out in Ref. [13] at each step of the process.

In the following, we present a derivation for the parametrization of the splitting momenta, the phase-space factorization and give an expression of the resulting splitting probability for all possible emitter-spectator pairs. Recall Fig. 3.1 for a visualization of the splittings for the respective emitter-spectator combinations.

5.1. Final-State Radiation and Final-State Spectator

In the Catani-Seymour dipole formalism, massive partons only appear in the final state. Hence, we first present final-state radiation with a final-state spectator which is the most generic case. In this thesis, it also is the most relevant case since we study the LEP experiment in detail.

5.1.1. Kinematics

The dipole-type splitting of a mother parton with momentum p_i in two daughter partons with respective momenta q_i, q can be described by a pair of Lorentz-invariant variables y and z [18],

$$y = \frac{q_i \cdot q}{q_i \cdot q + q_i \cdot q_j + q \cdot q_j}, \quad z = \frac{q_i \cdot q_j}{(q_i + q) \cdot q_j}. \quad (5.1)$$

The spectator observes a recoil and its momentum is rescaled from p_j to q_j during the splitting. y is a measure of the invariant mass of the splitting products, whereas z denotes how the momentum of the mother parton is split amongst the two daughter partons. In our implementation, the evolution variable of the shower is given by transverse momentum (see Chapter 3), whose definition in terms of Lorentz scalars is not obvious. Hence,

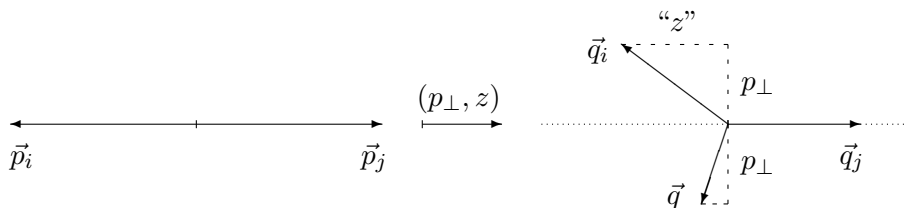


Figure 5.1.: Schematic depiction of the final-final splitting kinematics in the dipole’s rest frame. The momentum p_i of the emitter is divided among the splitting products according to z , symbolized by the notation “ z ”. Both momenta acquire transverse momentum p_\perp with respect to the orientation of the dipole but in opposite direction, respectively. The spectator momentum observes a recoil, its direction is however preserved. Owing to the dipole picture, momentum conservation is applied and all partons are on mass shell.

a Sudakov decomposition of the daughter momenta in terms of the parent momenta $p_{i,j}$ and transverse momentum k_\perp would be preferable. Following the parametrization given in Ref. [13] for the massless case, the daughter momenta are given by $q_n \equiv q_n(p_i, p_j; p_\perp, z)$, where p_\perp denotes the absolute value of transverse momentum k_\perp . See Fig. 5.1 for an illustration of the physical splitting variables (p_\perp, z) . It is noteworthy that the splitting kernels have been derived using the variables y, z presented in Eq. (5.1), i.e. a bijective mapping $(y, z) \leftrightarrow (p_\perp, z)$ is absolutely crucial for a consistent description of parton splittings in our formalism. Under these conditions and due to the fact that all partons may feature a finite mass, an applicable parametrization with the desired properties could however not be found.

Instead, we present an explicit, component-wise parametrization similar to the ones given in Refs. [21, 22]. We work in the rest frame of the dipole and use the following abbreviations¹

$$\begin{aligned}
 Q &= p_i + p_j = q_i + q + q_j, \\
 s &= Q^2, \\
 \bar{s} &= s - m_i^2 - m^2 - m_j^2, \\
 \mu_i &= \frac{m_i}{\sqrt{s}}, \quad \mu = \frac{m}{\sqrt{s}}, \quad \mu_j = \frac{m_j}{\sqrt{s}}.
 \end{aligned} \tag{5.2}$$

From the definitions of z and y immediately follows

$$2q_i \cdot q = y\bar{s}, \tag{5.3}$$

$$2q_i \cdot q_j = z(1-y)\bar{s}, \tag{5.4}$$

$$2q \cdot q_j = (1-z)(1-y)\bar{s}. \tag{5.5}$$

The centre-of-mass frame is oriented in such a way that the spectator momentum p_j points along the (positive) z axis. The daughter parton momenta are decomposed as follows,

$$q_i = (q_i^0, p_\perp \cos \theta, -p_\perp \sin \theta, q_i^\parallel), \tag{5.6}$$

$$q = (q^0, -p_\perp \cos \theta, p_\perp \sin \theta, q^\parallel), \tag{5.7}$$

$$q_j = (q_j^0, 0, 0, q_j^\parallel), \tag{5.8}$$

¹We choose the masses of the partons after splitting to be expressed by minuscule letters, $m_i^2 = q_i^2$ etc., those of the partons before splitting by capital letters, $M_i^2 = p_i^2$ etc.

where the particle energies q_n^0 and longitudinal momentum components q_n^{\parallel} are defined in the following way,

$$q_n^0 = \frac{Q \cdot q_n}{\sqrt{s}}, \quad q_n^{\parallel} = |\vec{q}_n| \cos(\angle \vec{q}_n, \vec{q}_j) = \frac{q_n^0 q_j^0 - q_n \cdot q_j}{\sqrt{(q_j^0)^2 - q_j^2}}. \quad (5.9)$$

The physical transverse momentum is defined to be the absolute value of the remaining spatial components in the dipole's rest frame, given by

$$\begin{aligned} p_{\perp} &\equiv p_{\perp}^{\text{phys}} = |q_i^{\perp}| = \left((q_i^0)^2 - (q_i^{\parallel})^2 - m_i^2 \right)^{1/2} \\ &= |q^{\perp}| = \left((q^0)^2 - (q^{\parallel})^2 - m^2 \right)^{1/2}. \end{aligned} \quad (5.10)$$

It is evident that this parametrization preserves exact energy-momentum conservation. Additionally, the direction of the emitter remains the same, which is a crucial requirement in our formalism. From the relations (5.3)-(5.5), the respective components are easily spelt out. The parton energies explicitly read

$$q_i^0 = \frac{\bar{s}(1 - (1 - z)(1 - y)) + 2m_i^2}{2\sqrt{s}}, \quad (5.11)$$

$$q^0 = \frac{\bar{s}(1 - z(1 - y)) + 2m^2}{2\sqrt{s}}, \quad (5.12)$$

$$q_j^0 = \frac{\bar{s}(1 - y) + 2m_j^2}{2\sqrt{s}}; \quad (5.13)$$

the remaining momentum components are functions of the particle energies and masses.

5.1.2. A new Evolution Parameter

In the previous section, we constructed a kinematic splitting parametrization from a pair of variables (y, z) which fulfils the desired properties. The variables used in the shower, (p_{\perp}, z) , can simply be read off the momentum vectors. However, the inverse mapping $(p_{\perp}, z) \mapsto (y, z)$ is not feasible. We therefore present a practically more useful definition p_{\perp}^{coll} in the following.

In the quasi-collinear limit (in which the shower approximation holds), a Sudakov decomposition in terms of k_{\perp} and z can easily be given²,

$$\begin{aligned} q_i &= zp + k_{\perp} - \frac{k_{\perp}^2 + z^2 M_i^2 - m_i^2}{z} \frac{n}{2p \cdot n}, \\ q &= (1 - z)p - k_{\perp} - \frac{k_{\perp}^2 + (1 - z)^2 M_i^2 - m^2}{1 - z} \frac{n}{2p \cdot n}, \end{aligned} \quad (5.14)$$

where p points towards the collinear direction and fulfils the property $p^2 = M_i^2$, n is a light-like auxiliary vector along the collinear direction, and k_{\perp} is the spatial momentum component orthogonal to both p and n , $(k_{\perp}^{\mu})^2 = -(p_{\perp}^{\text{coll}})^2$. From the definition of y , Eq. (5.1), we obtain the desired relations,

$$\begin{aligned} y &= \frac{(p_{\perp}^{\text{coll}})^2 + (1 - z)^2 m_i^2 + z^2 m^2}{\bar{s}z(1 - z)} \\ \Leftrightarrow (p_{\perp}^{\text{coll}})^2 &= \bar{s}yz(1 - z) - (1 - z)^2 m_i^2 - z^2 m^2. \end{aligned} \quad (5.15)$$

²Recall that the transverse momentum and all parton masses are understood to be uniformly vanishing in this expression.

In case of a massless spectator parton, this expression coincides with the physical transverse momentum. Furthermore, in the quasi-collinear limit, p_{\perp}^{phys} and p_{\perp}^{coll} coincide for arbitrary parton masses. Since the shower approximation is performed in this phase-space region as well, both quantities can be equivalently used as evolution parameter presumably without changing the shower prediction of the leading-logarithmic contributions. For performance reasons, p_{\perp}^{coll} will be used in the algorithm and the corresponding replacement $p_{\perp} \mapsto p_{\perp}^{\text{coll}}$ has to be made in the respective formulæ.

5.1.3. Phase Space and Splitting Probability

The kinematic parametrization gives rise to the phase-space factorization [18]

$$d\phi(q_i, q, q_j|Q) = d\phi(p_i, p_j|Q) dq_i(p_i, p_j) \Theta(1 - \mu_i - \mu - \mu_j), \quad (5.16)$$

where the single-parton phase space is given by

$$\begin{aligned} dq_i(p_i, p_j) &= \frac{1}{16\pi^2} \frac{s \bar{s}}{\sqrt{\lambda(s, M_i^2, M_j^2)}} (1-y) dy dz \frac{d\phi}{2\pi} \\ &= \frac{1}{16\pi^2} \frac{s}{\sqrt{\lambda(s, M_i^2, M_j^2)}} (1-y(p_{\perp}^2, z)) dp_{\perp}^2 \frac{dz}{z(1-z)} \frac{d\phi}{2\pi}. \end{aligned} \quad (5.17)$$

The Jacobian determinant used for the derivation of the latter expression directly follows from Eq. (5.15). λ is the triangular (Källén) function,

$$\lambda(a, b, c) = (a + b + c)^2 - 4(ab + ac + bc). \quad (5.18)$$

The (purely kinematic) boundary of the full, unconstrained phase space is determined by the limits of the angle between emitter and spectator given in Eq. (5.9),

$$|\cos(\langle \vec{q}_i, \vec{q}_j \rangle)| \leq 1, \quad (5.19)$$

and explicitly reads

$$\begin{aligned} \phi &\in (0, 2\pi), \\ y_{\pm} &= \frac{2m_i m}{\bar{s}}, \quad y_{\pm} = 1 - \frac{2m_j(\sqrt{s} - m_j)}{\bar{s}}, \\ z_{\pm} &= \frac{(2m_i^2 + \bar{s}y)(1-y) \pm \sqrt{y^2 - y_{\pm}^2} \sqrt{(2m_j^2 + \bar{s}(1-y))^2 - 4m_j^2 s}}{2(1-y)(m_i^2 + m^2 + \bar{s}y)}. \end{aligned} \quad (5.20)$$

Yet the phase space has to be further restricted due to evolution ordering. In order to reproduce the correct leading logarithms, the transverse momentum has to be further constrained, $\mu < p_{\perp} < \min(p_{\perp}^{\text{last}}, p_{\perp}^{\text{max}}) \equiv p_{\perp}^{\text{hard}}$ (μ being an infrared cutoff). The corresponding phase-space boundaries are obtained by solving $y(p_{\perp}, z'_{\pm}) \leq y_{\pm}$ for z'_{\pm} . We obtain³

$$p_{\perp}^{\text{max}} = \sqrt{\lambda(\mu_i^2, \mu^2, (1-\mu_j)^2)} \frac{\sqrt{s}}{2 - 2\mu_j}, \quad (5.21)$$

$$z'_{\pm} = \frac{1}{2(1-\mu_j)^2} \left[1 + \mu_i^2 - \mu^2 + \mu_j^2 - 2\mu_j \pm \sqrt{\lambda(\mu_i^2, \mu^2, (1-\mu_j)^2)} \sqrt{1 - \frac{p_{\perp}^2}{(p_{\perp}^{\text{hard}})^2}} \right]. \quad (5.22)$$

³In fact, by simply solving the inequality above we obtain the quoted expressions strictly only if $p_{\perp}^{\text{last}} \geq p_{\perp}^{\text{max}}$. However, we want to constrain the phase space particularly due to ordering in transverse momentum which is exactly the opposite case. We are therefore led to apply the rescaled value of p_{\perp} into the naïve expression of the z boundaries, $z'_{\pm}(p_{\perp}) \mapsto z'_{\pm}(p_{\perp} \cdot p_{\perp}^{\text{max}}/p_{\perp}^{\text{hard}})$, which then yields the quoted expression. The same considerations hold for the other splittings depicted in the remainder of this chapter as well.

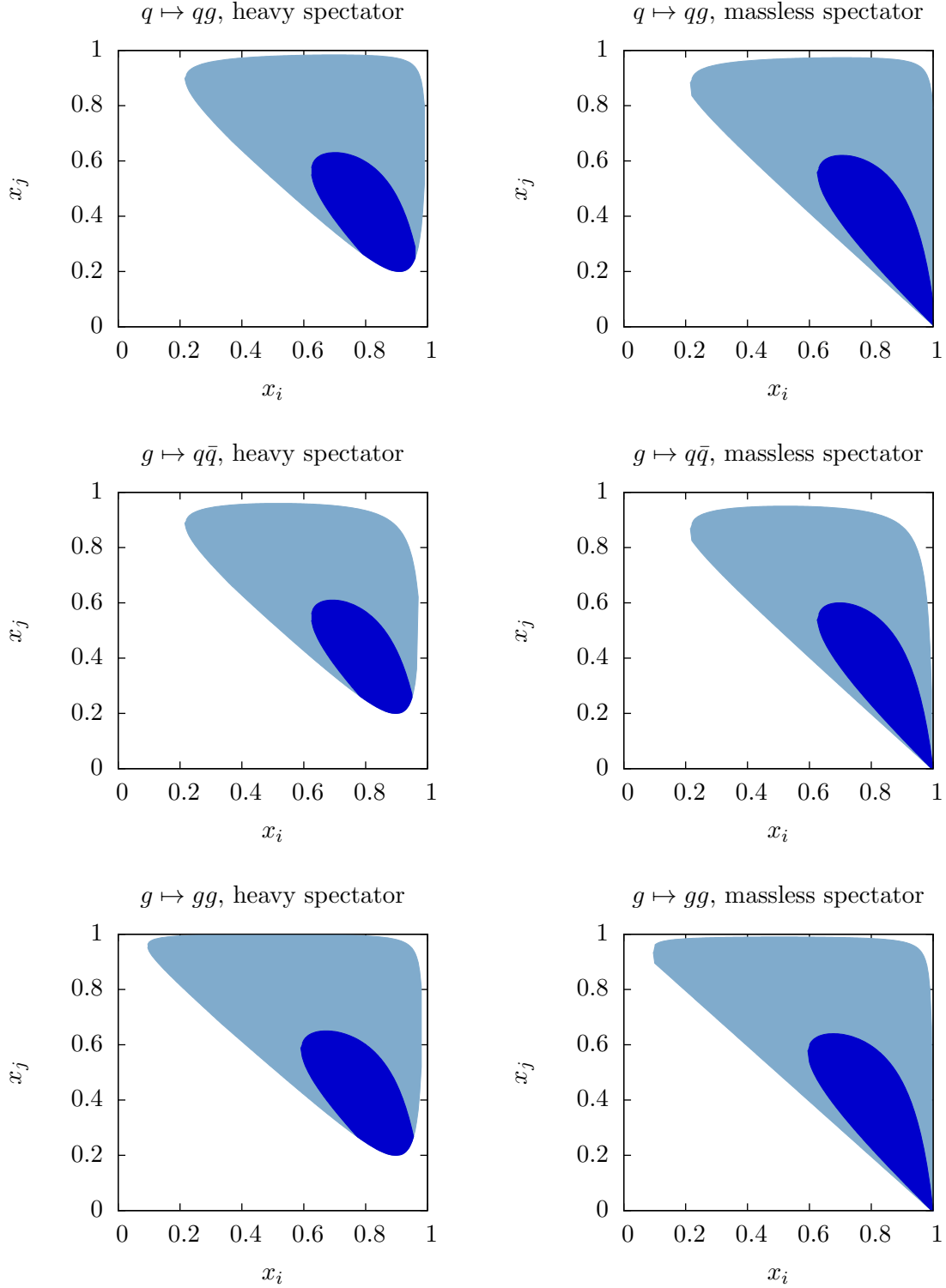


Figure 5.2.: Allowed phase-space regions for emission off a final-final dipole expressed in Dalitz variables $x_k = 2Q \cdot q_k/Q^2$ for a dipole of mass $\sqrt{s} = 100$ GeV, infrared cutoff $\mu = 5$ GeV with the quark mass set to $m_q = 10$ GeV. The light-shaded region is accessible from emissions off the emitter parton i when starting at the hard scale. The dark-shaded region is excluded when starting at a lower scale $p_{\perp}^{\text{hard}} = 30$ GeV. The impact of the finite infrared cutoff can be most easily seen in the massless case on the lower right. Also, it is obvious that heavy partons tend to demand a larger value of x_k compared to the similar configuration with a massless parton. The parton mass and the infrared cutoff are exaggerated for illustration purposes.

For a p_\perp -ordered parton shower like the one we are considering here, both kinematic and evolution boundaries have to be taken into account because they address different phase-space regions. The available phase space is depicted in Fig. 5.2 for several dipole configurations.

The final-final splitting kernels take the form (averaged over the azimuthal angle)

$$\frac{8\pi\alpha_S}{(q_i + q)^2 - M_i^2} \langle V(y, z) \rangle, \quad (5.23)$$

such that together with the phase-space factorization (5.17), the splitting probability follows as

$$d\mathcal{P}(y, z) = \frac{\alpha_S}{2\pi} \langle V(y, z) \rangle \frac{\bar{s}}{\sqrt{\lambda(s, M_i^2, M_j^2)}} \frac{s(1-y)}{m_i^2 + m^2 - M_i^2 + \bar{s}y} dy dz. \quad (5.24)$$

Note that large invariant masses of the emitter-emission pair, which correspond to large-angle hard splittings, are suppressed as an effect of the finite recoil. Also note that all quantities can safely be taken to the limit of vanishing masses, where the respective expressions from the massless calculation follow (cf. Refs. [13, 17, 24]).

5.2. Final-State Radiation and Initial-State Spectator

5.2.1. Kinematics

In the case of an initial-state spectator (denoted by the subscript a), the momentum transfer between the initial state and the final state remains invariant under the considered splitting,

$$Q = p_i - p_a = q_i + q - q_a. \quad (5.25)$$

A simple crossing of the kinematics derived in the previous section, $p_j \mapsto -p_a$, $q_j \mapsto -q_a$, however, is not possible since in general a ‘‘centre-of-mass’’ frame of Q does not exist. Nevertheless, we can instead give a Sudakov decomposition of the daughter momenta in terms of the parent momenta $p_{i,j}$ and transverse momentum k_\perp , since the spectator is massless and its 4-momentum can be simply rescaled,

$$\begin{aligned} q_i &= zp_i + \frac{p_\perp^2 + m_i^2 - z^2 M_i^2}{z\bar{s}} p_a + k_\perp, \\ q &= (1-z)p_i + \frac{p_\perp^2 + m^2 - (1-z)^2 M_i^2}{(1-z)\bar{s}} p_a - k_\perp, \\ q_a &= \left(1 + \frac{p_\perp^2 + (1-z)m_i^2 + zm^2 - z(1-z)M_i^2}{z(1-z)\bar{s}} \right) p_a, \end{aligned} \quad (5.26)$$

where we defined

$$\bar{s} = 2p_i \cdot p_a = M_i^2 - Q^2. \quad (5.27)$$

k_\perp is perpendicular to both dipole momenta before splitting, $k_\perp \cdot p_i = k_\perp \cdot p_a = 0$. It is taken to be purely spacelike in a frame where $p_i + p_a$ is at rest, and we define the evolution variable as $p_\perp^2 = -k_\perp^2$. The kinematic variables are defined as follows [18],

$$x = \frac{q_i \cdot q_a + q \cdot q_a - q_i \cdot q + \frac{1}{2}(M_i^2 - m_i^2 - m^2)}{(q_i + q) \cdot q_a}, \quad z = \frac{q_i \cdot q_a}{(q_i + q) \cdot q_a}, \quad (5.28)$$

such that by virtue of the parametrization given in Eq. (5.26), x is expressed in terms of the shower variables (p_\perp, z) by

$$x = \left(1 + \frac{p_\perp^2 + (1-z)m_i^2 + zm^2 - z(1-z)M_i^2}{z(1-z)\bar{s}} \right)^{-1}. \quad (5.29)$$

Recall that the initial-state spectator is evolved backwards in time, i.e. p_a enters the hard process and q_a is extracted from the incoming hadron (in case of only one splitting; however, a generalization is straightforward).

5.2.2. Phase Space and Splitting Probability

Our parametrization yields the phase-space factorization

$$d\phi(q_i, q, q_a|Q + q_a) = d\phi(p_i, p_a|Q + p_a) \frac{d\phi}{2\pi} \frac{x}{16\pi^2} \frac{dz}{z(1-z)} dp_{\perp}^2, \quad (5.30)$$

in agreement with Ref. [18]. Since the momentum of the initial-state spectator is rescaled, for the relevant measure at hadron level, the parton distribution function f_a and the kinematic factor of the partonic flux have to be taken into account,

$$\frac{f_a(x_a)}{4q_a \cdot p_b} d\phi(q_i, q, q_a|Q + q_a) dx_a = \left(\frac{f_a(x_a/x)}{f_a(x_a)} \theta(x - x_a) \frac{d\phi}{2\pi} \frac{x}{16\pi^2} \frac{dz}{z(1-z)} dp_{\perp}^2 \right) \frac{f_a(x_a)}{4p_a \cdot p_b} d\phi(p_i, p_a|Q + p_a) dx_a. \quad (5.31)$$

x_a denotes the momentum fraction of the spectator parton with respect to the incoming hadron (momentum P_a) before taking the recoil. In the flux factor, the momentum p_b of the second incoming particle enters. Considering the spectator momentum, we obtain the following limiting condition

$$q_a = \frac{1}{x} p_a = \frac{x_a}{x} P_a \stackrel{!}{<} P_a \Rightarrow x > x_a. \quad (5.32)$$

Using Eq. (5.29), the phase-space boundary turns out to be given by

$$\mu^2 < p_{\perp}^2 < \frac{s^*}{4x_a} \lambda \left(1, \frac{x_a m_i^2}{s^*}, \frac{x_a m^2}{s^*} \right) \equiv (p_{\perp}^{\max})^2, \quad (5.33)$$

$$z_{\pm} = \frac{1}{2} \left(1 + \frac{x_a(m_i^2 - m^2)}{s^*} \pm \sqrt{\lambda \left(1, \frac{x_a m_i^2}{s^*}, \frac{x_a m^2}{s^*} \right)} \sqrt{1 - \frac{p_{\perp}^2}{(p_{\perp}^{\text{hard}})^2}} \right),$$

where μ denotes an infrared cutoff and $s^* \equiv \bar{s}(1 - x_a) + x_a M_i^2$. Again, the hard scale of the transverse momentum is given by $p_{\perp}^{\text{hard}} = \min(p_{\perp}^{\text{last}}, p_{\perp}^{\text{max}})$.

The additional, purely kinematic phase-space boundaries stemming from the finite parton masses read [18]

$$x_+ = 1 + M_i^2 - (\mu_i + \mu)^2, \quad (5.34)$$

$$z_{\pm} = \frac{1 - x + M_i^2 + \mu_i^2 - \mu^2 \pm \sqrt{(1 - x + M_i^2 - \mu_i^2 - \mu_j^2)^2 - 4\mu_i^2 \mu^2}}{2(1 - x + M_i^2)}, \quad (5.35)$$

where the rescaled parton masses are defined as $\mu_n = m_n/\sqrt{2p_i \cdot q_a}$ (again, the capital letter M denotes incoming partons). The allowed phase-space region for final-initial branching is visualized in Fig. 5.3.

The final-initial splitting kernels take the form (averaged over the azimuthal angle)

$$\frac{8\pi\alpha_S}{(q_i + q)^2 - M_i^2} \frac{1}{x} \langle V(p_{\perp}^2, z) \rangle, \quad (5.36)$$

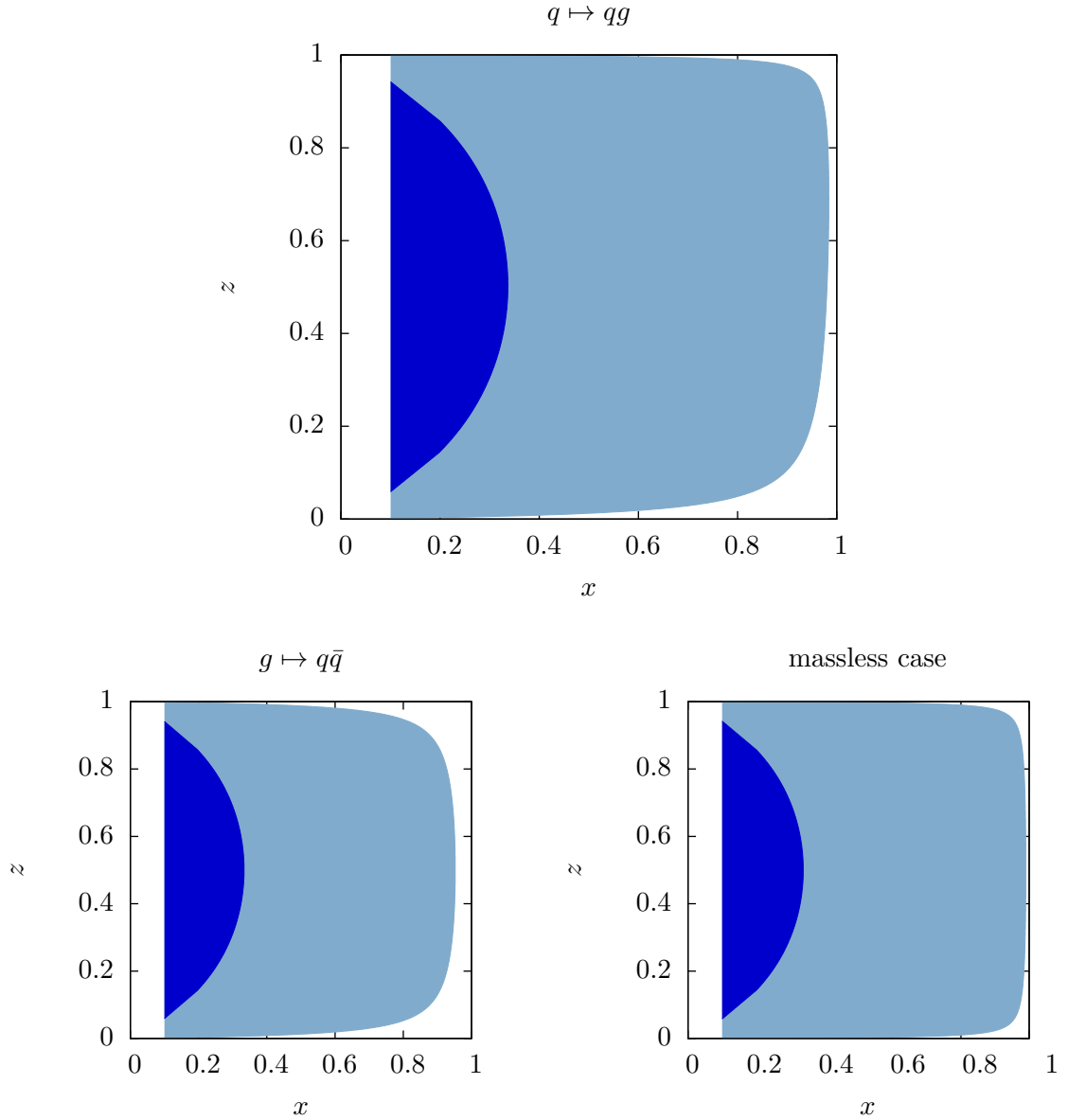


Figure 5.3.: Allowed phase-space region for emission off a final-initial dipole for invariant momentum transfer $\sqrt{s} = 100$ GeV, infrared cutoff $\mu = 5$ GeV and $x_a = 0.1$ for all different types of splittings. The quark mass is set to $m_q = 10$ GeV in each plot. The infrared cutoff and parton masses are exaggerated for illustration purposes. The light-shaded region is the accessible phase space for the evolution starting at the hard scale. The dark-shaded region is excluded when starting at a lower scale $p_{\perp}^{\text{hard}} = 70$ GeV.

such that, combined with the phase-space factorization, Eq. (5.31), the splitting probability reads

$$d\mathcal{P}(p_{\perp}^2, z) = \frac{\alpha_S}{2\pi} \langle V(p_{\perp}^2, z) \rangle \frac{f_a(x_a/x) dp_{\perp}^2}{f_a(x_a) p_{\perp}^2} dz. \quad (5.37)$$

The finite recoil only enters in the PDF ratio, reproducing the correct quasi-collinear limit when $x \mapsto 1$. Again, all quantities reproduce their respective counterparts in Ref. [13] for vanishing parton masses.

5.3. Initial-State Radiation and Final-State Spectator

Since within the formalism all initial-state partons are treated as massless, the only configuration not covered above nor in Ref. [13] is given by initial-state radiation with a final-state spectator. Note that the shower evolution is given by a backward evolution $(p_a, p_j) \mapsto (q_a, q, q_j)$, where the physical (forward) splitting process is $q_a \mapsto (p_a, q)$. For consistency, the emission q is also treated as massless although belonging to the final state.

5.3.1. Kinematics I

A Sudakov decomposition where the momentum transfer remains invariant,

$$Q \equiv q + q_j - q_a = p_j - p_a, \quad (5.38)$$

is given by

$$Rq_a = \frac{1}{x} p_a, \quad (5.39)$$

$$Rq = up_j + \frac{-k_{\perp}^2 - u^2 m_j^2}{u\bar{s}} p_a - k_{\perp}, \quad (5.40)$$

$$Rq_j = (1-u)p_j + \frac{-k_{\perp}^2 + m_j^2 - (1-u)^2 m_j^2}{(1-u)\bar{s}} p_a + k_{\perp}, \quad (5.41)$$

where $\bar{s} = 2p_a \cdot p_j$, $m_j^2 = p_j^2 = q_j^2$ and R denotes a Lorentz transformation. Again, the transverse momentum obeys $k_{\perp} \cdot p_a = k_{\perp} \cdot p_j = 0$ and is defined to be purely space-like in the dipole's rest frame (before emission). Note that for $R=1$, the direction of the emitter remains unchanged, whereas within the dipole shower formalism, preserving the direction of the spectator is preferred⁴. The kinematic variables introduced in Ref. [18] are defined as follows,

$$x = \frac{q \cdot q_a + q_j \cdot q_a - q \cdot q_j}{q \cdot q_a + q_j \cdot q_a}, \quad u = \frac{q \cdot q_a}{q \cdot q_a + q_j \cdot q_a}. \quad (5.42)$$

The transverse momentum obeys

$$-k_{\perp}^2 = u(1-u) \frac{1-x}{x} \bar{s} - u^2 m_j^2. \quad (5.43)$$

⁴In this type of splitting kinematics, the direction of the initial-state emitter is allowed to obtain transverse momentum for any spectator. After the shower evolution has terminated, a realignment boost is applied to the complete system. In this way, any emission off an initial-state parton can contribute transverse momentum to the final-state system, which is not the case for the kinematics considered in Eqs. (5.39)-(5.41) for $R=1$.

5.3.2. Kinematics II

We now present a different parametrization of the three daughter momenta with all the desired properties (in particular that the spectator does not obtain transverse momentum through the recoil). This has not yet been considered in the literature. Since a ‘‘centre-of-mass’’ frame of the momentum transfer Q does in general not exist, it is not clear if a component-wise calculation (as in Chapter 5.1.1) would give any simplification. We therefore present a (yet somewhat unwieldy) Sudakov decomposition,

$$q_a = ap_j + a'p_a + \tilde{k}_\perp, \quad (5.44)$$

$$q = bp_j + b'p_a + \tilde{k}_\perp, \quad (5.45)$$

$$q_j = cp_j + c'p_a. \quad (5.46)$$

The respective coefficients are obtained using Eq. (5.42), mass-shell conditions and momentum transfer conservation. Explicitly, they are given by

$$a = \frac{-\bar{s} + \left(\bar{s}(x+u-2xz) + 2m_j^2xu \right) / \sqrt{(x-u)^2 + 4xum_j^2/\bar{s}}}{2x(\bar{s} - m_j^2)}, \quad (5.47)$$

$$a' = \frac{\bar{s} + \alpha \left(\bar{s}(x+u-2xu) + 2m_j^2xu \right) / \sqrt{(x-u)^2 + 4xum_j^2/\bar{s}}}{2x(\bar{s} - m_j^2)}, \quad (5.48)$$

$$b = \frac{-\bar{s}(1-x-u) + \left| \bar{s}(u(1-u) - x(1-x)) + 2m_j^2xu \right| / \sqrt{(x-u)^2 + 4xum_j^2/\bar{s}}}{2x(\bar{s} - m_j^2)}, \quad (5.49)$$

$$b' = \frac{\bar{s}(1-x-u) + \alpha \left| \bar{s}(u(1-u) - x(1-x)) + 2m_j^2xu \right| / \sqrt{(x-u)^2 + 4xum_j^2/\bar{s}}}{2x(\bar{s} - m_j^2)}, \quad (5.50)$$

$$c = \frac{\bar{s}(x-u) - 2xm_j^2 + \sqrt{\bar{s}^2(x-u)^2 + 4\bar{s}m_j^2xu}}{2x(\bar{s} - m_j^2)}, \quad (5.51)$$

$$c' = \frac{-\bar{s}(x-u) + 2xm_j^2 + \alpha \sqrt{\bar{s}^2(x-u)^2 + 4\bar{s}m_j^2xu}}{2x(\bar{s} - m_j^2)}, \quad (5.52)$$

where $\alpha = 1 - 2m_j^2/\bar{s}$. The transverse momentum is given by

$$k_\perp = \sqrt{(x-u)^2 + 4xum_j^2/\bar{s}} \tilde{k}_\perp. \quad (5.53)$$

One can easily verify that this parametrization preserves the momentum transfer Q .

Considering the collinear limit $u \mapsto 0$, the emitter momentum reads

$$q_a = \mathcal{O}(u)p_j + \frac{1}{x^2} (x + u(1-x)\alpha + \mathcal{O}(u^2)) p_a + \frac{1}{x} \mathcal{O}(1)k_\perp. \quad (5.54)$$

We are therefore led to choose the physical splitting variables to be given by

$$z = x + u(1-x)\alpha \quad , \quad \kappa \equiv \frac{p_\perp^2}{\bar{s}} = u(1-u)(1-x), \quad (5.55)$$

where in the definition of the transverse momentum the mass term, which is of $\mathcal{O}(u^2)$, was dropped from Eq. (5.43) in order to simplify the expressions, i.e. $p_\perp^2 \neq -k_\perp^2$. Similar to the considerations for final-final splittings, evolution ordering is performed not strictly in the physical transverse momentum but in a quantity p_\perp which coincides with the former in all

relevant phase-space regions. Conversely, the inverse mapping is considerably simplified and reads

$$x = \frac{\alpha^2 \kappa + 2z - \alpha(1+z) + \alpha \sqrt{(1-z + \alpha\kappa)^2 - 4\kappa(1-z)}}{2(1-\alpha)}, \quad (5.56)$$

$$u = \frac{1-z + \alpha\kappa - \sqrt{(1-z + \alpha\kappa)^2 - 4\kappa(1-z)}}{2(1-z)}. \quad (5.57)$$

5.3.3. Phase Space and Splitting Probability

The kinematic parametrization gives rise to the phase-space factorization

$$\begin{aligned} d\phi(q, q_j, q_a|Q) &= d\phi(p_j, p_a|Q, x) \frac{d\phi}{2\pi} \frac{1}{16\pi^2} \frac{\bar{s}}{x} dx du \\ &= d\phi(p_j, p_a|Q, x) \frac{d\phi}{2\pi} \frac{1}{16\pi^2} \frac{\bar{s}}{x} \left| \det \frac{\partial(z, \kappa)}{\partial(x, u)} \right|^{-1} dz d\kappa, \end{aligned} \quad (5.58)$$

with the Jacobian determinant given by

$$\left| \det \frac{\partial(z, \kappa)}{\partial(x, u)} \right| = (1-x)(1-2u+u^2\alpha). \quad (5.59)$$

Averaging over azimuth, the initial-final splitting kernels read

$$\frac{8\pi\alpha_S}{2q_a \cdot q} \frac{1}{x} \langle V(p_\perp^2, z) \rangle, \quad 2q_a \cdot q = \frac{u}{x} \bar{s}, \quad (5.60)$$

such that the splitting probability directly follows,

$$d\mathcal{P}(p_\perp^2, z) = \frac{\alpha_S}{2\pi} \langle V(p_\perp^2, z) \rangle \frac{f_a(x_a/x)}{f_a(x_a)} \theta(x-x_a) \frac{1}{ux\bar{s}} \left| \det \frac{\partial(z, \kappa)}{\partial(x, u)} \right|^{-1} dz dp_\perp^2, \quad (5.61)$$

with the respective quantities given in Eqs. (5.56), (5.57) and (5.59). Since the momentum fraction of the incoming parton is rescaled during the splitting, the ratio between the respective parton distribution functions enters, with x_a the momentum fraction before splitting. The phase-space boundaries are given by the requirement $x_a < x$, which can be solved for z , such that

$$\mu^2 < p_\perp^2 < \frac{(1-x_a)\bar{s}}{4} \equiv (p_\perp^{\max})^2, \quad (5.62)$$

$$z_\pm = \frac{1}{2} \left(\alpha + x_a - (\alpha-1)x_a + \alpha(1-x_a) \sqrt{1 - \frac{p_\perp^2}{(p_\perp^{\max})^2}} \right). \quad (5.63)$$

Due to the finite mass of the spectator parton, an additional constraint arises, given by

$$0 \leq u \leq \frac{1-x}{1-x+xm_j^2/\bar{s}}. \quad (5.64)$$

See Fig. 5.4 for a visualization.

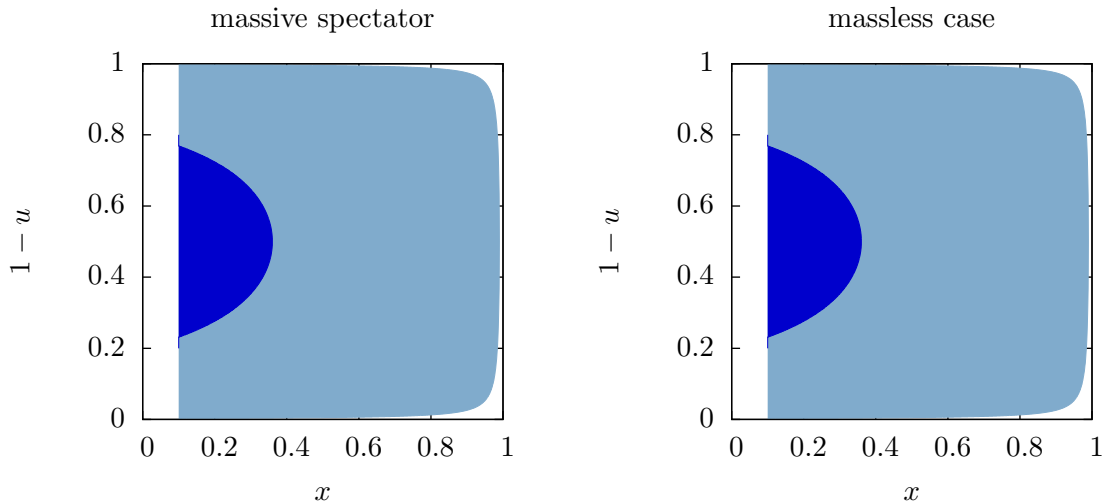


Figure 5.4.: Available phase-space region for emission off an initial-final dipole at invariant momentum transfer $\sqrt{s} = 100$ GeV, infrared cutoff $\mu = 5$ GeV and $x_a = 0.1$ for a massive spectator ($m_j = 10$ GeV) and a massless spectator, respectively. The light-shaded region is accessible for the evolution starting at the hard scale. The dark-shaded region is excluded when starting at a lower scale $p_{\perp}^{\text{hard}} = 30$ GeV. The impact of a finite spectator mass can hardly be seen with the naked eye.

5.4. Initial-State Radiation and Initial-State Spectator

Since all initial-state partons are treated as massless, this configuration does not call for any alterations due to finite parton masses. The reader is referred to Ref. [13], where all properties needed for an implementation are discussed in detail.

The Herwig++ Matchbox and DipoleShower Add-On Modules and Our Implementation

In this chapter we outline the basic work flow of the Herwig++ Matchbox add-on module, an extension to the Herwig++ event generator. We put emphasis on those elements which call for modifications in the presence of finite parton masses. For a more detailed description the reader is referred to Refs. [24, 23]. Sections 6.1-6.3 sketch the main features of the add-on module; Section 6.4 summarizes the new components implemented in the course of this work.

6.1. The `example` Library

In any Monte Carlo event generator, predictions are gained via the generation of randomly distributed single events, to which then certain weights are assigned. Since all events are sampled from random numbers, the specific sampling algorithm plays a crucial role for the efficiency of the whole algorithm. Owing to the complexity of the simulation process (in particular dipole shower and matching algorithms), a new sampler has been introduced within the Matchbox module, called `example` (for exponential sampler) [38]. Its main features include the capability of self-adapting and automated sampling for Sudakov-type probability densities only known through a function call. This type of density appears e.g. in the generation of splittings in the parton shower (see Chapter 3.3).

The resulting `example` library is based on very general grounds and implemented in a generic way where the density object only needs to provide some certain methods. Within the Matchbox module, it is used to sample events from differential cross sections and the above-mentioned Sudakov-type densities. Since finite parton masses do not call for conceptual modifications at all, we do not go into any detail here.

6.2. The DipoleShower Module

We present the parton shower outlined in Section 3.4 and Chapter 5 as implemented in the Herwig++ Matchbox module. We recall the basic properties of the general algorithm in the order of the work flow, starting from initial conditions and finishing with a final state which is then further treated by the hadronization model.

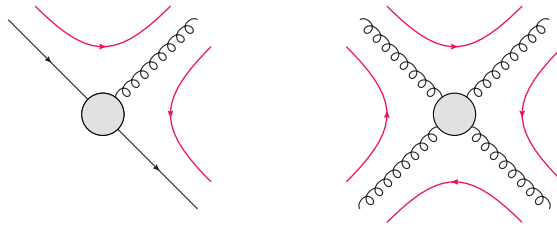


Figure 6.1.: Examples of dipole chains. Each pair of subsequent partons is colour-connected, as indicated by the red lines, and forms a dipole. As gluons exhibit two colour partners, chains of connected dipoles are formed. The left figure shows a non-circular and the right figure a circular chain.

6.2.1. Initialization

The initial conditions for the parton shower are determined by the colour flow in the hard process [39]. To each (anti-)quark a colour or anti-colour is assigned depending on its membership to either the initial or final state. Accordingly, a gluon carries both colour and anti-colour yet does not form an independent colour-anti-colour pair (due to the underlying $SU(3)$ gauge group). The algorithm is set up in the large- N limit (N being the number of different colours) such that each (anti-)colour is unique.

In the parton shower considered, colour singlets evolve independently, hence all partons from the hard sub-process are first sorted into colour singlets. This is done by exploiting the fact that a colour singlet is simply connected in the sense of its colour flow topology: each parton can be reached from any other parton by walking along (anti-)colour lines. We do not consider colour reconnection models (see e.g. Ref. [40]), therefore these colour singlets can indeed be regarded as independently evolving entities.

In the last step before the actual evolution, the partons in each singlet are sorted in such a way that colour-connected partons are in subsequent positions. Any such two neighbours form a dipole which may radiate during shower evolution. An (ordered) set of dipoles is called dipole chain, see Fig. 6.1 for examples. When a quark and an anti-quark are involved, the dipole chain is called open or non-circular since they mark the end points of the chain. On the other hand, a chain is called circular if it only consists of gluons and hence each parton has two colour partners.

In the algorithm, a dipole is represented in one-to-one correspondence by a `Dipole` class object. An (ordered) set of `Dipole` objects is assembled in a `DipoleChain` object. The hard scales are reported by the `DipoleEvolutionOrdering` object, given additional parameters such as the type of the splitting through a reference to a `DipoleSplittingKernel` object.

6.2.2. Evolution

In each dipole chain, all possible splittings are considered to compete with all other possible splittings of the chain. For a specific dipole (i, j) this involves all splittings $(i, j) \mapsto (i', k, j)$ as well as all splittings from the second leg where i, j are interchanged. The splitting with the largest value of (squared) transverse momentum p_{\perp}^2 is selected as long as it is above the shower's infrared cutoff, $p_{\perp}^2 > \mu_{(f),\text{IR}}^2$. We include the possibility of different shower cutoffs for the different involved flavours f , see Chapter 8. If no allowed splitting could be selected, the chain stops evolving and is inserted into the event record. For any candidate splitting (given an associated hard scale $(p_{\perp}^{\text{hard}})^2$) a scale p_{\perp}^2 is selected with probability

given by the Sudakov form factor

$$\Delta_{(i,j)\rightarrow(i',k,j)}(p_{\perp}^2, (p_{\perp}^{\text{hard}})^2) = \exp\left(-\int_{p_{\perp}^2}^{(p_{\perp}^{\text{hard}})^2} dq^2 \int_{z_-(q^2)}^{z_+(q^2)} dz P_{(i,j)\rightarrow(i',k,j)}(q^2, z)\right), \quad (6.1)$$

where $P_{(i,j)\rightarrow(i',k,j)}(q^2, z)$ is the appropriate splitting probability defined in Chapter 5.

The base class for kinematic parametrizations and phase space weight is called `DipoleSplittingKinematics`. Separate objects are implemented for final-final, final-initial, initial-final, and initial-initial splittings. The azimuthally averaged splitting kernels are stored in `DipoleSplittingKernel` objects for all possible configurations respectively. Each `DipoleSplittingKernel` can flag a certain splitting type to be equivalent to another splitting type for performance issues¹. `DipoleSplittingGenerator` objects assemble `DipoleSplittingKernel`, `DipoleSplittingKinematics` and `ThePEG:AlphaS` objects to completely define the splitting probability. The scale p_{\perp}^2 is then sampled according to Eq. (6.1) using the `exsample` library and a splitting is selected for the `DipoleChain` object considered.

In the case of a $(g, x) \mapsto (q, \bar{q}, x)$ splitting being selected, a circular chain becomes non-circular and an already non-circular chain is split up into two non-circular chains which then evolve independently. See Fig. 6.2 for an illustration.

The complete showering cascade is managed by the `DipoleShowerHandler` class.

6.2.3. Finalization of the Shower

If for each dipole chain no allowed splitting can be selected, the shower evolution stops. Due to initial-state radiation, the incoming parton momenta in general have obtained non-vanishing transverse momenta with respect to the beam axis during parton shower evolution. Therefore, the complete event is realigned after the shower has terminated.

6.3. The Matchbox Module

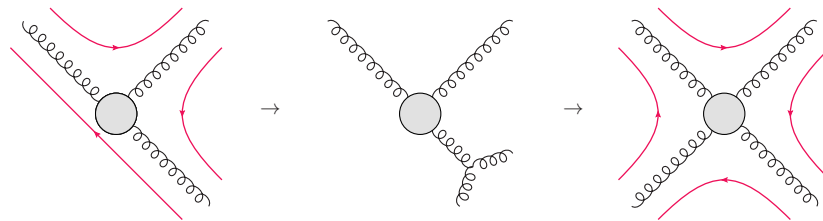
The `Matchbox` module performs the calculation of matched matrix elements at NLO using the Catani-Seymour dipole subtraction formalism and the matching procedure outlined in Chapter 3 in an automated way. The generation of the subtraction terms is outlined in Subsection 6.3.1. In Subsection 6.3.2 we sketch the generation of matched matrix elements.

6.3.1. Automatic Generation of Subtraction Terms

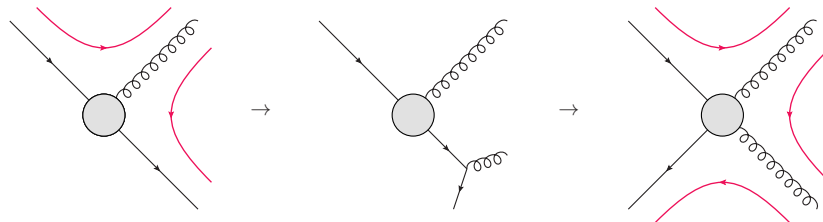
Recall from Section 3.2 that in order to perform an NLO calculation in the Catani-Seymour subtraction scheme the following expressions are required [18]:

- process-dependent quantities
 - a set of independent colour projections of the matrix element squared at the Born level, summed over parton polarizations (in d dimensions)
 - an additional projection of the Born-level matrix element over the helicity of each external gluon (in four dimensions)
 - the one-loop contribution $d\sigma^V$ (in d dimensions)
 - the real emission contribution $d\sigma^R$ (in four dimensions)

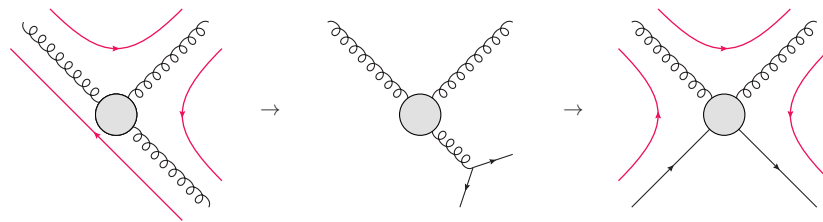
¹E.g. $\{(q, \bar{q}) \mapsto (q, g, \bar{q})\} \sim \{(\bar{q}, q) \mapsto (\bar{q}, g, q)\}$ or, for up quarks treated in the massless approximation, $\{(x_1, u) \mapsto (x_2, x_3, u)\} \sim \{(x_1, g) \mapsto (x_2, x_3, g)\}$.



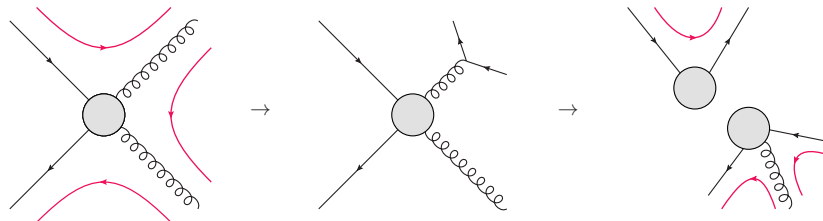
For gluon emission off a circular chain, the chain stays circular.



For gluon emission off an open chain, the chain stays open.



For quark pair production, a circular chain becomes open.



For quark pair production, an open chain breaks up.

Figure 6.2.: Examples for parton splittings in dipole chains. In each chain, all possible emissions off all dipoles compete for splitting. Recall that additionally in each dipole, emission from both legs is possible. When a chain breaks up, both resulting chains evolve independently.

- process-independent quantities
 - the subtraction dipoles $\mathcal{D}_{ij,k}$
 - the insertion operators \mathbf{I} , \mathbf{P} and \mathbf{K}
 - a kinematic $3 \mapsto 2$ mapping in order to merge two external legs

The colour and helicity projections of the Born matrix element squared are essential in order to apply the insertion operators which exhibit said correlations. Note that only the finite part of the respective expressions is needed for numerical evaluations, since the process-independent factors have been explicitly tailored to analytically remove all singularities. The correct set of subtraction dipoles and Born matrix elements for the process under consideration is obtained by investigating all possible mergings of external partons that appear in the real emission contribution. After these preparations, all respective

contributions to the NLO calculation can be performed numerically.

In the remainder of this section, we merely mention the classes implemented in the `Matchbox` module which are in one-to-one correspondence to the expressions outlined above. This is done for the sake of completeness and in order to enable the interested reader to track the modifications done in the course of this work.

By default, matrix elements are implemented in the following way: `MatchboxMEBase` is the base class for tree-level matrix elements and virtual corrections². The squared amplitudes $|\mathcal{M}|^2$, colour and potentially spin and colour correlated amplitudes $\langle \mathcal{M} | \mathbf{T}_i \cdot \mathbf{T}_j | \mathcal{M} \rangle$, $\langle \mathcal{M}_\mu | C^{\mu\nu} \mathbf{T}_i \cdot \mathbf{T}_j | \mathcal{M}_\nu \rangle$, one-loop/Born interference and a phase space generator for the implemented process are represented here.

The `SubtractionDipole` class is the base class for subtraction dipoles $\mathcal{D}_{ij,k}$, whilst the insertion operators `I`, `P`, `K` are implemented as `MatchboxInsertionOperator` objects. Dipoles and insertion operators may be registered with the `DipoleRepository` from which they can be accessed during calculations. The Born process and virtual corrections are calculated by making use of the `MatchboxNLOME` class. In order to assemble the subtracted real emission matrix element from the concerning `MatchboxMEBase` object and several `SubtractionDipole` objects, all possible mergings of external partons are investigated to obtain the correct set of subtraction dipoles and Born matrix elements. The respective $3 \mapsto 2$ kinematic mappings, $p_{i,j} \equiv p_{i,j}(q_i, q, q_j)$, are implemented in `TildeKinematics` objects³. The `SubtractedME` class then calculates the subtracted real emission matrix element within the Catani-Seymour subtraction formalism.

Finally, the matrix elements are handed over to the `NLOFactory` and are used to calculate the matched matrix elements. We sketch this process in the following subsection.

6.3.2. Matching with Matrix Element Corrections

POWHEG-type matching [26] can be automatically performed by the `PowhegFactory` class. Various ratios of squared matrix elements or subtraction dipoles divided by a sum of subtraction dipoles are calculated. They are used to obtain re-weighted matrix elements. The `InvertedTildeKinematics` class is the base class for the $2 \mapsto 3$ kinematic mapping, $\{q_i, q, q_j\} \equiv \{q_i, q, q_j\}(p_i, p_j; p_\perp^2, z, \phi)$, similar to the `DipoleSplittingKinematics` class used for parton shower evolution. All pieces are assembled automatically by the `PowhegFactory` class. A specialized post sub-process handler generates real emission radiation according to the matrix-element-corrected Sudakov form factor and may eventually replace a Born-type with a real-emission-type sub-process.

6.4. Our Implementation

During the course of this work, we implemented several modifications in order to incorporate the effects of finite parton masses. Due to the very flexible layout of the underlying algorithm, this included mostly a definition of “massive” sister classes to already existing “light” classes. Concerning splittings, more information about the splitting products is necessary compared to the massless approximation. The new dipoles and splitting kernels have been carefully defined in order to not interfere with processes involving only massless partons. Specifically, detailed log files of the shower evolution have been examined. No

²Note that the real emission matrix element is itself the tree level of a process involving one additional parton in the final state.

³The name refers to the notation used in the original papers on the subtraction formalism where the momenta p_i, p_j, p_k are mapped to $\tilde{p}_{ij}, \tilde{p}_k$. Conversely, a splitting is denoted $(\tilde{i}, \tilde{j}, k) \mapsto (i, j, k)$ accompanied by the kinematic mapping $(\tilde{p}_{ij}, \tilde{p}_k) \mapsto (p_i, p_j, p_k)$.

misbehaviour was found concerning the selection of the correct set of candidate splittings and the identification of equivalent parton configurations.

Due to additional phase-space constraints which arise from finite parton masses, the generation of parton branching was equipped with a veto mechanism concerning the kinematic variables.

All new methods have been separately checked to reproduce the results obtained by the “light” methods when the parton masses are set to zero. Particularly in the case of insertion operators, numerical instabilities can occur when the parton masses approach zero⁴. In-situ checks have explicitly shown the numerical stability of our implementation in this limit.

A systematic verification of the interplay between splitting kernels and kinematics as well as an investigation of the subtraction algorithm is presented in Chapter 7.

With all these modifications, the user is now able of switching between a massless approximation and an implementation taking full account of finite parton masses at input file level. See Appendix A where our implementation is described from a user point of view. Additionally, a complete list of the classes implemented in the course of this work is given.

So far, we only implemented and investigated a modified parton shower for final-state radiation with a final-state spectator. This has been done for the sake of a complete verification and parameter tuning to the LEP experiment. However, the modifications necessary for an improved simulation of events involving initial state partons as well have been outlined above. An implementation will be subject to future studies.

⁴E.g. due to factors of the form $\ln(\rho) \ln(1 + \rho)$ or $\rho \ln \rho$ with $\rho \mapsto 0$ for $m \mapsto 0$.

This chapter gives an overview of the validation of the simulation code. Extensive checks have been performed for the massless implementation and are documented in Ref. [24], hence we do not focus on a general validation but on the extensions implemented during the course of this work in order to incorporate finite parton masses. Most classes in the `DipoleShower` and `Matchbox` modules provide the possibility of printing out detailed diagnostic information during the simulation. These log files have been investigated and no misbehaviour could be found. Additional information has been printed out and examined to explicitly monitor potential numerical instabilities concerning the massless limit and the kinematic setup. Again, no malfunction could be recognized.

In the following we discuss validations of the new shower implementation as well as the subtraction scheme. After those validations at parton level, consistency with the massless approximation implementation is examined at observable level.

7.1. Shower Radiation

A cross check of the correct implementation of the splitting kernels and kinematics is to consider the spectra of the two kinematic quantities p_{\perp} and z for emissions generated by the shower, validated against a numerical integration of the expected Sudakov-type distribution. The latter has been implemented in a completely independent code, following the arguments presented in Chapter 5. Full agreement was found for final-final splittings off a $q\bar{q}$ dipole, where we investigated the situation for light and heavy quarks, respectively. See Fig. 7.1 for radiation off a $b\bar{b}$ dipole and Fig. 7.2 for other scenarios involving light and charm quarks. As can be seen, our implementation allows for an improved parton shower simulation at parton level when heavy quarks are involved.

Since the structures handling and sampling the splitting probabilities are implemented in a completely generic way, all other types of final-final splittings are expected to show the same degree of agreement. Gluon emission off a $q\bar{q}$ dipole was chosen as a representative to demonstrate the validity of the shower implementation because it is also the first emission in LEP-like simulations.

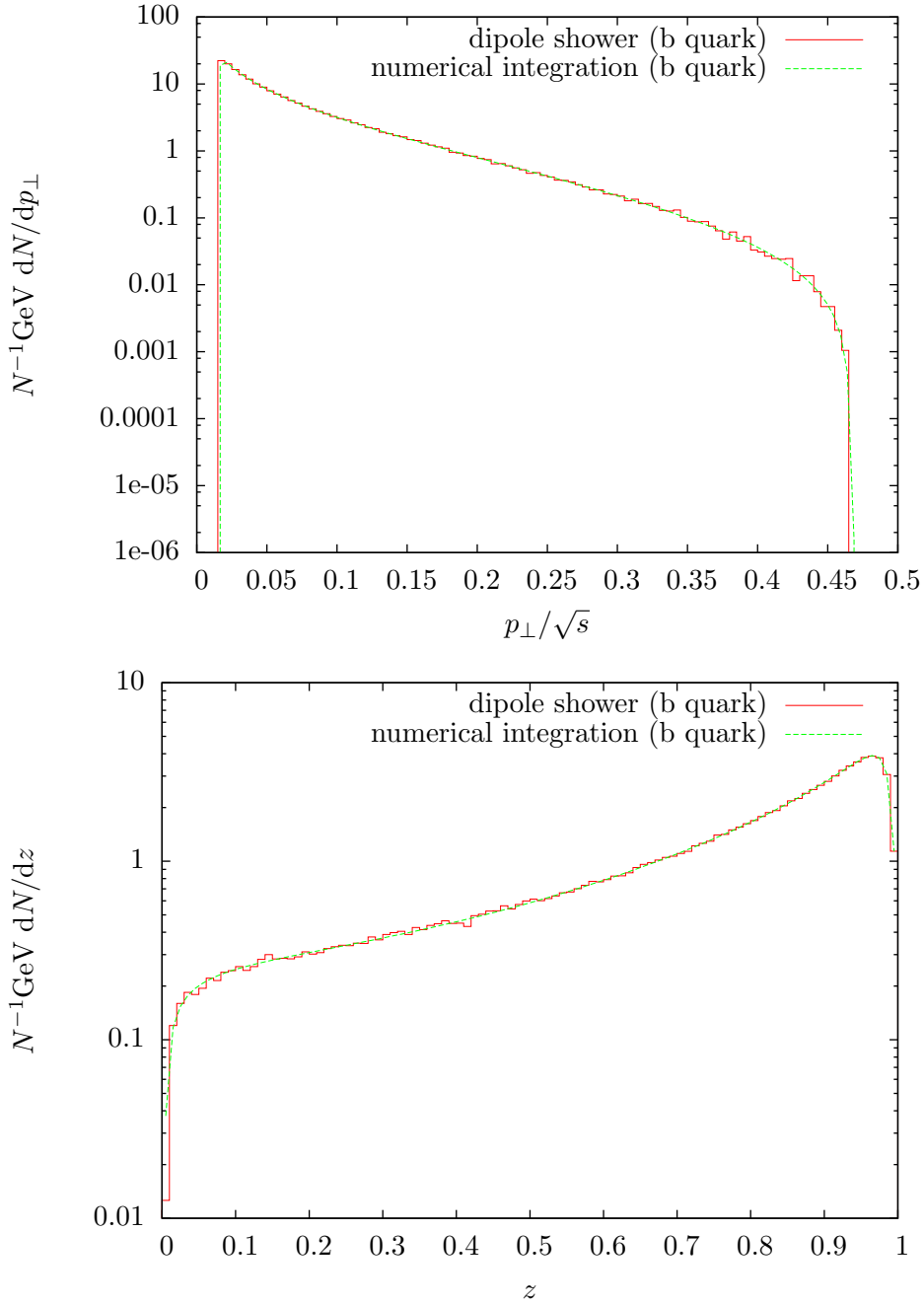


Figure 7.1.: p_{\perp} and z spectra as generated from a final state $b\bar{b}$ dipole in LEP events ($\sqrt{s} = 91.2$ GeV) versus results from a numerical integration. In the upper plot, effects stemming from the infrared cutoff as well as a reduced maximum transverse momentum $p_{\perp}^{\text{max}} < \sqrt{s}/2$ as a result of the large b quark mass can be observed.

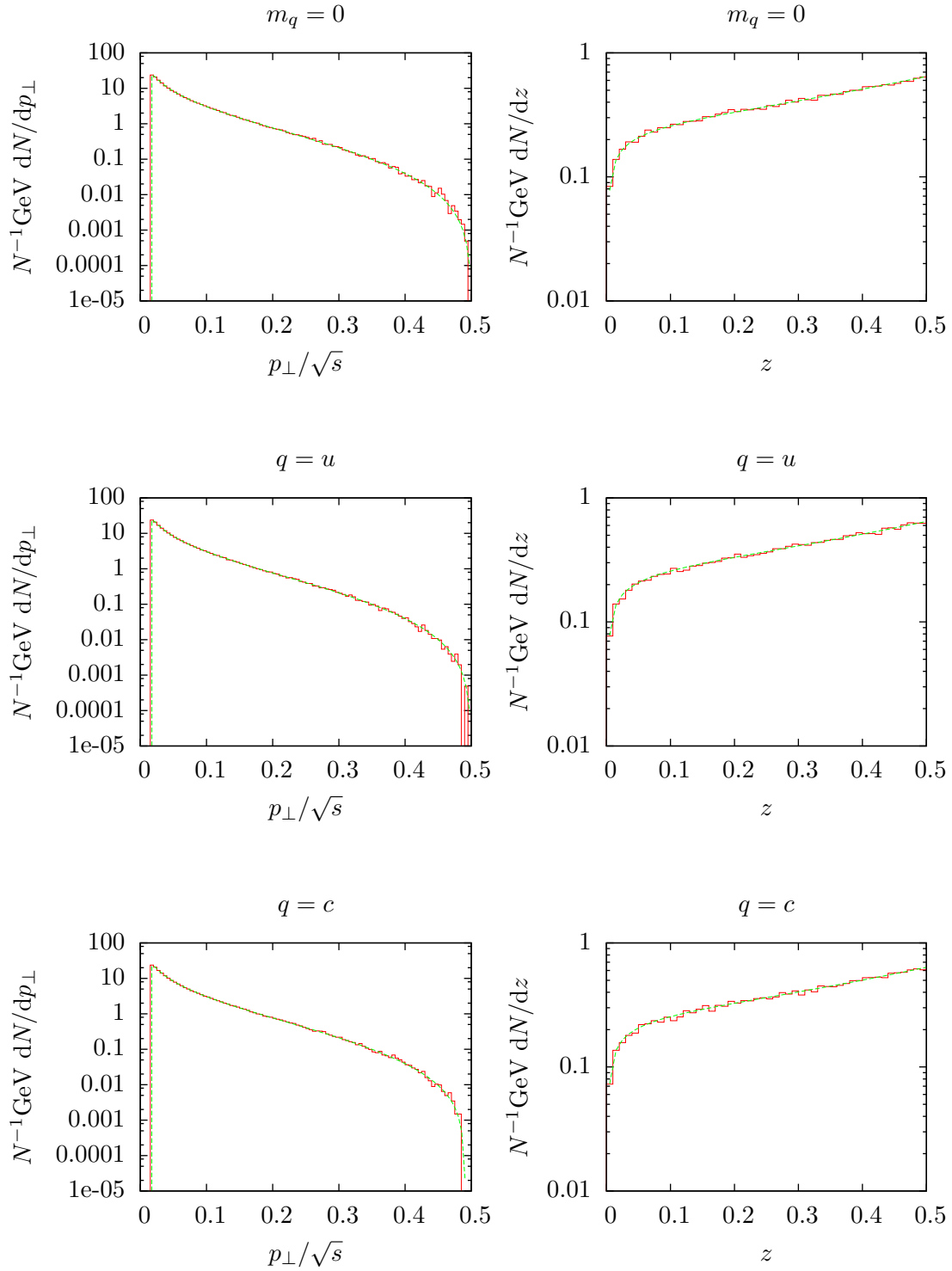


Figure 7.2.: p_{\perp} and z spectra as generated from a final state $q\bar{q}$ dipole in LEP events ($\sqrt{s} = 91.2$ GeV) for different quark flavours (red lines) versus results from a numerical integration (green broken lines). Perfect agreement was found for arbitrary quark masses.

7.2. Matrix Element Subtraction

The functionality of the subtraction terms has been validated. These terms particularly include the dipoles and insertion operators which were implemented during this work. Fig. 7.3 shows typical examples of the ratio of subtraction to real emission cross section, plotted against the respective propagator invariant causing the singularities if the quasi-collinear limit is reached. The ratio tends to 1 as the quasi-collinear region is approached for light quarks (demonstrated for up quarks). Although finite quark masses both screen the singularities in the matrix element and prevent from actually reaching the quasi-collinear limit, the ratio tends close to 1 for charm and bottom quarks as well. Since the soft singularity is still present for finite parton masses, the plots showing the same ratio against the energy of the emitted gluon are much more relevant for the desired verification. Here, the ratio reaches unity for arbitrary parton masses, thus proving the consistency of our implementation within the subtraction scheme.

7.3. Observables in the Massless Limit

A good check of consistency is to force the simulation to use all newly implemented massive classes but explicitly set all masses to zero, and compare the results to the massless implementation. This validation has been carried out for a large class of observables, ranging from event shapes to identified particle spectra. See Fig. 7.4 for exemplary observables. All plots show perfect agreement, proving the correct limiting behaviour of our implementation. It is striking that the simulation results exactly coincide even in phase-space regions of low statistics, where the exact same statistical fluctuations are reproduced. This indicates that the two implementations are indeed identical in the massless limit.

7.4. Conclusions

Our implementation of a dipole shower taking full respect of finite parton masses has been validated to be fully compatible with the existing setup of the `Matchbox` add-on module. Complete agreement with the present implementation in the massless approximation was shown. The consistent implementation of splitting kernels and kinematics in the shower as well as dipoles and insertion operators for matrix element subtraction was confirmed for arbitrary parton masses.

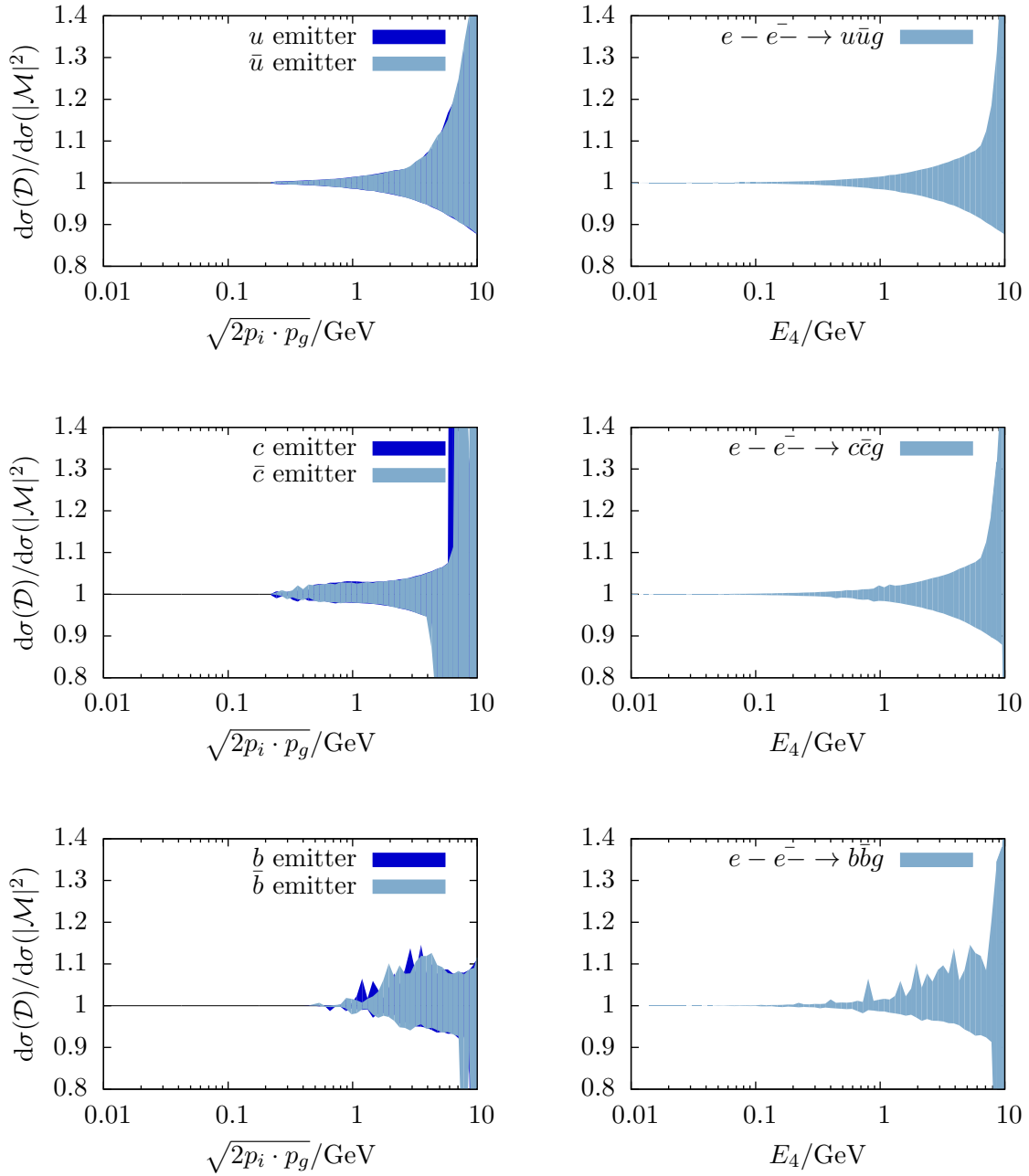


Figure 7.3.: Envelopes for the ratio of the subtraction to the real emission cross section in $e^+e^- \mapsto q\bar{q}g$ events in the case of u , c and b quarks, respectively. On the left-hand-side, the ratio is plotted against the propagator denominator for both possible emitter-spectator combinations. The figures on the right-hand-side show the same ratio versus the energy of the emitted gluon.

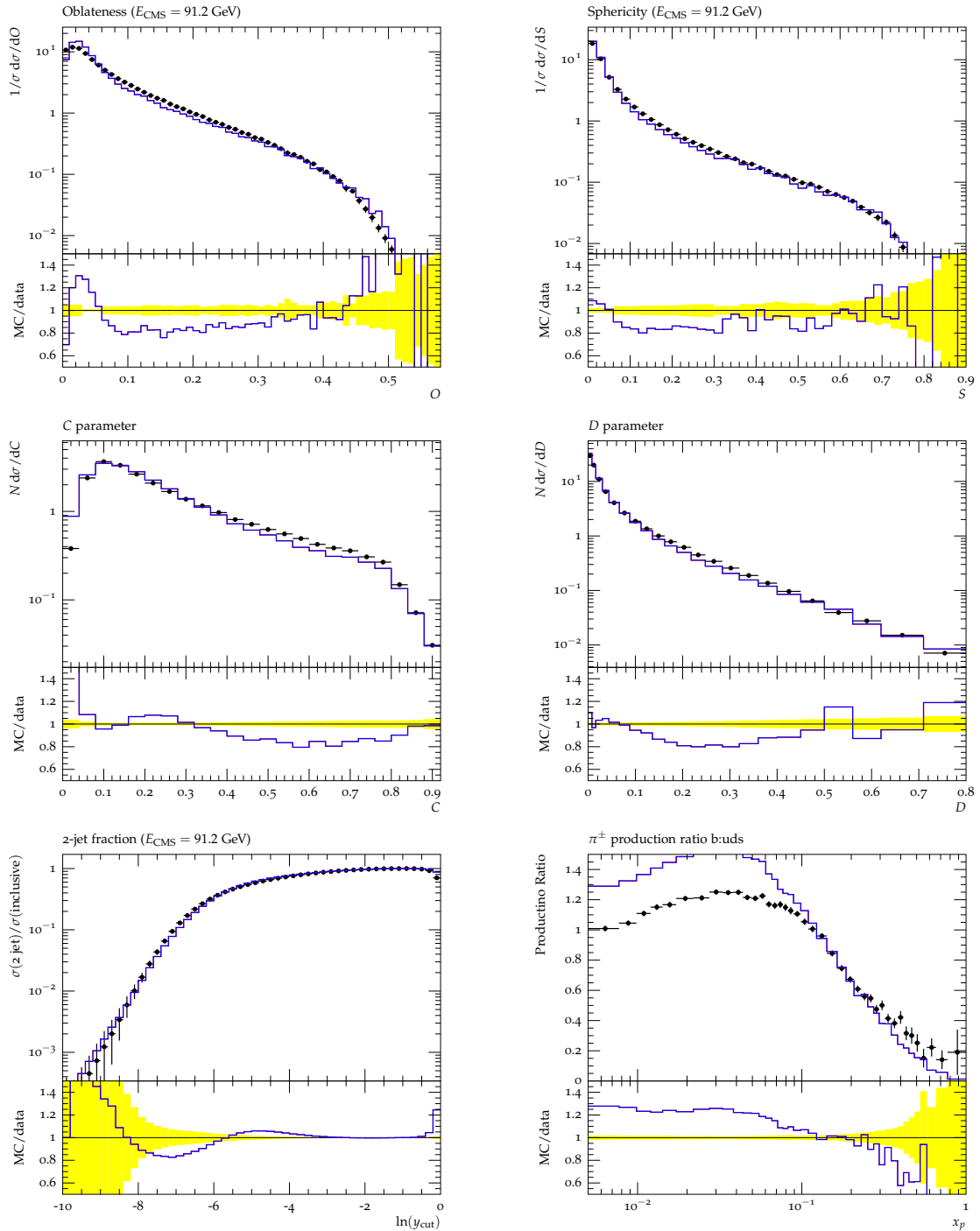


Figure 7.4.: Exemplary observables for simulations with the dipole shower in the massless approximation and our implementation where all masses are set to zero by hand. In each plot only one of the two curves is visible since the two simulation results exactly coincide, proving the correct limiting behaviour of the new shower. Experimental data was obtained by the ALEPH collaboration [41] for oblateness, sphericity and the 2-jet fraction, the DELPHI collaboration [42] for C and D parameter, and the SLD collaboration [36] for the π^\pm production ratio.

Analysis II: Simulation Results

This chapter presents further analyses concerning our implementation, which aim at a better description of a large class of observables at LEP. Special emphasis is put on the description of heavy partons.

Since the implementation of the new parton shower could be validated in the previous section, the partonic final state is expected to give a more accurate description compared to the massless approximation. Therefore, tuning has to be performed where the free parameters of the parton shower and of the non-perturbative hadronization model are re-adjusted, see Chapter 4.3. In Section 8.1 the tuning procedure is described and results are presented. Section 8.2 gives a discussion of B -hadron fragmentation which is particularly sensitive to the dynamics of heavy quarks. Conclusions are drawn in Section 8.3.

8.1. Tuning

We aim at a complete tune of both shower and hadronization model parameters to LEP data. Since in our implementation heavy quarks evolve qualitatively differently compared to light quarks, separating shower and hadronization parameters for different quark flavours is reasonable. Thus, in comparison to the massless approximation, a larger set of parameters is available and tuning is expected to further improve simulation results.

8.1.1. Setup

As quark masses only enter the shower dynamics in terms of the form m^2/Q^2 where Q^2 is a typical scale of the dipole, the effects of light quark masses are very limited. We therefore allow flavour-dependent parameters for light (u, d, s), charm and bottom quarks, respectively. A complete list of the parameters varied during the tuning stage and their respective ranges is given in Tab. 8.1.

Tuning was performed using the Professor tuning system sketched in Section 4.5. Due to the large number of free parameters, it was carried out as a multistage process where light-, charm- and bottom-quark-related parameters were treated in separate groups. At each stage, the previously obtained results were used as default input parameters. For reference data, event shape variables and jet rates as measured by the DELPHI [42, 43] and ALEPH [41] experiments, jet observables as determined by the OPAL collaboration [44],

Parameter	Range	Description
$\alpha_S(M_Z^2)$	0.1 – 0.13	strong coupling constant at the Z mass
$\mu_{\text{IR,FF}}^{(f)}$	0.5 GeV – 2.0 GeV	infrared shower cutoff for final-final dipoles
$\mu_{\text{soft,FF}}^{(f)}$	0.3 GeV – 1.2 GeV	soft scale for final-final dipoles
$m_{g,c}$	0.67 GeV – 3.0 GeV	gluon constituent mass
$\text{Cl}_{\text{max}}^{(f)}$	0.5 GeV – 10 GeV	maximum cluster mass
$\text{Cl}_{\text{pow}}^{(f)}$	0.0 – 10.0	cluster mass exponent
$\text{Cl}_{\text{smr}}^{(f)}$	0.0 – 10.0	cluster direction smearing
$\text{P}_{\text{split}}^{(f)}$	0.0 – 1.4	cluster mass splitting parameter

Table 8.1.: The parameters varied for the fit to LEP data. Parameters indicated by the superscript (f) exist in three copies, depending on the heaviest flavour associated where $f = (uds), c, b$. The hadronization parameters were introduced in Section 4.3.

and identified particle spectra as reported by the SLD collaboration [36] were used. The “light” and global parameters were tuned to event shapes, jet rates, multiplicities and those identified particle spectra with no particular reference to heavy flavours. Shower and hadronization parameters for charm and bottom quarks were tuned to the respective identified particle spectra. In a last step, the global parameters were once more fitted in order to incorporate the improved behaviour of the heavy quark simulation.

This tuning cycle was repeated several times, assigning different weighting to the observables in order to find the best possible description of experimental data. However, tunes where large weights were assigned to the B -hadron fragmentation turned out to be unstable within our setup and agreement with data could not be achieved. We therefore decided to aim at a tune satisfactory for the large majority of observables under consideration and give a separate discussion of the B -hadron fragmentation in Section 8.2.

8.1.2. Results and Discussion

The fitted parameter values are given in Tab. 8.2. Generally, no significant difference between the parameters for the LO and NLO fit is found. Moreover, the hadronization parameters for the different quark flavours are of the same order.

The standard deviation for $\alpha_S(M_Z^2)$ given by Professor is particularly small compared to the other parameters. Although a determination to this accuracy seems implausible, the results are still compatible with the world average [45] of 0.1184(7).

The values obtained for the infrared shower cutoff $\mu_{\text{IR}}^{(f)}$ of charm and bottom quarks yield an inconsistent picture. In particular, the large differences between the values obtained at LO compared to NLO are surprising. However, this peculiarity can be explained by the strong dependence of the heavy flavour cutoffs on only a limited number of observables during the tune. A smaller value for the light flavour cutoff is preferred by the NLO fit, i.e. more of the dynamics are modelled by a QCD prediction than by the phenomenological hadronization model. Conversely, the reverse effect is found for charm and bottom quark evolution.

In Fig. 8.1 LO and NLO simulation results are compared for selected observables and in general give a comparably accurate description of experimental data. For clarity, we therefore only make use of the LO simulation for further comparisons with other shower algorithms. A comparison between LO simulation results, a previous tune [23] of the dipole shower in the massless approximation and the Herwig++ standard shower is shown in

Parameter	LO	NLO
$\alpha_S(M_Z^2)$	0.11845(7)	0.11756(7)
$\mu_{\text{IR,FF}}^{(uds)}$	1.219(5) GeV	1.064(4) GeV
$\mu_{\text{IR,FF}}^{(c)}$	0.37(7) GeV	0.61(9) GeV
$\mu_{\text{IR,FF}}^{(b)}$	0.63(2) GeV	1.159(12) GeV
$\mu_{\text{soft,FF}}^{(uds)}$	0.813(4)	0.68(2)
$\mu_{\text{soft,FF}}^{(c)}$	0.81(6)	0.59(7)
$\mu_{\text{soft,FF}}^{(b)}$	0.877(18)	0.764(12)
$m_{g,c}$	1.599(7) GeV	1.533(4) GeV
$\text{Cl}_{\text{max}}^{(uds)}$	3.839(18)	2.982(12)
$\text{Cl}_{\text{max}}^{(c)}$	2.0(4)	3.8(4)
$\text{Cl}_{\text{max}}^{(b)}$	3.98(18)	3.52(8)
$\text{Cl}_{\text{pow}}^{(uds)}$	5.05(2)	5.044(16)
$\text{Cl}_{\text{pow}}^{(c)}$	2.6(5)	3.5(4)
$\text{Cl}_{\text{pow}}^{(b)}$	7.94(12)	7.70(5)
$\text{Cl}_{\text{smr}}^{(uds)}$	5.02(3)	5.39(2)
$\text{Cl}_{\text{smr}}^{(c)}$	3.6(5)	3.9(7)
$\text{Cl}_{\text{smr}}^{(b)}$	4.69(2)	2.39(11)
$\text{P}_{\text{split}}^{(uds)}$	0.801(2)	0.742(2)
$\text{P}_{\text{split}}^{(c)}$	0.45(7)	0.36(6)
$\text{P}_{\text{split}}^{(b)}$	0.004(13)	0.024(8)

Table 8.2.: Parameters for LO and NLO fits to LEP data.

Fig. 8.2. The generally good agreement of the dipole shower predictions with experimental results is further improved by our implementation, and the overall description of event shapes and jet rates by the dipole shower is closer to experimental data than the standard shower. Nevertheless, hadron multiplicities are off data in the dipole shower but largely of the same order, see Tab. 8.3.

Fig. 8.3 shows the energy-energy correlation, which has not been included in the fit and serves as a test of the predictive efficiency of the simulation. Almost perfect agreement is found for the LO and NLO fits.

Particle	Average Multiplicity	Simulation	
		LO	NLO
mean charged	21.16(21)	21.64	21.57
π^+	17.02(19)	16.29	16.32
π^0	9.42(32)	8.92	8.99
K^+	2.228(59)	3.248	3.210
K^0	2.045(26)	3.160	3.109
D^+	0.175(16)	0.298	0.314
D^0	0.454(30)	0.463	0.576
$\rho(770)^0$	1.231(98)	0.930	0.971
$\rho(770)^\pm$	2.40(43)	2.00	2.10
$\omega(782)$	1.016(65)	0.719	0.759
$\phi(1020)$	0.0963(32)	0.1693	0.1769
$J/\Psi(1S)$	0.0052(4)	0.0036	0.0041
p	1.050(32)	1.566	1.462

Table 8.3.: Average hadron multiplicities per hadronic e^+e^- annihilation events at $\sqrt{s} = 91.2$ GeV, as published by the Particle Data Group [46] compared to the LO and NLO predictions of our implementation. The experimental data for the mean charged multiplicity is taken from the OPAL collaboration [47]. Statistical fluctuations in the MC runs are negligible.

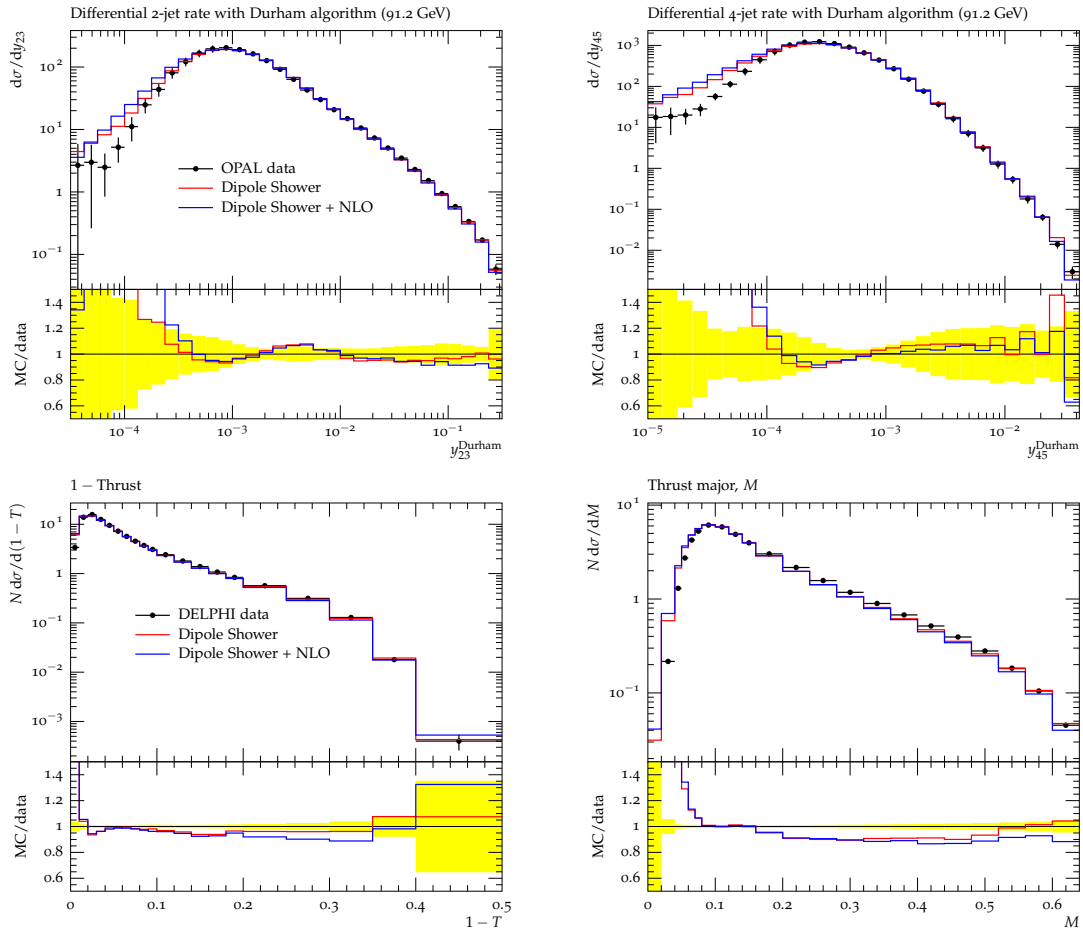


Figure 8.1.: Some differential jet rates and event shapes as predicted by the leading order and next-to-leading order simulations.

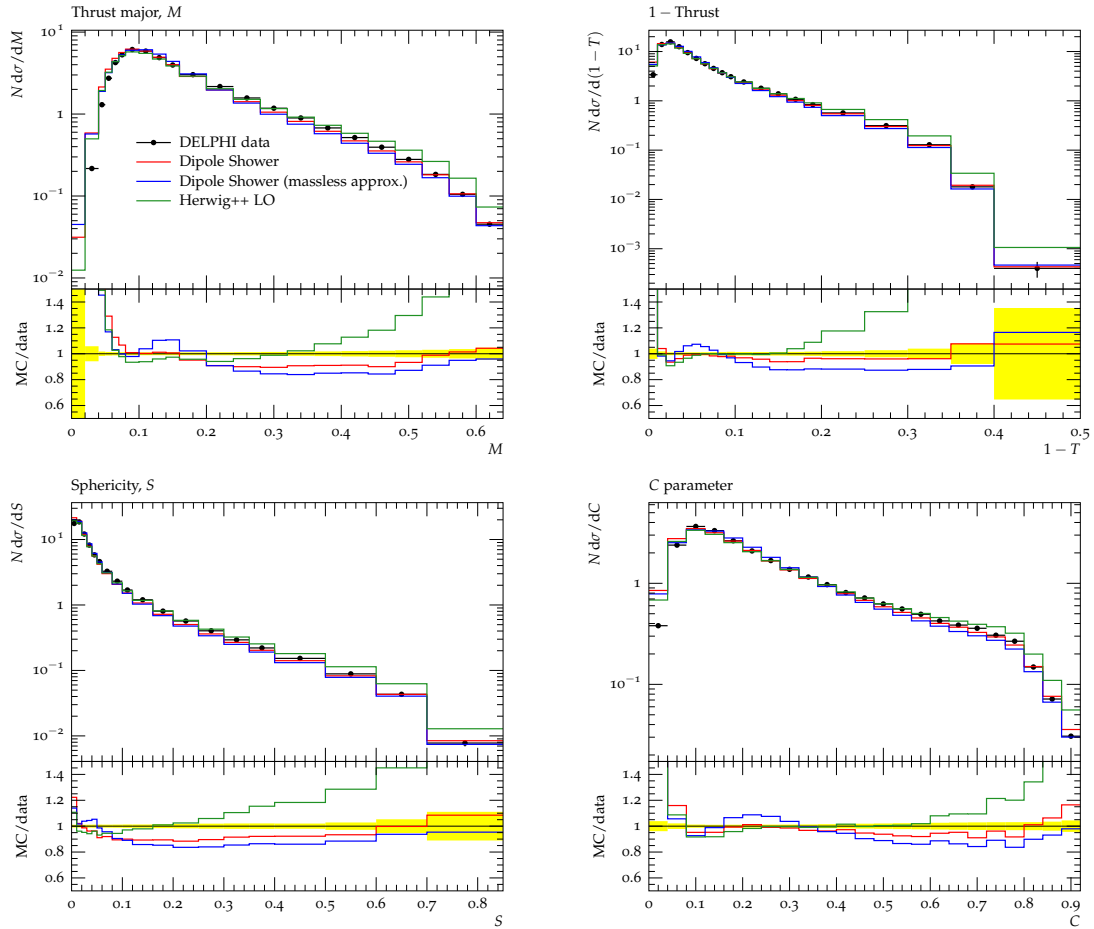


Figure 8.2.: Some event shape variables as predicted by the leading order simulations. Here, we compare to both the previous implementation of the dipole shower in the massless approximation and the standard *Herwig++* shower. The new dipole shower gives a significantly improved description.

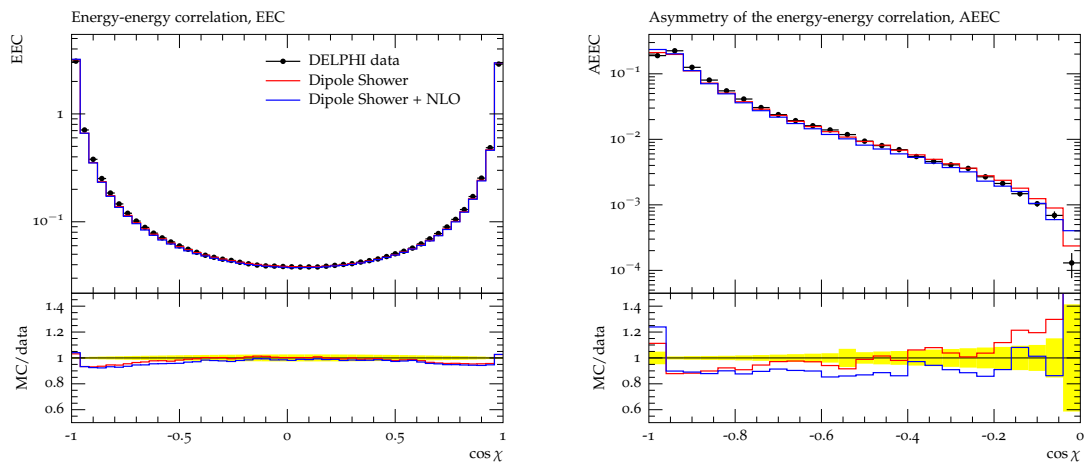


Figure 8.3.: Energy-energy correlation and asymmetry of the energy-energy correlation. These observables have not been included in the fit and thus provide a test of the predictive efficiency of the simulation.

8.2. B -Hadron Fragmentation

The B -hadron fragmentation distribution is an important tool for investigating the impact of our implementation, since it is explicitly related to heavy quarks. Fig. 8.4 shows the simulation results for various shower setups. Although the description is improved by the new parton shower in comparison to the dipole shower in the massless approximation, agreement with experimental data seems out of reach.

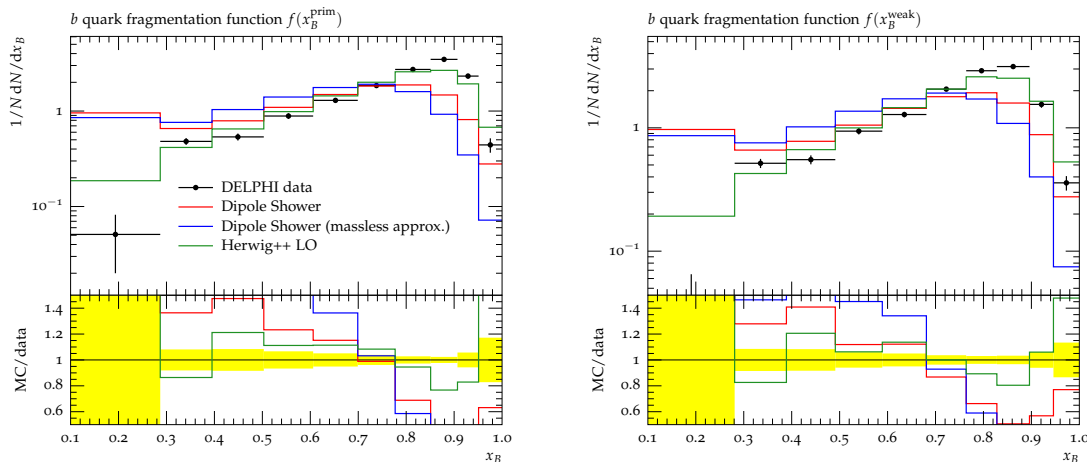


Figure 8.4.: B -hadron fragmentation for three different parton shower implementations.

Therefore, we investigated the partonic final state and the subsequent formation of primary clusters just before hadronization in more detail. Since the **Herwig++** standard shower gives a fairly accurate description of the B -hadron fragmentation, it served as a benchmark to which the dipole shower spectra were tuned manually. Fig. 8.5 shows the spectrum of the partonic state right before hadronization as well as the spectrum of primary clusters which contain a b or \bar{b} quark. In both spectra, an excess of particles carrying a very high energy fraction arose, which corresponds to shower evolution without any branching at all. Lowering the IR cutoff to $\mu_{\text{IR}}^{(b)} = 0.25$ GeV was found to yield quite good agreement in this phase-space region. Additionally, the respective soft scale $\mu_{\text{soft}}^{(b)}$ which screens the Landau singularity in the coupling constant was significantly lowered to 0.2 GeV in order to give a better description in the perturbative domain.

A second effect of our implementation is manifest in a bump in the primary cluster spectrum at $10 \sim 11$ GeV. Since the default value of the bottom quark constituent mass is 5 GeV in **Herwig++**, the bump corresponds to $b\bar{b}$ clusters just above the production threshold. At least one of the constituent quarks must have been produced during shower evolution from $g \mapsto b\bar{b}$ splittings, which is strongly suppressed in the standard shower. As a practical choice, this particular shower kernel was removed from further simulations. The prediction by the modified simulation is also plotted in Fig. 8.5.

Lastly, the impact of the cutoff $\mu_{\text{IR}}^{(uds)}$ on the full spectrum of primary clusters was investigated. Fig. 8.6 shows that the best agreement with the standard shower spectrum was found for a value of $\mu_{\text{IR}}^{(uds)} = 0.8$ GeV. Note that the spectra considered cannot be obtained by experiment and that the outcome of the **Herwig++** standard shower is considered plausible simply because it yields satisfactory agreement with experimental data and its shape can be explained by quark production threshold considerations.

After applying the parameters discussed above and manually excluding $g \mapsto b\bar{b}$ branching, B -hadron fragmentation was significantly improved. A new tune of b quark evolution and b hadronization parameters based on these considerations supports a low IR shower cutoff,

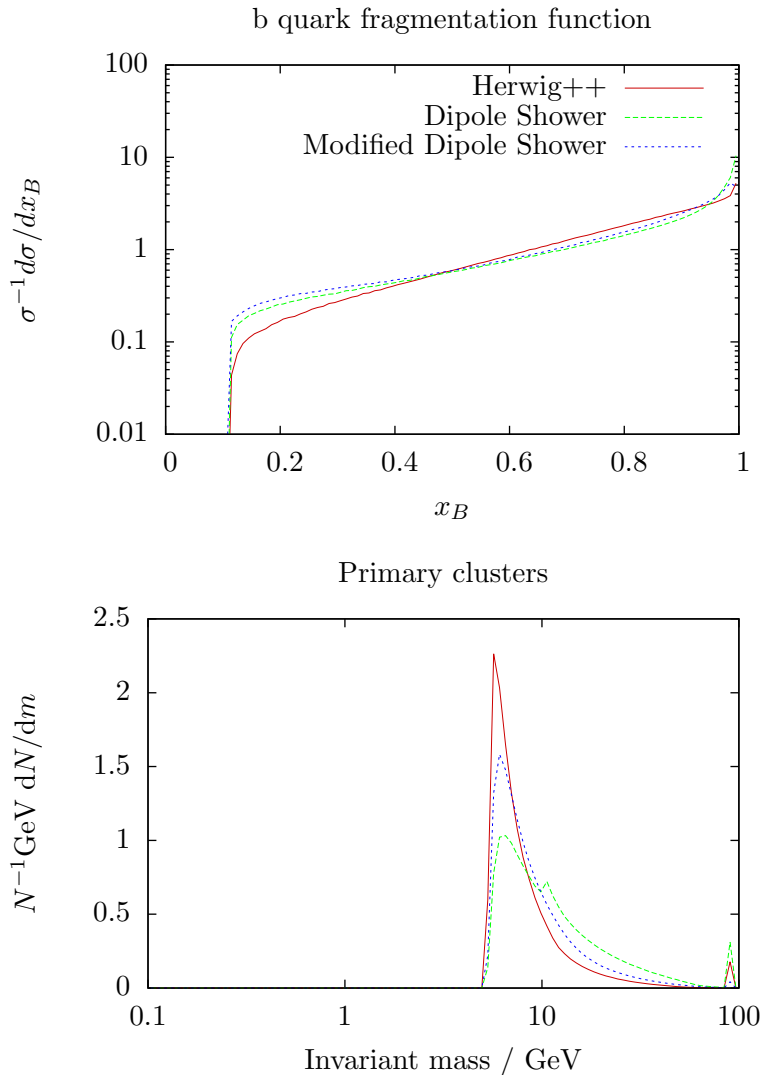


Figure 8.5.: Spectra of b quarks after shower evolution terminated and primary b clusters which are formed from colour-connected pairs of partons. The modified dipole shower was manually adjusted in order to yield better agreement with the spectra obtained by the standard Herwig++ parton shower.

and results are portrayed in Tab. 8.4. For comparison, $g \mapsto b\bar{b}$ branching was excluded for the massless shower implementation, too, and a tune of newly introduced b -quark-specific parameters was attempted. Due to evident deficiencies concerning heavy quark evolution, agreement could not be achieved. Fig. 8.7 shows the results of our adjusted implementation together with the dipole shower in the massless approximation and the standard Herwig++ shower. Agreement with experimental data is still not as good as the results obtained for the standard shower, but the improvement by incorporating finite parton masses is immense.

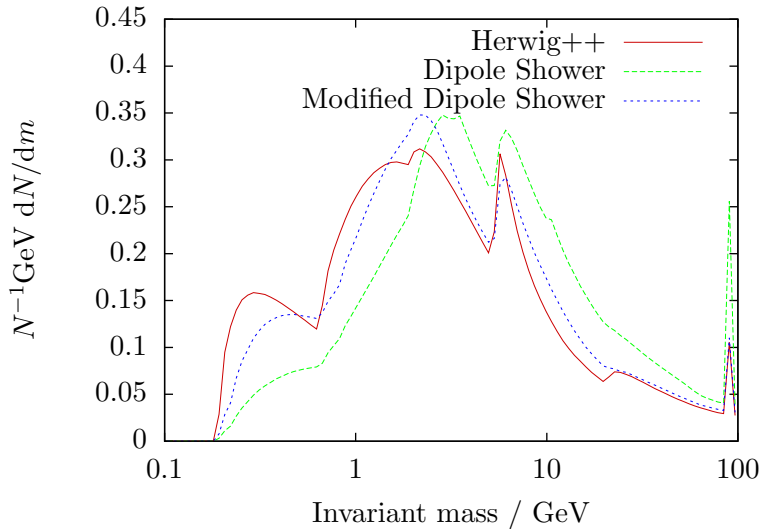


Figure 8.6.: Primary cluster spectrum right before hadronization.

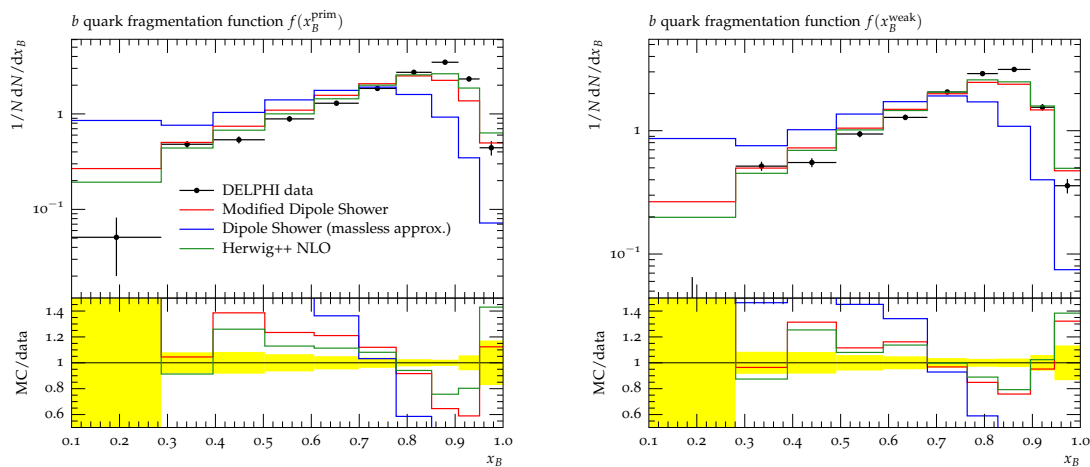


Figure 8.7.: B -hadron fragmentation as predicted by the leading order simulation after adjusting the b quark and primary cluster spectra and performing a new tune with exclusion of $g \rightarrow b\bar{b}$ shower branching. For comparison, the results for the (similarly modified and tuned) dipole shower in the massless approximation and for the standard Herwig++ parton shower are presented as well.

Parameter	LO	NLO
$\mu_{\text{IR,FF}}^{(b)}$	0.273(12) GeV	0.27(3) GeV
$\mu_{\text{soft,FF}}^{(b)}$	0.61(3)	0.392(8)
$\text{Cl}_{\text{max}}^{(b)}$	4.06(9)	0.58(4)
$\text{Cl}_{\text{pow}}^{(b)}$	4.89(12)	9.98(4)
$\text{Cl}_{\text{smr}}^{(b)}$	0.0	0.43(6)
$\text{P}_{\text{split}}^{(b)}$	0.017(10)	0.000(4)

Table 8.4.: Parameters concerning b quark evolution for LO and NLO fits of the modified dipole shower to LEP data. $\text{Cl}_{\text{smr}}^{(b)}$ was set to zero as it was determined negative in the LO tune (but compatible with zero).

8.3. Conclusions

A complete tune of shower and hadronization parameters to experimental data from the LEP experiment was achieved. For a large class of observables, good agreement was found. A detailed investigation of B -hadron fragmentation showed that the best results are obtained for a very low shower cutoff for b quark evolution, specifically $\mu_{\text{IR}}^{(b)} = 0.27$ GeV. An investigation of the primary cluster spectrum hints towards a lower value of the light quark IR cutoff $\mu_{\text{IR}}^{(uds)} \approx 0.8$ GeV, too. However, it is not clear if this value is justified by perturbative QCD. Both cutoff parameters are significantly lower than the default value in the massless dipole shower ($\mu_{\text{IR}}^{m=0} \approx 1.4$ GeV [23]) and the value obtained by tuning. In other words, more emphasis is put on the perturbative QCD shower evolution than on the phenomenological hadronization model.

The overestimation of $g \mapsto b\bar{b}$ splittings in the dipole shower is not understood. Raising the screening scale and IR cutoff for this particular kernel within a reasonable range does not reduce this effect in a sufficient manner. We therefore dropped the kernel from our simulation, which improves the description of B -hadron fragmentation significantly. However, this procedure can only be regarded as a temporary solution and further studies on the dipole shower are necessary, particularly when higher centre-of-mass energies are investigated where neglecting b quark pair production is not justified.

Conclusions and Outlook

The aim of this work was to provide an implementation of a dipole-type parton shower which takes full account of finite parton masses in the event generator `Herwig++`. In parton showers, higher-order corrections are effectively resummed and enhancements to all orders in perturbation theory are approximated. Furthermore, the exact result at NLO accuracy can be obtained when the real emission matrix element is matched to the shower, and all quantities necessary for this procedure were to be provided, too. The implementation had to be tested and validated both at parton and observable level. Moreover, a complete tune to LEP data with emphasis on heavy quarks was necessary due to the qualitatively different description of the evolution of the partonic ensemble. For the sake of a detailed investigation of the new algorithm, an implementation of all quantities that are necessary for hadron collider experiments was postponed.

The desired parton shower implementation has been provided. Parametrizations of the splitting kinematics, phase-space factorization properties and phase-space boundaries were derived for all possible emitter-spectator pairs and arbitrary parton masses. Together with the Catani-Seymour splitting kernels they were implemented and the emission spectrum of the full code was validated against an independent numerical calculation.

Catani-Seymour dipoles, insertion operators and kinematic mappings were provided within the subtraction scheme for NLO calculations. Besides, the real emission contribution to $e^+e^- \mapsto$ jets events was implemented. The functionality of the subtraction algorithm, specifically accordance of the auxiliary subtraction terms with the real emission contribution in the singular phase-space regions, was confirmed numerically.

Consistency of the full implementation with the original algorithms developed for the massless approximation was found at parton and observable level.

Thus, an improved description of the partonic final state was achieved and tuning to LEP data was performed. It was shown that generally good agreement with experimental results is possible. Although significant improvement stemming from the incorporation of finite-mass effects was found for B -hadron fragmentation as well, agreement with data was not obtained at this stage. Since we did not concern ourselves with the hadronization model in `Herwig++`, the partonic final state at the onset of hadronization was investigated in more detail. Whereas the dipole-type parton shower is expected to provide a more accurate description, a comparison to the successful `Herwig++` standard parton shower is

reasonable. This comparison suggests substantially lower IR shower cutoffs particularly for bottom quark branching, on which the spectra of the partonic final state after shower evolution and of primary clusters crucially depend. Hence, within the new algorithm more weight is assigned to the perturbative QCD simulation in the parton shower compared to the phenomenological hadronization model. Moreover, the cluster spectra indicated a strong suppression of $g \mapsto b\bar{b}$ splittings. After the shower was modified in this way, a new tune fully confirmed the previous results and the description of B -hadron fragmentation was significantly improved.

In conclusion, our implementation yields the correct physical results within reach of the dipole shower approximation and gives a good description of the LEP experiment. Additionally, all tools have been provided in order to extend the algorithm to the case of hadron colliders. However, further studies concerning the transition from the parton shower to the non-perturbative domain are indicated. The cluster hadronization model implemented in Herwig++ was developed in the presence of standard parton showers, yet dipole-type showers yield a qualitatively different partonic final state. New insights might be gained via an investigation with emphasis on this aspect. Another loose end of our investigations is the excess of $g \mapsto q\bar{q}$ branching in our implementation, which was discovered due to its impact on B -hadron fragmentation. An investigation of the role of the shower cutoff and the splitting kernel screening scales as well as possible modifications of the splitting kernels seems to deserve special attention.

A.1. Modified and New Classes

In this appendix we present the modifications implemented in the course of this work at code level. See Table A.1 for a listing of the respective classes concerned with shower evolution and Table A.2 for those connected to the evaluation of matrix elements in the subtraction and matching schemes introduced in Chapter 3. For an outline of the structure of the code recall Chapter 6.

A.2. Simulations using Our Implementation

With the introduction of the modifications outlined above to `Herwig++` we are able to simulate events using a dipole-type parton shower which takes full account of finite parton masses. The user may switch between the different implementations at input file level. For this purpose, we give a prescription of the new settings which are now available.

First, the default values for the quark masses can be retained, i.e. the entries

```
set /Herwig/Particles/d:NominalMass 0*GeV
set /Herwig/Particles/dbar:NominalMass 0*GeV
set /Herwig/Particles/u:NominalMass 0*GeV
set /Herwig/Particles/ubar:NominalMass 0*GeV
set /Herwig/Particles/s:NominalMass 0*GeV
set /Herwig/Particles/sbar:NominalMass 0*GeV
set /Herwig/Particles/c:NominalMass 0*GeV
set /Herwig/Particles/cbar:NominalMass 0*GeV
set /Herwig/Particles/b:NominalMass 0*GeV
set /Herwig/Particles/bbar:NominalMass 0*GeV
```

are safe to be removed from `Matchbox.in` and `DipoleShower.in`. As dipole kernels and insertion operators are registered with the repository in an automated way, no adjustments concerning matrix element calculations and matching have to be done.

In `DipoleShower.in` the current way to assign different infrared shower cutoff parameters to heavy quarks is via the creation of additional `DipoleSplittingKinematics` objects,

Class name ← inherits from (light sister class)	Description
DipoleSplittingKinematics ←HandlerBase	Base class for kinematic parametrizations and phase-space weight. Modified to pass more information about the respective splitting to its methods.
FFMassiveKinematics ←DipoleSplittingKinematics (FFLightKinematics)	Contains the kinematic parametrization and phase-space weight for final-final splittings as derived in Chapter 5.
FFMgx2ggxDipoleKernel, FFMgx2qqxDipoleKernel, FFMqx2qgxDipoleKernel. ←DipoleSplittingKernel (FFgx2ggxDipoleKernel etc.)	Azimuthally averaged splitting kernels for final-final $(g, x) \mapsto (g, g, x)$ splittings etc. following the ones derived in Ref. [18].

Table A.1.: New classes which incorporate finite parton masses in the dipole shower.

Class name ← inherits from (light sister class)	Description
DipoleMIOperator ←MatchboxInsertionOperator (DipoleIOperator)	The insertion operator I , removing all singularities from the virtual contribution of an arbitrary process. Takes full account of finite parton masses.
FFMggxDipole, FFMqgxDipole, FFMqxDipole ←SubtractionDipole (FFggxDipole etc.)	The subtraction dipoles for merging of two external legs $gg \mapsto g$ etc.
MatchboxMEllbar2qqbar ←MatchboxMEBase, MatchboxMEllbarqqbar	The full $ll \mapsto q\bar{q}$ matrix element including Born level and the virtual contribution. It has been extended to fully incorporate finite parton masses [48].
MatchboxMEllbar2qqbar ←MatchboxMEBase, MatchboxMEllbarqqbar	The real emission contribution associated with quark pair production in leptonic events. Modifications include an adjustment of the phase space and some book-keeping issues.
FFMassiveTildeKinematics ←TildeKinematics (FFLightTildeKinematics)	Implements the “tilde” mapping $p_{i,j} \equiv p_{i,j}(q_i, q, q_j)$.
FFMassiveInvertedTilde= Kinematics ←InvertedTildeKinematics (FFLightInvertedTilde= Kinematics)	Implements the inverted “tilde” mapping $\{q_i, q, q_j\} \equiv \{q_i, q, q_j\}(p_i, p_j; p_{\perp}^2, z, \phi)$ and corresponding phase-space boundaries as used for automatic POWHEG matching.

Table A.2.: Modified and new classes which incorporate finite parton masses in the calculation of matrix elements.

```
cd /Herwig/DipoleShower/Kinematics
create Herwig::FFMassiveKinematics FFcKinematics
create Herwig::FFMassiveKinematics FFbKinematics
```

The $q \mapsto qg$ kernels are then assigned their respective `DipoleSplittingKinematics` object depending on the quark flavour,

```
create Herwig::FFMqx2qgxDipoleKernel FFMqx2qgxDipoleKernel

cp FFMqx2qgxDipoleKernel FFMux2ugxDipoleKernel
set FFMux2ugxDipoleKernel:Flavour /Herwig/Particles/u
set FFMux2ugxDipoleKernel:SplittingKinematics
  /Herwig/DipoleShower/Kinematics/FFMassiveKinematics
insert /Herwig/DipoleShower/DipoleShowerHandler:Kernels 0
  FFMux2ugxDipoleKernel
```

[same for d,s]

```
cp FFMqx2qgxDipoleKernel FFMcx2cgxDipoleKernel
set FFMcx2cgxDipoleKernel:Flavour /Herwig/Particles/c
set FFMcx2cgxDipoleKernel:SplittingKinematics
  /Herwig/DipoleShower/Kinematics/FFcKinematics
insert /Herwig/DipoleShower/DipoleShowerHandler:Kernels 0
  FFMcx2cgxDipoleKernel
```

```
cp FFMqx2qgxDipoleKernel FFMbx2bgxDipoleKernel
set FFMbx2bgxDipoleKernel:Flavour /Herwig/Particles/b
set FFMbx2bgxDipoleKernel:SplittingKinematics
  /Herwig/DipoleShower/Kinematics/FFbKinematics
insert /Herwig/DipoleShower/DipoleShowerHandler:Kernels 0
  FFMbx2bgxDipoleKernel
```

The same procedure is to be applied to final-final $g \mapsto q\bar{q}$ splitting kernels as well as the respective final-initial and initial-final kernels (once made available).

In the main input file, e.g. `LEP-Matchbox.in` for the LEP experiment, the parameters obtained by the tune presented in Chapter 8 have to be included,

```
read DipoleShowerParametersM-L0.in
```

or

```
read DipoleShowerParametersM-NLO.in
```

for matrix element calculations at NLO accuracy, respectively. Switching between the `MC@NLO` and `POWHEG` matching schemes is well-documented in the default `.in` files.

Splitting Kernels and Insertion Operators

This appendix gives a summary of the splitting kernels and insertion operators which were required for our implementation. They have been presented in Ref. [18] and are recited in the following, using the notations introduced in the previous chapters. For brevity, we only give the expressions for the case of no initial-state hadrons, as implemented in the course of this work.

B.1. Parton-Shower Splitting Kernels

The spin- and/or polarization-averaged splitting kernels as used throughout the parton shower algorithm are commonly denoted $\langle V_{ik,j} \rangle$ for a splitting $i' \mapsto (i, k)$ with a spectator parton j . For final-final splittings they read

$$\langle V_{Qg,j}(y, z) \rangle = 8\pi\mu^{2\epsilon}\alpha_S C_F \left\{ \frac{2}{1-z(1-y)} - \frac{\tilde{v}_{i,j}}{v_{ik,j}} \left[1 + z + \frac{2m_Q^2}{y\bar{s}} + \epsilon(1-z) \right] \right\}, \quad (\text{B.1})$$

$$\langle V_{Q\bar{Q},j}(y, z) \rangle = 8\pi\mu^{2\epsilon}\alpha_S T_R \frac{1}{v_{ik,j}} \left\{ 1 - \frac{2}{1-\epsilon} \left[z(1-z) - (1-\kappa)z_+z_- - \frac{\kappa m_Q^2}{2m_Q^2 + \bar{s}y} \right] \right\}, \quad (\text{B.2})$$

$$\langle V_{gg,j}(y, z) \rangle = 16\pi\mu^{2\epsilon}\alpha_S C_A \left\{ \frac{1}{1-z(1-y)} + \frac{1}{1-(1-z)(1-y)} + \frac{z(1-z) - (1-\kappa)z_+z_- - 2}{v_{ik,j}} \right\}. \quad (\text{B.3})$$

The relative velocity $\tilde{v}_{i,j}$ between the parton momenta p_i and p_j before splitting is given by

$$\tilde{v}_{i,j} = \frac{\sqrt{\lambda(s, M_i^2, M_j^2)}}{s - M_i^2 - M_j^2}. \quad (\text{B.4})$$

After the splitting, the relative velocity $v_{ik,j}$ between $q_i + q$ and q_j reads

$$v_{ik,j} = \frac{\sqrt{[2m_j^2 + \bar{s}(1-y)]^2 - 4m_j^2 s}}{\bar{s}(1-y)}. \quad (\text{B.5})$$

κ is a free parameter of the subtraction scheme, where it cancels in final expressions between the subtraction dipoles and insertion operators. In our implementation we chose $\kappa = 0$. The kinematic variables y and z are defined in Section 5.1 where the phase-space boundary z_{\pm} is also given.

B.2. Splitting Functions in the Subtraction Scheme

In the Catani-Seymour dipole subtraction scheme, colour or spin projections of the splitting functions are required. The final-final dipoles read

$$\langle s|V_{Qg,j}(y,z)|s'\rangle = \langle V_{Qg,j}(y,z)\rangle\delta_{ss'}, \quad (\text{B.6})$$

$$\begin{aligned} \langle \mu|V_{Q\bar{Q},j}(y,z)|\nu\rangle = 8\pi\mu^{2\epsilon}\alpha_S T_R \frac{1}{v_{ik,j}} & \left\{ -g^{\mu\nu} \left[1 - \frac{2\kappa}{1-\epsilon} \left(z_+ z_- - \frac{m_Q^2}{(q_i + q)^2} \right) \right] \right. \\ & \left. - \frac{4}{(q_i + q)^2} \left[z^{(m)} q_i^\mu - z'^{(m)} q^\nu \right] \left[z^{(m)} q_i^\nu - z'^{(m)} q^\mu \right] \right\}, \end{aligned} \quad (\text{B.7})$$

$$\begin{aligned} \langle \mu|V_{gg,j}(y,z)|\nu\rangle = 16\pi\mu^{2\epsilon}\alpha_S C_A & \left\{ -g^{\mu\nu} \left[\frac{1}{1-z(1-y)} + \frac{1}{1-(1-z)(1-y)} - \frac{2-\kappa z_+ z_-}{v_{ik,j}} \right] \right. \\ & \left. + \frac{1}{v_{ik,j}} \frac{1-\epsilon}{q_i \cdot q} \left[z^{(m)} q_i^\mu - z'^{(m)} q^\nu \right] \left[z^{(m)} q_i^\nu - z'^{(m)} q^\mu \right] \right\}, \end{aligned} \quad (\text{B.8})$$

where the abbreviations

$$z^{(m)} = z - \frac{1}{2}(1 - v_{ik,j}), \quad z'^{(m)} = (1 - z) - \frac{1}{2}(1 - v_{ik,j}) \quad (\text{B.9})$$

have been used. All other expressions are given in the previous section and in Section 5.1.

B.3. Insertion Operator

In the case of no identified partons the insertion operator \mathbf{I} reads

$$\begin{aligned} \mathbf{I}_m(\epsilon, \mu^2; q_i, m_i) = -\frac{\alpha_S}{2\pi} \frac{1}{\Gamma(1-\epsilon)} \left(\frac{4\pi\mu^2}{\bar{s}_{jk}} \right)^\epsilon & \sum_j \frac{1}{\mathbf{T}_j^2} \sum_{k \neq j} \mathbf{T}_j \cdot \mathbf{T}_k \\ & \times \left[\mathbf{T}_j^2 \left(\mathcal{V}_j(\bar{s}_{jk}, m, m_j, \{m_F\}; \epsilon, \kappa) - \frac{\pi^2}{3} \right) + \left(\frac{\bar{s}_{jk}}{\mu^2} \right)^\epsilon \Gamma_j(\mu, m, \{m_F\}; \epsilon) \right. \\ & \left. + \gamma_j \ln \frac{\mu^2}{\bar{s}_{jk}} + \gamma_j + K_j + \mathcal{O}(\epsilon) \right], \end{aligned} \quad (\text{B.10})$$

where $\bar{s}_{jk} = 2q \cdot q_j$ and $\{m_F\}$ denotes the set of masses of those massive quarks that may appear in the $g \mapsto q\bar{q}$ splitting. The constants γ_a and K_a read

$$\gamma_q = \frac{3}{2}C_F, \quad \gamma_g = \frac{11}{6}C_A - \frac{2}{3}T_R N_f, \quad (\text{B.11})$$

$$K_q = \left(\frac{7}{2} - \frac{\pi^2}{6} \right) C_F, \quad K_g = \left(\frac{67}{18} - \frac{\pi^2}{6} \right) C_A - \frac{10}{9}T_R N_f, \quad (\text{B.12})$$

for quarks and gluons, respectively. The functions Γ_j depend on the flavour of the parton j and on the parton masses. They read (with dummy arguments suppressed)

$$\Gamma_g(\{m_F\}; \epsilon) = \frac{1}{\epsilon} \gamma_g - \frac{2}{3} T_R \sum_{F=1}^{N_F} \ln \frac{m_F^2}{Q_{\text{aux}}^2}, \quad (\text{B.13})$$

$$\Gamma_q(\epsilon) = \frac{1}{\epsilon} \gamma_q, \quad (\text{B.14})$$

$$\Gamma_Q(\mu, m_Q; \epsilon) = C_F \left[\frac{1}{\epsilon} + \frac{1}{2} \ln \frac{m_Q^2}{\mu^2} - 2 \right], \quad (\text{B.15})$$

where the subscript q denotes massless (anti-)quarks and Q denotes massive (anti-)quarks. Q_{aux} is an auxiliary mass scale which cancels between Eqs. (B.13) and (B.25) in the final expression. N_F denotes the number of heavy flavours.

The kernels \mathcal{V}_j depend on the flavour of parton j and on the momenta and masses of both partons j and k . They are decomposed into one contribution which is symmetric with respect to the interchange of the indices j and k and exhibits singularities, and another contribution which is neither symmetric nor singular,

$$\mathcal{V}_j(\bar{s}_{jk}, m_j, m_k, \{m_F\}; \epsilon, \kappa) = \mathcal{V}_j^{(\text{S})}(\bar{s}_{jk}, m_j, m_k; \epsilon) + \mathcal{V}_j^{(\text{NS})}(\bar{s}_{jk}, m_j, m_k, \{m_F\}; \kappa). \quad (\text{B.16})$$

The singular terms read

$$\begin{aligned} \mathcal{V}_j^{(\text{S})}(\bar{s}_{jk}, m_j > 0, m_k > 0; \epsilon) &= \frac{1}{v_{jk}} \left[\frac{1}{\epsilon} \ln \rho - \frac{1}{4} \ln^2 \rho_j^2 - \frac{1}{4} \ln^2 \rho_k^2 - \frac{\pi^2}{6} \right] \\ &\quad + \frac{1}{v_{jk}} \ln \rho \ln \frac{s_{jk}}{\bar{s}_{jk}}, \end{aligned} \quad (\text{B.17})$$

$$\begin{aligned} \mathcal{V}_j^{(\text{S})}(\bar{s}_{jk}, m_j > 0, > 0; \epsilon) &= \frac{1}{2\epsilon^2} + \frac{1}{2\epsilon} \ln \frac{m_j^2}{\bar{s}_{jk}} - \frac{1}{4} \ln^2 \frac{m_j^2}{\bar{s}_{jk}} - \frac{\pi^2}{12} \\ &\quad - \frac{1}{2} \ln \frac{m_j^2}{\bar{s}_{jk}} \ln \frac{\bar{s}_{jk}}{s_{jk}} - \frac{1}{2} \ln \frac{m_j^2}{s_{jk}} \ln \frac{\bar{s}_{jk}}{s_{jk}}, \end{aligned} \quad (\text{B.18})$$

$$\mathcal{V}_j^{(\text{S})}(\bar{s}_{jk}, 0, 0; \epsilon) = \frac{1}{\epsilon^2}, \quad (\text{B.19})$$

with $s_{jk} = \bar{s}_{jk} + m_j^2 + m_k^2$ and the relative velocity between partons j and k given by

$$v_{jk} = \frac{\sqrt{\lambda(s_{jk}, m_j^2, m_k^2)}}{\bar{s}_{jk}}. \quad (\text{B.20})$$

The quantities ρ and ρ_n read

$$\rho = \sqrt{\frac{1 - v_{jk}}{1 + v_{jk}}}, \quad \rho_n = \sqrt{\frac{1 - v_{jk} + 2m_n^2/\bar{s}}{1 + v_{jk} + 2m_n^2/\bar{s}}}. \quad (\text{B.21})$$

The non-singular terms depend on the flavours and masses of partons j and k . With

dummy arguments suppressed, they read

$$\begin{aligned} \mathcal{V}_Q^{(\text{NS})}(\bar{s}_{jk}, m_j > 0, m_k > 0) &= \frac{\gamma_q}{\mathbf{T}_q^2} \ln \frac{\bar{s}_{jk}}{s_{jk}} \\ &+ \frac{1}{v_{jk}} \left[\ln \rho^2 \ln(1 + \rho^2) + 2 \text{Li}_2(\rho^2) - \text{Li}_2(1 - \rho_j^2) - \text{Li}_2(1 - \rho_k^2) - \frac{\pi^2}{6} \right] \\ &+ \ln \frac{\sqrt{s_{jk}} - m_k}{\sqrt{s_{jk}}} - 2 \ln \frac{(\sqrt{s_{jk}} - m_k)^2 - m_j^2}{s_{jk}} - \frac{2m_j^2}{\bar{s}_{jk}} \ln \frac{m_j}{\sqrt{s_{jk}} - m_k} \\ &- \frac{m_k}{\sqrt{s_{jk}} - m_k} + \frac{2m_k(2m_k - \sqrt{s_{jk}})}{\bar{s}_{jk}} + \frac{\pi^2}{2}, \end{aligned} \quad (\text{B.22})$$

$$\mathcal{V}_Q^{(\text{NS})}(\bar{s}_{jk}, m_j > 0, 0) = \frac{\gamma_q}{\mathbf{T}_q^2} \ln \frac{\bar{s}_{jk}}{s_{jk}} + \frac{\pi^2}{6} - \text{Li}_2 \frac{\bar{s}_{jk}}{s_{jk}} - 2 \ln \frac{\bar{s}_{jk}}{s_{jk}} - \frac{m_j^2}{\bar{s}_{jk}} \ln \frac{m_j^2}{s_{jk}}, \quad (\text{B.23})$$

$$\mathcal{V}_q^{(\text{NS})}(\bar{s}_{jk}, 0, m_k > 0) = \frac{\gamma_q}{\mathbf{T}_q^2} \left[\ln \frac{\bar{s}_{jk}}{s_{jk}} - 2 \ln \frac{\sqrt{s_{jk}} - m_k}{\sqrt{s_{jk}}} - \frac{2m_k}{\sqrt{s_{jk}} + m_k} \right] + \frac{\pi^2}{6} - \text{Li}_2 \frac{\bar{s}_{jk}}{s_{jk}}, \quad (\text{B.24})$$

$$\begin{aligned} \mathcal{V}_g^{(\text{NS})}(\bar{s}_{jk}, 0, m_k > 0, \{m_F\}; \kappa) &= \frac{\gamma_g}{\mathbf{T}_q^2} \left[\ln \frac{\bar{s}_{jk}}{s_{jk}} - 2 \ln \frac{\sqrt{s_{jk}} - m_k}{\sqrt{s_{jk}}} - \frac{2m_k}{\sqrt{s_{jk}} + m_k} \right] \\ &+ \frac{\pi^2}{6} - \text{Li}_2 \frac{\bar{s}_{jk}}{s_{jk}} + \frac{2}{3} \frac{T_R}{C_A} \sum_{F=1}^{N_F} \ln \frac{m_F^2}{Q_{\text{aux}}^2} \\ &+ \frac{4}{3} \frac{T_R}{C_A} \sum_{F=1}^{N_F^{jk}} \left[\ln \frac{\sqrt{s_{jk}} - m_k}{\sqrt{s_{jk}}} + \frac{m_k \rho_1^3}{\sqrt{s_{jk}} + m_k} + \ln \frac{1 + \rho_1}{2} - \frac{\rho_1}{3} (3 + \rho_1^2) - \frac{1}{2} \ln \frac{m_F^2}{s_{jk}} \right] \\ &+ \left(\kappa - \frac{2}{3} \right) \frac{m_k^2}{\bar{s}_{jk}} \left[\left(2 \frac{T_R}{C_A} N_f - 1 \right) \ln \frac{2m_k}{\sqrt{s_{jk}} + m_k} \right. \\ &\quad \left. 2 \frac{T_R}{C_A} \sum_{F=1}^{N_F^{jk}} \left(\rho_2^3 \ln \frac{\rho_2 - \rho_1}{\rho_2 + \rho_1} - \ln \frac{1 - \rho_1}{1 + \rho_1} - \frac{8\rho_1 m_F^2}{\bar{s}_{jk}} \right) \right], \end{aligned} \quad (\text{B.25})$$

$$\mathcal{V}_q^{(\text{NS})}(\bar{s}_{jk}, 0, 0) = 0, \quad (\text{B.26})$$

$$\begin{aligned} \mathcal{V}_g^{(\text{NS})}(\bar{s}_{jk}, 0, 0, \{m_F\}) &= \\ &\frac{4}{3} \frac{T_R}{C_A} \sum_{F=1}^{N_F^{jk}} \left[\ln \frac{1 + \rho_1}{2} - \frac{\rho_1}{3} (3 + \rho_1^2) - \frac{1}{2} \ln \frac{m_F^2}{\bar{s}_{jk}} \right] + \frac{2}{3} \frac{T_R}{C_A} \sum_{F=1}^{N_F} \ln \frac{m_F^2}{Q_{\text{aux}}^2}. \end{aligned} \quad (\text{B.27})$$

N_F^{jk} is the number of those heavy flavours for which $\bar{s}_{jk} > 4m_F(m_F + m_k)$. Note that for $m_F \mapsto 0$, we can set $N_F^{jk} = N_F$ because the region of vanishing \bar{s}_{jk} gives a vanishing contribution to infrared-safe observables [18]. $\rho_{1,2}$ appearing in Eq. B.25 are given by

$$\rho_1 = \sqrt{1 - \frac{4m_F^2}{(\sqrt{s_{jk}} - m_k)^2}}, \quad \rho_2 = \sqrt{1 - \frac{4m_F^2}{s_{jk} - m_k^2}}. \quad (\text{B.28})$$

Bibliography

- [1] S. Weinberg, *A Model of Leptons*. Phys.Rev.Lett. **19** (1967) 1264–1266.
<http://link.aps.org/doi/10.1103/PhysRevLett.19.1264>.
- [2] A. Salam and J. Ward, *Weak and electromagnetic interactions*. Il Nuovo Cimento (1955-1965) **11** (1959) 568–577. <http://dx.doi.org/10.1007/BF02726525>.
10.1007/BF02726525.
- [3] S. L. Glashow, J. Iliopoulos, and L. Maiani, *Weak Interactions with Lepton-Hadron Symmetry*. Phys. Rev. D **2** (1970) 1285–1292.
<http://link.aps.org/doi/10.1103/PhysRevD.2.1285>.
- [4] M. Bähr, S. Gieseke, M. Gigg, D. Grellscheid, K. Hamilton, *et al.*, *Herwig++ Physics and Manual*. Eur.Phys.J. **C58** (2008) 639–707, [arXiv:0803.0883](https://arxiv.org/abs/0803.0883) [hep-ph].
- [5] T. Sjöstrand, S. Mrenna, and P. Z. Skands, *A Brief Introduction to PYTHIA 8.1*. Comput.Phys.Commun. **178** (2008) 852–867, [arXiv:0710.3820](https://arxiv.org/abs/0710.3820) [hep-ph].
- [6] T. Gleisberg, S. Hoeche, F. Krauss, M. Schönherr, S. Schumann, *et al.*, *Event generation with SHERPA 1.1*. JHEP **0902** (2009) 007, [arXiv:0811.4622](https://arxiv.org/abs/0811.4622) [hep-ph].
- [7] S. Gieseke, A. Ribon, M. H. Seymour, P. Stephens, and B. Webber, *Herwig++ 1.0: An Event generator for e+ e- annihilation*. JHEP **0402** (2004) 005, [arXiv:hep-ph/0311208](https://arxiv.org/abs/hep-ph/0311208) [hep-ph].
- [8] M. E. Peskin and D. V. Schroeder, *An Introduction To Quantum Field Theory (Frontiers in Physics)*. Westview Press, 1995.
- [9] D. J. Gross and F. Wilczek, *Ultraviolet Behavior of Non-Abelian Gauge Theories*. Phys. Rev. Lett. **30** (1973) 1343–1346.
<http://link.aps.org/doi/10.1103/PhysRevLett.30.1343>.
- [10] H. D. Politzer, *Reliable Perturbative Results for Strong Interactions?* Phys. Rev. Lett. **30** (1973) 1346–1349.
<http://link.aps.org/doi/10.1103/PhysRevLett.30.1346>.
- [11] M. Kaku, *Quantum Field Theory: A Modern Introduction*. Oxford University Press, 1993.

- [12] T. Kinoshita, *Mass singularities of Feynman amplitudes*. J.Math.Phys. **3** (1962) 650–677.
- [13] S. Plätzer and S. Gieseke, *Coherent Parton Showers with Local Recoils*. JHEP **1101** (2011) 024, [arXiv:0909.5593 \[hep-ph\]](#).
- [14] S. Frixione, Z. Kunszt, and A. Signer, *Three jet cross-sections to next-to-leading order*. Nucl.Phys. **B467** (1996) 399–442, [arXiv:hep-ph/9512328 \[hep-ph\]](#).
- [15] D. A. Kosower, *Antenna factorization of gauge theory amplitudes*. Phys.Rev. **D57** (1998) 5410–5416, [arXiv:hep-ph/9710213 \[hep-ph\]](#).
- [16] A. Gehrmann-De Ridder and M. Ritzmann, *NLO Antenna Subtraction with Massive Fermions*. JHEP **0907** (2009) 041, [arXiv:0904.3297 \[hep-ph\]](#).
- [17] S. Catani and M. Seymour, *A general algorithm for calculating jet cross sections in NLO QCD*. Nuclear Physics **B485** (1997) 291 – 419, [arXiv:hep-ph/9605323v3](#).
- [18] S. Catani, S. Dittmaier, M. H. Seymour, and Z. Trócsányi, *The dipole formalism for next-to-leading order QCD calculations with massive partons*. Nuclear Physics **B627** (2002) 189 – 265, [arXiv:hep-ph/0201036v1](#).
- [19] S. Catani, S. Dittmaier, and Z. Trocsanyi, *One loop singular behavior of QCD and SUSY QCD amplitudes with massive partons*. Phys.Lett. **B500** (2001) 149–160, [arXiv:hep-ph/0011222 \[hep-ph\]](#).
- [20] R. K. Ellis, W. J. Stirling, and B. R. Webber, *QCD and Collider Physics*, vol. 8. Cambridge University Press, 1996.
- [21] S. Schumann and F. Krauss, *A Parton shower algorithm based on Catani-Seymour dipole factorisation*. JHEP **0803** (2008) 038, [arXiv:0709.1027 \[hep-ph\]](#).
- [22] M. Dinsdale, M. Ternick, and S. Weinzierl, *Parton showers from the dipole formalism*. Phys.Rev. **D76** (2007) 094003, [arXiv:0709.1026 \[hep-ph\]](#).
- [23] S. Plätzer and S. Gieseke, *Dipole Showers and Automated NLO Matching in Herwig++*. [arXiv:1109.6256 \[hep-ph\]](#).
- [24] S. Plätzer, *Parton Showers and Radiative Corrections in QCD*. PhD thesis, Karlsruher Institut für Technologie, 2010.
- [25] S. Frixione and B. R. Webber, *Matching NLO QCD computations and parton shower simulations*. JHEP **0206** (2002) 029, [arXiv:hep-ph/0204244 \[hep-ph\]](#).
- [26] S. Frixione, P. Nason, and C. Oleari, *Matching NLO QCD computations with Parton Shower simulations: the POWHEG method*. JHEP **0711** (2007) 070, [arXiv:0709.2092 \[hep-ph\]](#).
- [27] M. Bähr, *Underlying Event Simulation in the Herwig++ Event Generator*. PhD thesis, Universität Karlsruhe (TH), 2008.
- [28] E. Boos, M. Dobbs, W. Giele, I. Hinchliffe, J. Huston, *et al.*, *Generic user process interface for event generators*. [arXiv:hep-ph/0109068 \[hep-ph\]](#).
- [29] J. Alwall, A. Ballestrero, P. Bartalini, S. Belov, E. Boos, *et al.*, *A Standard format for Les Houches event files*. Comput.Phys.Commun. **176** (2007) 300–304, [arXiv:hep-ph/0609017 \[hep-ph\]](#).

- [30] K. Arnold, M. Bähr, G. Bozzi, F. Campanario, C. Englert, *et al.*, *VBFNLO: A Parton level Monte Carlo for processes with electroweak bosons*. Comput.Phys.Commun. **180** (2009) 1661–1670, arXiv:0811.4559 [hep-ph].
- [31] F. Maltoni and T. Stelzer, *MadEvent: Automatic event generation with MadGraph*. JHEP **0302** (2003) 027, arXiv:hep-ph/0208156 [hep-ph].
- [32] M. Bähr, S. Gieseke, and M. H. Seymour, *Simulation of multiple partonic interactions in Herwig++*. JHEP **0807** (2008) 076, arXiv:0803.3633 [hep-ph].
- [33] S. Gieseke, P. Stephens, and B. Webber, *New formalism for QCD parton showers*. JHEP **0312** (2003) 045, arXiv:hep-ph/0310083 [hep-ph].
- [34] R. D. Field and S. Wolfram, *A QCD model for e^+e^- annihilation*. Nucl.Phys. **B213** (1983) 65–84.
- [35] A. Buckley, J. Butterworth, L. Lönnblad, H. Hoeth, J. Monk, *et al.*, *Rivet user manual*. arXiv:1003.0694 [hep-ph].
- [36] **SLD** Collaboration, K. Abe *et al.*, *Production of π^+ , π^- , K^+ , K^- , p and anti- p in light (uds), c and b jets from Z^0 decays*. Phys.Rev. **D69** (2004) 072003, arXiv:hep-ex/0310017 [hep-ex].
- [37] A. Buckley, H. Hoeth, H. Lacker, H. Schulz, and J. E. von Seggern, *Systematic event generator tuning for the LHC*. Eur.Phys.J. **C65** (2010) 331–357, arXiv:0907.2973 [hep-ph].
- [38] S. Plätzer, *ExSample: A Library for Sampling Sudakov-Type Distributions*. arXiv:1108.6182 [hep-ph].
- [39] G. Marchesini and B. Webber, *Monte Carlo simulation of general hard processes with coherent QCD radiation*. Nuclear Physics B **310** (1988) no. 3-4, 461–526. <http://www.sciencedirect.com/science/article/pii/0500321388900892>.
- [40] B. Webber, *Color reconnection and Bose-Einstein effects*. J.Phys.G **G24** (1998) 287–296, arXiv:hep-ph/9708463 [hep-ph].
- [41] **ALEPH** Collaboration, A. Heister *et al.*, *Studies of QCD at e^+e^- centre-of-mass energies between 91 and 209 GeV*. The European Physical Journal C - Particles and Fields **35** (2004) 457–486. <http://dx.doi.org/10.1140/epjc/s2004-01891-4>. 10.1140/epjc/s2004-01891-4.
- [42] **DELPHI** Collaboration, P. Abreu *et al.*, *Tuning and test of fragmentation models based on identified particles and precision event shape data*. Zeitschrift für Physik C Particles and Fields **73** (1996) 11–59. <http://dx.doi.org/10.1007/s002880050295>. 10.1007/s002880050295.
- [43] **DELPHI** Collaboration, G. Barker *et al.*, *A study of the b -quark fragmentation function with the DELPHI detector at LEP1*. DELPHI 2002-069 CONF 603 (2002) .
- [44] **JADE**, **OPAL** Collaboration, P. Pfeifenschneider *et al.*, *QCD analyses and determinations of $\alpha(s)$ in e^+e^- annihilation at energies between 35-GeV and 189-GeV*. Eur.Phys.J. **C17** (2000) 19–51, arXiv:hep-ex/0001055 [hep-ex].
- [45] **Particle Data Group** Collaboration, K. Nakamura *et al.*, *Review of particle physics*. J.Phys.G **G37** (2010) 075021.

-
- [46] **Particle Data Group** Collaboration, C. Amsler *et al.*, *Review of Particle Physics*. Phys.Lett. **B667** (2008) 1–1340.
- [47] **OPAL Collaboration** Collaboration, K. Ackerstaff *et al.*, *Measurements of flavor dependent fragmentation functions in $Z^0 \rightarrow q \text{ anti-}q$ events*. Eur.Phys.J. **C7** (1999) 369–381, [arXiv:hep-ex/9807004](https://arxiv.org/abs/hep-ex/9807004) [hep-ex].
- [48] J. Jersák, E. Laermann, and P. M. Zerwas, *Electroweak production of heavy quarks in e^+e^- annihilation*. Phys. Rev. D **25** (1982) 1218–1228.
<http://link.aps.org/doi/10.1103/PhysRevD.25.1218>.

Danksagung

In erster Linie möchte ich mich bei Herrn Prof. Dr. Dieter Zeppenfeld bedanken, dass er mir die Möglichkeit gegeben hat, zu diesem interessanten Themengebiet eine Diplomarbeit anzufertigen.

Mein besonderer Dank gilt Herrn Dr. Stefan Gieseke, der diese Arbeit mitbetreut hat und der sich stets Zeit für mich genommen hat. In zahlreichen Gesprächen konnte ich sehr viel von ihm lernen. Ich danke ihm auch für die Möglichkeit, mich am DESY eine Woche lang mit Herrn Dr. Simon Plätzer auszutauschen. Ebenfalls bedanken möchte ich mich für seine Korrekturvorschläge zu meiner Arbeit.

Herrn Dr. Simon Plätzer danke ich dafür, dass er mir bei offenen Fragen immer zur Seite stand und mich bei meiner Arbeit sehr unterstützt und vorangebracht hat. Weiter danke ich ihm dafür, dass er sich für mich Zeit genommen und eine weitere Fahrt ans DESY ermöglicht hat. Für ausführliche Korrekturvorschläge zu meiner Arbeit bin ich ihm ebenfalls sehr dankbar.

Herrn Prof. Dr. Günter Quast danke ich herzlich für die Übernahme des Korreferats.

Mein ausdrücklicher Dank gilt den Korrekturlesern Yasmin Anstruther, Johannes Bellm, Anastasia Bierweiler, Kathrin Ender, Jessica Frank, Ramona Gröber, Christian Hangst, Matthias Kerner, Dr. Sophy Palmer, Christian Röhr und Matthias Weinreuter, sowie Daniel Gandyra für seine Unterstützung während des Drucks.

Bedanken möchte ich mich außerdem bei allen Institutsmitgliedern für die gute Atmosphäre. Besondere Erwähnung verdienen auch die Administratoren Bastian Feigl und Christian Röhr, die bei zahlreichen Problemen keine Scheu hatten, weiterzuhelfen.

Meine Freunde waren mir während des gesamten Studiums eine große Unterstützung.

Schließlich bedanke ich mich bei meinen Eltern, die mir das Studium erst ermöglicht und mir immer Unterstützung entgegengebracht haben.